

# DEFENCE S&T TECHNICAL BULLETIN

VOL. 17 NUM. 1 YEAR 2024 eISSN 3009-1896

## CONTENTS

Efficacy Testing Analysis of Antimicrobial Treatments on Different Military Fabric Materials <i>Nik Nur Ilyani Mohamed Nazri, Zulhilmi Zuhairie Muhammad, Muhammad Fawwaz Mohd Usoff, Noor Hafifi Zuriani Abdul Rahim, Farizah Abd Fatah, Mohd Badrolnizam Jamhari, Ahmad Razi Mohd Yunus &amp; Aznida Yusuf</i>	1 - 13
Comparison of Moisture Management Properties for Malaysian Government Uniforms <i>Nurul Hidayah Abdul Aziz, Nor Hafizah Mohd Jais, Wan Elyn Amira Wan Adnan &amp; Ahmad Ikhwan Muaz Abd Rahman</i>	14 - 27
A Comparative Study on Indoor Air Quality (IAQ) Between Centralised and Split Unit Air Conditioning Systems in a Naval Ship <i>Amirul Faiz Kamaruddin, Maryam Zahaba, Nur Sarah Fatimah Tamsi, Mohd Khusainy Anua, Noor Artika Hassan, Nur Sazwi Nordin &amp; Arman Ariffin</i>	28 - 36
Fusion Datasets for Ultrasonic Weld Defect Classification with Transfer Learning in Neural Networks <i>Suhairy Sani, Mohamad Hanif Md Saad, Norsalim Muhammad, Siti Fatahiyah Mohamad &amp; Megat Harun Al Rashid Megat Ahmad</i>	37 - 48
Quasi-Static Indentation Testing of Stainless-Steel Wire Mesh / Epoxy Laminated Composites <i>Nurul Zakiah Zamri Tan, Azrin Hani Abdul Rashid, Md. Mominur Rahman Mohd, Mohd Yazid Yahya, Mohd Yuhazri Yaakob, Risby Mohd Sohaimi &amp; Anis Amirah Nor Anuwar</i>	49 - 62
Manpack Ground Surveillance Radar as Supporting Equipment for the Indonesian Army <i>Yussi Perdana Saputera, Moh. Khusaini, Dhiana Puspitawati &amp; Arif Harnanto</i>	63 - 72
Shortest Possible Dual-Section Matching Network <i>Chung Boon Kuan</i>	73 - 83
Evaluation of the Effect of Multipath on Multi-GNSS Performance via GNSS Simulation <i>Dinesh Sathyamoorthy</i>	84 - 89
GPS Jamming Impact on UAV Performance in Outdoor Environments <i>Nurhakimah Norhashim, Nadhiya Liyana Mohd Kamal, Zulhilmy Sahwee, Shahrul Ahmad Shah, Nur Afiqah Alfian &amp; Dinesh Sathyamoorthy</i>	90 - 97
A Case Study of Failure Reporting Analysis and Corrective Action System (FRACAS) for Medical Oxygen Plant (MOP) <i>Manmeet Singh &amp; Nilesh Ware</i>	98 - 104



Ministry of  
Defence  
Malaysia

SCIENCE & TECHNOLOGY RESEARCH INSTITUTE FOR DEFENCE (STRIDE)

## **EDITORIAL BOARD**

### **Chief Editor**

Gs. Dr. Dinesh Sathyamoorthy

### **Deputy Chief Editor**

Dr. Mahdi bin Che Isa

### **Associate Editors**

Dr. Ridwan bin Yahaya

Dr. Norliza bt Hussein

Dr. Rafidah bt Abd Malik

Ir. Dr. Shamsul Akmar bin Ab Aziz

Ts. Dr. Fadzli bin Ibrahim

Dr. Nik Hassanuddin bin Nik Yusoff

Ir. Dr. Nur Afande bin Ali Hussain

Nor Hafizah bt Mohamed

Kathryn Tham Bee Lin

Masliza bt Mustafar

Siti Rozanna bt Yusuf

### **Published by:**

Science & Technology Research Institute for Defence (STRIDE)

Taman Bukit Mewah Fasa 9, 43000 Kajang, Selangor, Malaysia

Email: [dinesh.sathyamoorthy@stride.gov.my](mailto:dinesh.sathyamoorthy@stride.gov.my) / [mahdi.cheisa@stride.gov.my](mailto:mahdi.cheisa@stride.gov.my)

Tel.: +603-8732 4400

The Defence S&T Technical Bulletin is published biannually.

eISSN 3009-1896



9 773009 189007

## AIMS AND SCOPE

The Defence S&T Technical Bulletin is the official journal of the Science & Technology Research Institute for Defence (STRIDE). The journal, which is indexed in, among others, Scopus, Index Corpenicus, ProQuest and EBSCO, contains manuscripts on research findings in various fields of defence science & technology. The primary purpose of this journal is to act as a channel for the publication of defence-based research work undertaken by researchers both within and outside the country.

## WRITING FOR THE DEFENCE S&T TECHNICAL BULLETIN

Contributions to the journal should be based on original research in areas related to defence science & technology. All contributions should be in English.

## PUBLICATION

The editors' decision with regard to publication of any item is final. A manuscript is accepted on the understanding that it is an original piece of work that has not been accepted for publication elsewhere.

## PRESENTATION OF MANUSCRIPTS

The format of the manuscript is as follows:

- a) Page size A4
- b) MS Word format
- c) Single space
- d) Justified
- e) In Times New Roman, 11-point font
- f) Should not exceed 15 pages, including references
- g) Texts in charts and tables should be in 10-point font.

Please email the manuscript to:

- 1) Gs. Dr. Dinesh Sathyamoorthy (dinesh.sathyamoorthy@stride.gov.my)
- 2) Dr. Mahdi bin Che Isa (mahdi.cheisa@stride.gov.my)

The next edition of the journal (Vol. 17, Num. 2) is expected to be published in November 2024. The due date for submissions is 6 August 2024. **It is strongly iterated that authors are solely responsible for taking the necessary steps to ensure that the submitted manuscripts do not contain confidential or sensitive material.**

The template of the manuscript is as follows:

# TITLE OF MANUSCRIPT

Name(s) of author(s)

Affiliation(s)

Email:

## ABSTRACT

*Contents of abstract.*

**Keywords:** *Keyword 1; keyword 2; keyword 3; keyword 4; keyword 5.*

### 1. TOPIC 1

Paragraph 1.

Paragraph 2.

#### 1.1 Sub Topic 1

Paragraph 1.

Paragraph 2.

### 2. TOPIC 2

Paragraph 1.

Paragraph 2.

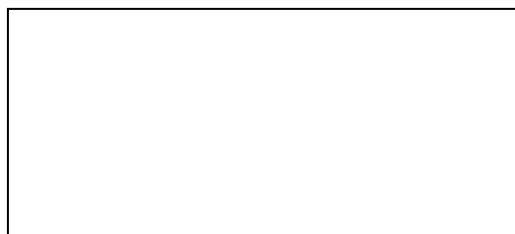


**Figure 1: Title of figure.**

**Table 1: Title of table.**

Content	Content	Content
Content	Content	Content
Content	Content	Content
Content	Content	Content

Equation 1 (1)  
Equation 2 (2)

## REFERENCES

Long lists of notes of bibliographical references are generally not required. The method of citing references in the text is 'name date' style, e.g. 'Hanis (1993) claimed that...', or '...including the lack of interoperability (Bohara *et al.*, 2003)'. End references should be in alphabetical order. The following reference style is to be adhered to:

### Books

Serra, J. (1982). *Image Analysis and Mathematical Morphology*. Academic Press, London.

### Book Chapters

Goodchild, M.F. & Quattrochi, D.A. (1997). Scale, multiscaling, remote sensing and GIS. In Quattrochi, D.A. & Goodchild, M.F. (Eds.), *Scale in Remote Sensing and GIS*. Lewis Publishers, Boca Raton, Florida, pp. 1-11.

### Journals / Serials

Jang, B.K. & Chin, R.T. (1990). Analysis of thinning algorithms using mathematical morphology. *IEEE T. Pattern Anal.*, **12**: 541-550.

### Online Sources

GTOPO30 (1996). *GTOPO30: Global 30 Arc Second Elevation Data Set*. Available online at: <http://edcwww.cr.usgs.gov/landdaac/gtopo30/gtopo30.html> (Last access date: 1 June 2009).

### Unpublished Materials (e.g. theses, reports and documents)

Wood, J. (1996). *The Geomorphological Characterization of Digital Elevation Models*. PhD Thesis, Department of Geography, University of Leicester, Leicester.

# EFFICACY TESTING ANALYSIS OF ANTIMICROBIAL TREATMENTS ON DIFFERENT MILITARY FABRIC MATERIALS

Nik Nur Ilyani Mohamed Nazri<sup>1\*</sup>, Zulhilmi Zuhairie Muhammad<sup>1</sup>, Muhammad Fawwaz Mohd Usoff<sup>4</sup>, Noor Hafifi Zuriani Abdul Rahim<sup>2</sup>, Farizah Abd Fatah<sup>3</sup>, Mohd Badrolnizam Jamhari<sup>1</sup>, Ahmad Razi Mohd Yunus<sup>1</sup> & Aznida Yusuf<sup>1</sup>

<sup>1</sup>Protection and Biophysical Technology Division (BTPB)

<sup>2</sup>Instrumentation and Electronics Technology Division (BTIE)

<sup>3</sup>Tropical Research Centre (TRC)

Science and Technology Research Institute for Defence (STRIDE), Ministry of Defence, Malaysia

<sup>4</sup>Disease Department, National Public Health Laboratory (NPHL), Ministry of Health, Malaysia

\*Email: nikilyani.nazri@stride.gov.my

## ABSTRACT

*Antimicrobial textiles have emerged as a new trend, particularly in military settings, due to their capacity to reduce the risk of infection transmission, improve cleanliness, as well as promote overall health and safety. In this study, three antimicrobial solutions were chosen to be tested, which were Antimicrobials A, B and C, by applying them on three different fabric materials of Malaysian Armed Forces (MAF) clothes, which were polyester cotton, polyester and cotton. There were three potential pathogenic bacteria employed in this experiment, which were Escherichia coli (E. coli), Klebsiella pneumoniae (K. pneumoniae) and Staphylococcus aureus (S. aureus). The samples were categorised as treated and untreated samples, and non-fabric samples as control. The treated samples were treated with each antimicrobial solution using a spray method. Three serial dilutions were performed for all the samples using the shake flask test in saline water method. After the final 24 h of incubation, the colony forming unit (CFU) readings of the test samples for 0, 1, 3 and 24 h were counted and recorded using an automatic colony counter (Interscience Scan 4000, USA). From the results obtained, S. aureus was the highest bacteria that had been reduced by all three antimicrobial solutions. Overall, the treated samples showed higher bacterial reduction trend as compared to the untreated samples. For the treated samples, the results showed that the combination of Antimicrobials A and B, which contained titanium dioxide (TiO<sub>2</sub>) as their primarily active components, with cotton fabrics had higher efficacy in eradicating all three bacteria. It was found that the Antimicrobial A was more efficient than Antimicrobial B due to high dodecanoic acid content as additional active ingredient in Antimicrobial A that also helps to eradicate the evaluated bacteria through lytic action. For the untreated samples, the most bacterial reduction could also be seen on the cotton fabrics. In conclusion, this study found that the combination of Antimicrobial A and cotton fabrics was the most suitable pair to be used in future research for the development of MAF antimicrobial clothes.*

**Keywords:** *Antimicrobial textiles; fabric materials; pathogenic bacteria; titanium dioxide (TiO<sub>2</sub>); colony forming unit (CFU).*

## 1. INTRODUCTION

The Malaysian Armed Forces (MAF) are frequently exposed to diverse bacteria in their daily routine, whether in their military dorms or training fields. During conflict, wounds and injuries are often susceptible to bacterial infections, and soldiers living in close quarters are at risk of contracting contagious illnesses (Biselli *et al.*, 2022). Military personnel have been experiencing skin-related medical problems for a long time, starting with World War I and persisting through Operation Iraqi

Freedom (Henning & Firoz, 2010). A review revealed that around 27% of dermatological diagnoses documented in combat zones are associated with bacterial or fungal infections (Gelman *et al.*, 2015). In tropical climates such as Vietnam, most infections are aggravated by high temperatures, humidity and limited access to personal hygiene facilities, resulting in heightened vulnerability to skin injuries (U.S. Army Center for Health Promotion and Preventive Medicine, 2005). Moreover, the incidence of dermatophytes or bacterial infections was higher among combat infantry Vietnamese soldiers as compared to Vietnamese soldiers in non-combat support roles (Smith, 1980).

As Malaysia is situated in the same region as Vietnam, it is also easy to be exposed to these infectious diseases. This tropical climate with daily temperature ranging from 21 to 32 °C (Rahman, 2018) is a favourable environment for the growth of bacteria and fungi. Hence, it becomes a threat to humans because this exposure can lead to many diseases that can have detrimental effects on their health. Nazri *et al.* (2020a) identified 13 bacteria species in indoor and outdoor environments at a government premise in Selangor, consisting of some potential pathogenic bacteria. The presence of these bacteria becomes a challenge for the personnel in avoiding illnesses. MAF personnel undoubtedly have high possibility of being exposed to a greater variety of bacteria because they not only live in their camps, but also have a number of outdoor activities at lakes and forests. Hence, there is an urgency to develop antimicrobial garments that are capable of shielding troops from noxious germs and lowering the possibility of infections.

Research on potential pathogenic microorganisms specifically bacteria is crucial to understanding their growth, effects on humans and their survivability in surrounding environments. Gram-negative and Gram-positive bacteria are widely recognised pathogens that can cause diseases other than viruses and fungi. Gram-positive and some Gram-negative organisms have been found to survive in a variety of environmental conditions, such as arid conditions and on various fabrics used in healthcare (Carter, 2005; Kramer *et al.*, 2006; Nazri & Rahim, 2021). Since bacteria require certain environmental conditions to grow and reproduce, their growth concentration is significantly influenced by these factors (Mouli *et al.*, 2005; Nazri *et al.*, 2020b). Temperature, pH and osmotic pressure are some of the factors that influence microbial growth (Isnawati & Trimulyono, 2018).

*Escherichia coli* (*E. coli*), *Staphylococcus aureus* (*S. aureus*) and *Klebsiella pneumoniae* (*K. pneumoniae*) are common bacteria that can be found in the environment and can cause diseases (Breijyeh *et al.*, 2020; Oliveira & Reygaert, 2022). *E. coli* are Gram-negative bacteria that can be normally found in the intestines of humans and some animals (Martinson & Walk, 2020). Scientists have a better understanding of these bacteria than other living microorganisms due to their minimal feeding requirements, rapid development rate and most crucially, well-established genetics (Basavaraju & Gunashree, 2022). Numerous researchers have examined the impact of their antimicrobial textile products using *E. coli* as a test subject (Zhu & Zhang, 2020, Lou *et al.*, 2021; Novoa *et al.*, 2022; Qian *et al.*, 2022). Meanwhile, *S. aureus* are Gram-positive bacteria that is part of the normal microflora of healthy people (Taylor & Unakal, 2022). Many researchers used these bacteria as samples to assess their antimicrobial properties in textile industries due to the ailments caused (Batista *et al.*, 2019; Hanczvikkel *et al.*, 2019; Ibrahim *et al.*, 2021; Feng *et al.*, 2022). *K. pneumoniae* are Gram-negative bacteria that commonly colonise the mucosal surfaces of the oropharynx and gastrointestinal tract in humans (Ashurst & Dawson, 2023). Various studies have been conducted using these bacteria as test samples for antibacterial capabilities (Turalija *et al.*, 2015; Singh & Goyal, 2020; Novi *et al.*, 2022).

Since it is important to lower the risk of infections and protect MAF personnel from harmful microorganisms that can affect their training plans or missions, there has been increased interest in creating fabrics with antimicrobial properties. Numerous studies have been published on the development of antimicrobial textiles for cotton (Zhou *et al.*, 2017; Hanczvikkel *et al.*, 2019; Ketema & Worku, 2020), polyester (Xu *et al.*, 2013; Gressier *et al.*, 2019; Ali *et al.*, 2021), and polyester cotton fabrics (Joshi *et al.*, 2007; Ravindra *et al.*, 2021; Novi *et al.*, 2022). These antimicrobial textiles are categorised based on several classes, whereby one of them is the antimicrobial treatment received and antimicrobial agents used, as well as whether the mechanisms kill (biocide) or inhibit (biostatic) the

growth of the microorganisms (Morais *et al.*, 2016). Metal-based antibacterial agents can be introduced into fabrics during the production or finishing process of the fabric using various methods (Yusop *et al.*, 2023). Metal and metal oxides-based nanoparticles have been widely used as they have demonstrated great antimicrobial properties in recent years, including silver nanoparticle (AgNPs) (Thite *et al.*, 2018; Patil *et al.*, 2019; Ribeiro *et al.*, 2022, Ilieş *et al.*, 2022), zinc oxide nanoparticles (ZnONPs) (Das & Rebecca, 2017; Hassabo *et al.*, 2019; Tania & Ali, 2021), copper nanoparticles (CuNPs) (Sedighi *et al.*, 2014; Ali *et al.*, 2020; Staneva *et al.*, 2021), and titanium dioxide (TiO<sub>2</sub>) (Rashid *et al.*, 2021; Wu, 2022; Jongprateep *et al.*, 2022). The antibacterial properties of metal and metal oxide nanoparticles use a multi-target strategy, whereby they can interfere with DNA while phosphorus- and sulphur-containing substances have capacity to change how permeable cell membranes are, thus making it difficult for bacteria to acquire resistance to them because of this process (Zhang *et al.*, 2022).

In this study, the effects of different antimicrobial solutions against different bacteria when applied on different MAF fabric samples were observed to evaluate the efficacy of the antimicrobial treatments and fabric material usage in reducing the evaluated bacteria. During the evaluation process, three types of fabric samples, namely polyester cotton, polyester and cotton, were sprayed with three types of antimicrobial solutions, Antimicrobials A, B and C, and then the fabric samples were tested using the shake flask method in saline water. This procedure involved soaking the fabric samples in saline water solution containing three specific types of bacteria, *K. pneumoniae*, *S. aureus* and *E. coli*. In order to transfer the bacterial culture onto agar plates, a streaking procedure was conducted after the immersion process. The plates then were placed in an incubator for periods of 0, 1, 3 and 24 h to facilitate bacterial growth. Using a colony counter, every bacterial colony on the plates were counted and recorded for further data analysis.

## 2. MATERIALS AND METHODS

The experiment was conducted using three different types of bacteria, which were *E. coli*, *S. aureus* and *K. pneumoniae*. The three antimicrobial solutions that were tested were Antimicrobials A, which consists of distilled water and TiO<sub>2</sub> with high dodecanoic acid content; Antimicrobial B, which consists of distilled water and TiO<sub>2</sub> with high isopropyl alcohol content; and Antimicrobial C, which consists of distilled water and high heptaethylene glycol with no TiO<sub>2</sub> content. Meanwhile the three different fabric materials from MAF clothes that were tested were polyester cotton, which consists of 63% cotton and 37% polyester, polyester, and cotton. Non-fabric samples were used as control.

In this experiment, the shake flask method was performed in saline to investigate the rate reduction in the number of bacteria. A different medium of saline was used to evaluate the growth of microbes without the addition of other nutrients. Fabric samples were placed in contact with 20 ml of sterile saline (0.85% NaCl) bottles and the fabrics were inoculated with 1 ml of bacterial inoculum. The fabric samples in the bottles were incubated in an incubator shaker at constant temperature of 37 °C. The number of viable cells after incubation was obtained by spread plating serial dilutions on nutrient agar at 0, 1, 3 and 24 h (Singh *et al.*, 2012; Xue *et al.*, 2015).

There were three tests for each bacterium that had been conducted with each antimicrobial solution, as each test needed to follow all the procedures discussed in Sections 2.1 until 2.10. Hence, there were a total of nine tests that needed to be conducted to obtain the required results. All the equipment and medium used in the experiment were sterilised to avoid any contamination before starting the test procedures.

### 2.1 Preparation of Plate Count Agar (PCA) Medium

A total of 17.5 g of PCA powder was weighed and dissolved in 1 L of distilled water in a conical flask. The solution was stirred using a magnetic stirrer at 500 rpm and heated up on a hotplate at 130 °C until



the murk was almost clear. The solution was poured into an autoclave bottle and autoclaved at 121 °C for 15 min. Then, the autoclaved medium solution was poured into each sterile petri dish until the bottle was empty. The agar medium was left to dry at room temperature in laminar air flow and stored in a refrigerator at 4 °C.

## **2.2 Preparation of Nutrient Broth (NB) Medium**

A total of 8 g of NB powder was weighed and dissolved in 1 L of distilled water in a conical flask. The solution was stirred using a magnetic stirrer at 500 rpm and heated up on a hotplate at 130 °C until the murk was almost clear. 9 ml and 20 ml of the solution was pipetted into each empty bottle respectively and autoclaved at 121 °C for 15 min. The bottles were then stored at room temperature.

## **2.3 Preparation of 0.85% Saline Water**

A total of 8.5 g of sodium chloride (NaCl) powder was weighed and dissolved in 1 L of distilled water in a conical flask. The solution was stirred using a magnetic stirrer at 500 rpm and heated up on a hotplate at 130 °C until the murk was almost clear. Volumes of 9 ml and 20 ml of the solution were pipetted into each empty bottle respectively and autoclaved at 121 °C for 15 min. The bottles were then stored at room temperature.

## **2.4 Preparation of Fabric Samples**

All antimicrobial solutions were stored in a refrigerator at 4 °C. Each antimicrobial solution was taken out of the refrigerator and was thawed at room temperature. Three types of fabrics, polyester cotton, polyester and cotton, were prepared with 2 cm width and 5 cm length for each sample. The fabric samples were placed into petri dishes that were labelled accordingly. There were two types of test samples, which were treated and untreated samples. The treated samples were sprayed with Antimicrobials A, B and C, while the untreated samples were not sprayed with any of the antimicrobial solutions. The spraying process was carried out uniformly, and applied to the front and back of the fabrics to ensure thorough distribution. Sterile forceps were used for each sample during the process to prevent cross-contamination. The fabric samples were then dried using a hair dryer for 5 min to ensure that all the sprayed antimicrobial solutions were fully attached to the fabric surfaces. Once the drying process was done, the petri dishes containing the fabric samples were stored in a silica gel desiccator to maintain the dryness of the samples and prevent moisture damage.

## **2.5 Preparation of Bacteria Samples**

A biosafety cabinet was thoroughly sanitised to ensure a clean and safe working environment. Using sterile loops, single colonies of *E. coli* were meticulously selected and transferred into fresh 9 ml NB bottles. The contents of each bottle were gently mixed to ensure homogeneous distribution of the bacterial colonies. This process was repeated for the second and third bottles to ensure adequate supply of bacteria samples. Once prepared, the bottles were placed inside an incubator shaker (New Brunswick Innova® 42R, Germany) to be incubated for 24 h at constant temperature of 37 °C at 110 rpm.

## **2.6 Optical Density (OD) Reading**

OD readings were taken using a spectrophotometer (Eppendorf Biospectrometer, Germany) with a standardised OD value of 0.5 (1 x 10<sup>8</sup> CFU/mL) for the bacteria being tested. A volume 1 ml of each bacteria sample that had been incubated was measured to record the OD readings. A bottle of sample

from each of the three samples was chosen to prepare a new standardised OD value of 0.5. A volume of 1 ml of the newly prepared bacteria from the 0.5 OD bottle was added into three 9 ml bottles of NB and incubated in the incubator shaker (New Brunswick Innova® 42R, Germany) for 3 h at 37 °C and 110 rpm.

## 2.7 Labelling 20 ml of 0.85% Saline Water Bottles

A volume of 20 ml of 0.85% saline water were prepared and labelled accordingly. They were divided into two groups, treated and untreated, with four incubation periods, which were 0, 1, 3 and 24 h. Each fabric sample was placed into 20 ml of saline water according to their respective labels. The non-fabric samples acted as control group.

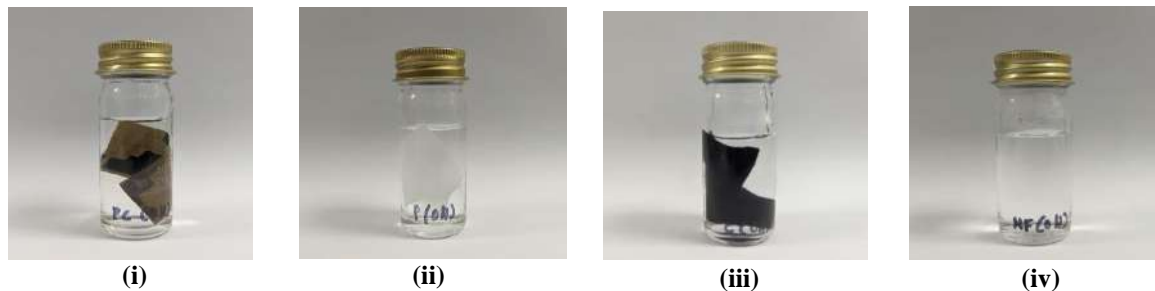


Figure 1: (i) Polyester cotton (PC), (ii) polyester (P), (iii) cotton (C) and (iv) non-fabric (NF) samples.

## 2.8 Bacteria Sample Loading for Testing

After 3 h, 1 ml of the saline water containing bacteria was taken, and two serial dilutions were performed using 9 ml of saline water. A volume of 1 ml from the second dilution was added to 20 ml of saline water containing the fabric samples and control. The saline water, except for the 0 h samples, were incubated in the incubator shaker at 37 °C and 110 rpm, according to the specified time intervals of 1, 3 and 24 h.

## 2.9 Bacterial Testing

Serial dilution was conducted using 9 ml of 0.85% saline water. Three serial dilutions were performed for the treated, untreated and non-fabric samples. Then, 1 ml was taken from each dilution and pipetted into PCA plates. The test samples were evenly spread on the surface of the plates using hockey-stick cell spreaders. All the samples were then incubated in an incubator at 36 °C for 24 h. The bacterial testing process was repeated for the samples at time intervals of 0, 1, 3 and 24 h.

## 2.10 Bacteria Enumeration

After incubation period of 24 h, the sample plates were taken out of the incubator. Colony forming unit (CFU) readings for the 0, 1, 3 and 24 h test samples were counted and recorded using an automatic colony counter (Interscience Scan 4000, USA). Once recorded, the plates were discarded.

### 3. RESULTS AND DISCUSSION

Table 1 shows the CFU readings of the bacteria for three times dilution of each sample that were counted and recorded by the automatic colony counter at 0 and 24 h. Three times dilution results were chosen because most of the other dilution frequency results given by the software programme were between ranges that were too few or too many to count, which could interfere with data accuracy. If there are too few colonies, the count may be inaccurate, while if there are too many colonies, it is difficult and time-consuming to discern the individual colonies on a plate (O'Toole, 2016).

**Table 1: Percentage of reduction of different bacteria on treated (T), untreated (UT) and non-fabric (NF) samples at 0 and 24 h.**

Bacteria	Antimicrobial Solution	Category	Sample	0 h	24 h	Percentage Reduction %	
<i>E. coli</i>	A	T	PC	44.80	0.00	100.00	
			P	341.40	0.00	100.00	
			C	0.00	0.00	0.00	
		UT	PC	431.50	123.20	71.45	
			P	473.10	28.62	93.95	
			C	459.20	175.40	61.80	
	B	T	NF	583.60	1219.00	-108.17	
			PC	73.94	44.62	39.65	
			P	43.66	281.10	-544.16	
		UT	C	5.18	0.00	100.00	
			PC	620.70	94.83	84.72	
			P	1090.00	361.00	66.88	
	C	T	C	134.00	146.20	-9.10	
			NF	596.00	744.30	-24.83	
			PC	85.15	778.70	-815.05	
		UT	P	25.14	0.00	100	
			C	44.20	1674.00	-3697.29	
			PC	516.60	1672.00	-223.65	
	<i>S. aureus</i>	A	T	P	347.40	1026.00	-195.34
				C	167.60	2457.00	-1365.99
				NF	223.10	419.30	-87.96
UT			PC	0.00	0.00	0.00	
			P	650.80	0.00	100.00	
			C	0.00	0.00	0.00	
B		T	PC	135.20	668.60	-394.53	
			P	167.20	25.51	84.74	
			C	117.80	2.43	97.94	
		UT	NF	320.10	0.00	100.00	
			PC	5.21	0.00	100.00	
			P	2.51	1.70	32.27	
C	T	C	57.70	0.00	100.00		
		PC	6.53	407.50	-6140.43		
		P	154.30	196.80	-27.54		
	UT	C	156.80	3724.00	-2275.00		
NF	162.70	1487.00	-814.62				

<i>K. pneumoniae</i>	C	T	PC	1.91	0.00	100.00	
			P	0.00	0.00	0.00	
			C	1.80	0.00	100.00	
		UT	PC	159.30	108.30	32.02	
			P	149.40	11.20	92.50	
			C	116.30	2.45	97.89	
	<i>K. pneumoniae</i>	A	T	PC	0.00	0.00	0.00
				P	13.91	0.00	100.00
				C	0.00	0.00	0.00
			UT	PC	187.20	392.00	-109.40
				P	95.21	523.40	-449.73
				C	236.50	817.10	-245.50
B		T	NF	284.40	0.00	100.00	
			PC	209.00	0.00	100.00	
			P	196.30	0.00	100.00	
		UT	C	79.59	0.00	100.00	
			PC	54.65	906.70	-1559.10	
			P	293.80	723.70	-146.32	
C	T	C	486.70	552.00	-13.42		
		NF	430.50	688.20	-59.75		
		PC	169.10	12.07	92.86		
	UT	P	95.93	18.04	81.20		
		C	112.70	86.22	23.34		
		PC	34.45	76.31	-121.51		
UT	P	102.40	177.20	-73.05			
	C	61.69	156.00	-152.88			
	NF	130.60	179.80	-37.37			

The treated samples were the fabrics that had been sprayed with Antimicrobials A, B, and C using the shake flask test in saline water method. Based on Table 1, the results for the treated samples showed that the combination of Antimicrobials A and B with cotton fabrics were the most effective combination in reducing all the bacteria. The primarily active component in both Antimicrobials A and B is TiO<sub>2</sub>. The addition of this nanoparticle could produce reactive oxygen, leading to oxidative stress that breaks down the bacterial outer membranes and results in phospholipid peroxidation that leads to cell death (Khan *et al.*, 2016; Priyanka *et al.*, 2016). TiO<sub>2</sub> has been proven from previous studies to be able to reduce many potentially pathogenic bacteria, such as *E. coli* (Kangwansupamonkon *et al.*, 2009), *S. aureus* (Chen *et al.*, 2022), *K. pneumoniae* (Jongprateep *et al.*, 2022), *Pseudomonas fluorescens* (Azizi-Lalabadi *et al.*, 2019) and *Listeria monocytogenes* (Azizi-Lalabadi *et al.*, 2019). TiO<sub>2</sub> is an active ingredient that is widely regarded as a natural material, which is classified as biologically inert in humans and animals. This has contributed to its relatively good public acceptance (Skocaj *et al.*, 2011). The active ingredient is the chemical compound accountable for the antimicrobial efficacy of the solution (Vaou *et al.*, 2021). It has recently been found that TiO<sub>2</sub> substance offers the advantages of high stability, non-toxicity and low cost when compared to many other inorganic pigments (Wu, 2022).

However, the effectiveness of Antimicrobial B was less compared to Antimicrobial A. It could be seen that the effectiveness of the combination of Antimicrobial A and cotton fabrics was better because it could totally inhibit all three bacteria at 0 h, where 0.00 CFU reading were recorded. In addition,

Antimicrobial A was proven to remain 100% effective in reducing all bacteria at 24 h even when combined with polyester and polyester cotton fabrics. For the combination of Antimicrobials B and C fabrics, there was still bacterial growth recorded at 0 h, and the effectiveness of Antimicrobial B decreased when combined with polyester and polyester cotton fabrics. Antimicrobial A was more effective due to the addition of high dodecanoic acid content, which is also an antimicrobial agent that helps to inhibit the growth of bacteria (Matsue *et al.*, 2019). This free fatty acid, also known as lauric acid, has potent antimicrobial activity that commonly acts based on lytic behaviour, which is the disruption of cell wall or cell membrane that causes death to bacteria (Jackman *et al.*, 2016). Throughout this study, Antimicrobial C was the most ineffective antimicrobial solution to combat the evaluated bacteria as it did not contain any active ingredient.

From both treated and untreated samples, it could be observed that cotton was the most effective fabric to inhibit bacterial growth, while polyester was the least effective fabric. The results obtained was due the difference physicochemical properties of cotton and polyester that govern the bacterial behaviour. The hydrophobic properties of the textile can affect bacterial attachment directly, and bacterial growth indirectly through its effect on water retention (Mollebjerg *et al.*, 2021). Due to cotton's morphology, which is hydrophilic, the cotton fabrics were able to absorb well the antimicrobial solution during the spraying process as compared to polyester and polyester cotton. As a result, no bacteria could grow on it starting from the 0 h of the test when it was sprayed with Antimicrobial A. The nature of polyester, which has hydrophobic properties (Azeem *et al.*, 2018), increased its availability to bacteria. It was found that bacteria adhere more strongly to more hydrophobic surfaces, due to lower energy barrier to adhesion. Stronger bacterial adhesion drives faster establishment of surface-associated biofilms (Mollebjerg *et al.*, 2021). Cotton was also proven to have higher absorption as compared to polyester cotton (Saleh *et al.*, 2021). Previous studies reported that cotton offers softness and comfort, as well as being stain resistant (Dogbey *et al.*, 2015). It also provides greater air circulation through high air permeability on the skin (Adamu & Gao, 2022), and can also degrade naturally, which makes it environmentally safe (Li *et al.*, 2010). Meanwhile, fabrics made from polyester and their blends retain more perspiration than their natural counterparts. In such cases, there is a greater risk of microbial growth on both human body and textiles. This is because soil, dust, dissolved substances from sweat and some textile finishes can also be sources of nutrients for microorganisms (Purwar & Joshi, 2004; Gao & Cranston, 2008; Simoncic & Tomsic, 2010).

The results from untreated samples showed that there were bacteria that could effectively be reduced in the non-fabric samples. The decrease of CFU readings for the non-fabric samples might due to the 0.85% saline water used in this study that slowed the growth of bacteria in the saline solution, with multiplication by 1 log in 48 h (Goetz *et al.*, 1995). As bacterial growth rate depends on local nutrient concentration, the higher rate of bacterial growth exhausts available nutrient in saline water (Shao *et al.*, 2017). This contributed to the death of the microorganism within 24 h. Besides that, evaporation may have occurred during the agar incubation, resulting in loss of water and subsequently decrease of colony size, which inhibited bacterial growth (Bonnet *et al.*, 2019).

*S. aureus* was the easiest bacteria to be reduced in both the treated and untreated samples, as compared to *E. coli* and *K. pneumoniae*. This is due to the characteristic of *S. aureus* as a Gram-positive bacterium that can be primarily identified by its thick peptidoglycan layer that makes it highly susceptible to reduction due to its ability to easily absorb the antimicrobial solution, and having a wider cell wall, thereby facilitating its vulnerability to be killed (Thiel *et al.*, 2007; Breijyeh *et al.*, 2020; Jubeh *et al.*, 2020). This further demonstrates the peptidoglycan's dynamic character as a macromolecule that continuously remodels in response to varying environmental variables (Irazoki *et al.*, 2019). Thus, this peptidoglycan usually becomes the target of antimicrobial properties, since changes in peptidoglycan structure have direct impact on a variety of activities, including lysozyme resistance (Yadav *et al.*, 2018), host immunological response (Wolf & Underhill, 2018) and antibiotic resistance (Nikolaidis *et al.*, 2014).

For the treated samples, *E. coli* proved to be the most challenging to diminish, while for the untreated samples, *K. pneumoniae* exhibited the most resistant response towards bacterial growth reduction. Previous studies reported that these Gram-negative bacteria need higher antimicrobial emulsion to inhibit growth as compared to Gram-positive bacteria, due to the presence of thin cell wall (Subhapiya & Gomathipriya, 2018; Heidaripour & Sirouskabiri, 2023). They also have an additional membrane called the outer membrane that overlies and covers both the cytoplasmic membrane and peptidoglycan layers. The lipids in the outer membrane are asymmetrically distributed with phospholipids and lipopolysaccharides found in the inner and outer leaflets respectively, thus making it difficult for the antimicrobial to react with its targets (Martinez de Tejada *et al.*, 2012). Hence, it proved that the bactericidal activity outcomes vary depending on the nature of Gram-negative and Gram-positive bacteria due to dissimilarity in their cell wall structure and composition (Silhavy *et al.*, 2010).

#### 4. CONCLUSION

The idea of including antimicrobial properties in military clothes has been encouraged by the recent extensive use of anti-odour, antifungal and antibacterial materials among civilian populations. From the results obtained in the study, Antimicrobial A and cotton fabrics was the most suitable combination in reducing bacterial growth on MAF fabrics. This was due to various factors that caused the inhibition of the bacterial growth, including different compositions of the formulations contained in each of the antimicrobial solution. As can be observed for Antimicrobial A, antimicrobial agent TiO<sub>2</sub> was added with high dodecanoic acid content, which gave significant effect in eradicating the evaluated bacteria. Thus, it showed that the effectiveness of these antimicrobial solutions highly depends on their compositions and active ingredient concentrations. Cotton fabrics are well-known for their cellulosic components that make it more hydrophilic than the other evaluated fabrics, which helped in increasing its antimicrobial response. The study also showed that Gram-negative bacteria is more resistant to antimicrobial activities as compared to Gram-positive bacteria. It can be concluded that the survival of microorganisms is determined by their form and cell integrity to react with the antimicrobial agents' properties.

Although the antimicrobial nanoparticles have been proven to offer promising potential to address issues of public health, infection prevention and people's general well-being, the detailed antibacterial processes of nanoparticles have not been well explored, and it has been found that the same type of nanoparticles can frequently have different antimicrobial activity effects. Hence, further studies need to be conducted focusing on the efficacy of different kind of antimicrobial agents towards various types of clothing, how antimicrobial clothing reduces the spread of disease, and the viability of utilising antimicrobial clothing in different military circumstances. This can ultimately result in a stronger and more effective military force, as well as improved health outcomes for military personnel.

#### 5. REFERENCES

- Adamu, B.F. & Gao, J. (2022). Comfort related woven fabric transmission properties made of cotton and nylon. *Fash. Text.*, **9**: 1-10.
- Ali, A., Baheti, V., Vik, M. & Militky, J. (2020). Copper electroless plating of cotton fabrics after surface activation with deposition of silver and copper nanoparticles. *J. Phys. Chem. Solids*, **137**: 109181.
- Ali, M.A., Aly, N.M. & Abou, E.A.A. (2021). Imparting antibacterial activity, uv-protection properties and enhancing performance of casein modified polyester fabrics. *J. Text. Inst.*, **112**: 1436-1448.
- Ashurst, J.V. & Dawson, A. (2023). *Klebsiella pneumoniae*. Available online at: <https://www.ncbi.nlm.nih.gov/books/NBK519004/> (Last access date: 30 July 2023).
- Azeem, M., Wiener, J. & Khan, M.Z. (2018). Hydrophobic analysis of nano-filament polyester fabric. *Vlak. Text.*, **25**: 5.

- Azizi-Lalabadi, M., Ehsani, A., Divband, B. & Alizadeh-Sani, M. (2019). Antimicrobial activity of titanium dioxide and zinc oxide nanoparticles supported in 4A zeolite and evaluation the morphological characteristic. *Sci. Rep.*, **9**: 17439.
- Basavaraju M. & Gunashree, B.S. (2022). Escherichia coli: an overview of main characteristics. In Eerjavec, M. S. (Ed.), *Escherichia coli - Old and New Insights*. IntechOpen Limited, London, United Kingdom, pp. 1-32.
- Batista, I.R., Prates, A.C.L., De Souza Santos, B., Araújo, J.C.C., De Oliveira, B.Y.C., Rodrigues, M. V.P., Morceli, G., Poletini, J., Cavalleri, A.C., Winkelstroter, L.K. & Pereira, V.C. (2019). Determination of antimicrobial susceptibility and biofilm production in Staphylococcus aureus isolated from white coats of health university students. *Ann. Clin. Microbiol.*, **18**: 1-7.
- Biselli, R., Nisini, R., Lista, F., Autore, A., Lastilla, M., De Lorenzo, G., Peragallo, M.S., Stroffolini, T. & D'Amelio, R. (2022). A historical review of military medical strategies for fighting infectious diseases: from battlefields to global health. *Biomed.*, **10**: 2050.
- Bonnet, M., Lagier, J.C., Raoult, D. & Khelaifia, S. (2019). Bacterial culture through selective and non-selective conditions: the evolution of culture media in clinical microbiology. *New Microbes New Infect.*, **34**: 100622.
- Breijyeh, Z., Jubeh, B. & Karaman, R. (2020). Resistance of gram-negative bacteria to current antibacterial agents and approaches to resolve it. *Molecules*, **25**: 1340.
- Carter, M.J. (2005). Enterically infecting viruses: pathogenicity, transmission and significance for food and water borne infections. *J. Appl. Microbiol.*, **98**: 1354-1380.
- Chen, W., Feng, X., Zhang, D., Lu, F., Wang, H., Tan, J., Xu, Q., Liu, Y., Cao, Z. & Su, X. (2022). In situ synthesis of TiO<sub>2</sub>/NC on cotton fibers with antibacterial properties and recyclable photocatalytic degradation of dyes. *RSC Adv.*, **12**: 19974-19980.
- Das, M.P. & Rebecca, L.J. (2017). Evaluation of antibacterial efficacy of biogenic zinc oxide nanoparticles on cotton fabrics. *J. Pharm. Sci. Res.*, **9**: 2553-2557.
- Dogbey, R., Kpobee, M.K., Dedume, V. & Osei, J. (2015). The effect of fabrics and designs on the physical comfort of children clothes in the Accra Metropolis. *Choice*, **30**.
- Feng, J., Feng, L., Xu, S., Zhu, C., Pan, G. & Yao, L. (2022). Universal preparation strategy for ultradurable antibacterial fabrics through coating an adhesive nanosilver glue. *Nanomaterials*, **12**: 2429.
- Gao, Y. & Cranston, R. (2008). Recent advances in antimicrobial treatments of textiles. *Text. Res. J.*, **78**: 60-72.
- Gelman, A.B., Norton, S.A., Valdes-Rodriguez, R. & Yosipovitch, G. (2015). A review of skin conditions in modern warfare and peacekeeping operations. *Mil. Med.*, **180**: 32-37.
- Goetz, A. M., Rihs, J.D., Chow, J.W., Singh, N. & Muder, R.R. (1995). An outbreak of infusion related Klebsiella pneumoniae bacteraemia in a liver transplantation unit. *Clin. Infect. Dis.*, **21**: 1501-1503.
- Gressier, P., De Smet, D., Behary, N., Campagne, C. & Vanneste, M. (2019). Antibacterial polyester fabrics via diffusion process using active bio-based agents from essential oils. *Ind. Crops Prod.*, **136**: 11-20.
- Hanczvikkel, A., Víg, A. & Tóth, Á. (2019). Survival capability of healthcare-associated, multidrug-resistant bacteria on untreated and on antimicrobial textiles. *J. Ind. Text.*, **48**: 1113-1135.
- Hassabo, A.G., El-Naggar, M.E., Mohamed, A.L. & Hebeish, A.A. (2019). Development of multifunctional modified cotton fabric with tri-component nanoparticles of silver, copper and zinc oxide. *Carbohydr. Polym.*, **210**: 144-156.
- Heidaripour, A. & Sirouskabiri, B. (2023). Gram-positive and gram-negative antibacterial activity in textiles impregnated with OA-g-CSO copolymer. *Asian J. Green Chem.*, **7**: 229-238.
- Henning, M.J.S. & Firoz, B.F. (2010). Combat dermatology: the prevalence of skin disease in a deployed dermatology clinic in Iraq. *J. Drugs. Dermatol.*, **9**: 210-214.
- Ibrahim, A., Laquerre, J.-É., Forcier, P., Deregnacourt, V., Decaens, J. & Vermeersch, O. (2021). Antimicrobial agents for textiles: types, mechanisms and analysis standards. In Kumar, B. (Ed.), *Textiles for Functional Applications*, IntechOpen Limited, London, United Kingdom, pp. 13-42.
- Ilieş, A., Hodor, N., Pantea, E., Ilieş, D.C., Indrie, L., Zdrîncă, M., Lancu, S., Caciora, T., Chiriac, A., Gherghel, C., Taghiyari, H.R., Costea, M. & Baias, Ş. (2022). Antibacterial effect of eco-friendly

- silver nanoparticles and traditional techniques on aged heritage textile, investigated by dark-field microscopy. *Coatings*, **12**: 1688.
- Irazoki, O., Hernandez, S.B. & Cava, F. (2019). Peptidoglycan muropeptides: release, perception, and functions as signalling molecules. *Front. Microbiol.*, **10**: 500.
- Isnawati & Trimulyono, G. (2018). Temperature range and degree of acidity growth of isolate of indigenous bacteria on fermented feed “fermege”. *J. Phys. Conf. Ser.*, **953**: 012209.
- Jackman, J.A., Yoon, B.K., Li, D. & Cho, N.J. (2016). Nanotechnology formulations for antibacterial free fatty acids and monoglycerides. *Molecules*, **21**: 305.
- Jongprateep, O., Mani-Lata, C., Sakunrak, Y., Audcharuk, K., Narapong, T., Janbooranapinij, K., Pitiphatharabun, S., Lertworasirikul, A., Laobuthee, A., Thengchaisri, S., Ajiro, H., Yoshida, H. & Panomsuwan, G. (2022). Titanium dioxide and fluoropolymer-based coating for smart fabrics with antimicrobial and water-repellent properties. *RSC Adv.*, **12**: 588-594.
- Joshi, M., Ali, S.W. & Rajendran, S. (2007). Antibacterial finishing of polyester/cotton blend fabrics using neem (*Azadirachta indica*): a natural bioactive agent. *J. Appl. Polym. Sci.*, **106**: 793-800.
- Jubeh, B., Breijyeh, Z. & Karaman, R. (2020). Resistance of gram-positive bacteria to current antibacterial agents and overcoming approaches. *Molecules*, **25**: 2888.
- Kangwansupamonkon, W., Lauruengtana, V., Surassmo, S. & Ruktanonchai, U. (2009). Antibacterial effect of apatite-coated titanium dioxide for textiles applications. *Nanotechnol. Biol. Med.*, **5**: 240-249.
- Ketema, A. & Worku, A. (2020). Antibacterial finishing of cotton fabric using stinging nettle (*Urtica dioica* L.) plant leaf extract. *J. Chem.*, **2020**: 1-10.
- Khan, S.T., Ahmad, J., Ahamed, M., Musarrat, J. & Al-Khedhairi, A.A. (2016). Zinc oxide and titanium dioxide nanoparticles induce oxidative stress, inhibit growth, and attenuate biofilm formation activity of *Streptococcus mitis*. *J. Biol. Inorg. Chem.*, **21**: 295-303.
- Kramer, A., Schwebke, I. & Kampf, G. (2006). How long do nosocomial pathogens persist on inanimate surfaces? a systematic review. *BMC Infect. Dis.*, **6**: 130.
- Li, L., Frey, M., & Browning, K.J. (2010). Biodegradability study on cotton and polyester fabrics. *J. Eng. Fibers Fabr.*, **5**: 2010.
- Lou, C.W., Hsieh, M.C., Lai, M.F., Lee, M.C. & Lin, J.H. (2021). Functional antibacterial nanometer zinc ion yarns: manufacturing technique and antimicrobial efficacy against *Escherichia coli*. *Appl. Sci.*, **11**: 5021.
- Martinez de Tejada, G., Sánchez-Gómez, S., Rázquin-Olazarán, I., Kowalski, I., Kaconis, Y., Heinbockel, L. & Brandenburg, K. (2012). Bacterial cell wall compounds as promising targets of antimicrobial agents I. antimicrobial peptides and lipopolyamines. *Curr. Drug. Targets*, **13**: 1121-1130.
- Martinson, J.N.V. & Walk, S.T. (2020). *Escherichia coli* residency in the gut of healthy human adults. *EcoSal. Plus.*, **9**: 1-27.
- Matsue, M., Mori, Y., Nagase, S., Sugiyama, Y., Hirano, R., Ogai, K., Ogura, K., Kurihara, S. & Okamoto, S. (2019). Measuring the antimicrobial activity of lauric acid against various bacteria in human gut microbiota using a new method. *Cell Transplant.*, **28**: 1528-1541.
- Mollebjerg, A., Palmén, L.G., Gori, K. & Meyer, R.L. (2021). The bacterial life cycle in textiles is governed by fiber hydrophobicity. *Microbiol. Spectr.*, **9**: e01185-21.
- Morais, D.S., Guedes, R.M. & Lopes, M.A. (2016). Antimicrobial approaches for textiles: from research to market. *Materials*, **9**: 498.
- Mouli, P.C., Mohan, S.V. & Reddy, S.J. (2005). Rainwater chemistry at a regional representative urban site: influence of terrestrial sources on ionic composition. *Atmos. Environ.*, **39**: 999-1008.
- Nazri, N.N.I.M., Hamid, A.N.A. & Aminuddin, N.A. (2020a). Bioaerosol sampling and identification of airborne bacteria in indoor and outdoor environments. *Def. S. T. Tech. Bull.*, **13**: 142-153.
- Nazri, N.N.I.M., Hamid, A.N.A., Aminuddin, N.A., Jusoh, A. & Rahim, N.H.Z.A. (2020b). Indoor and outdoor bioaerosol sampling and bacterial counting analysis. *Def. S. T. Tech. Bull.*, **13**: 130-141.
- Nazri, N.N.I.M. & Rahim, N.H.Z.A. (2021). Detection and quantification of bacteria on frequently touched surfaces at a workplace. *Def. S. T. Tech. Bull.*, **14**: 164-171.
- Nikolaidis, I., Favini-Stabile, S. & Dessen, A. (2014). Resistance to antibiotics targeted to the bacterial cell wall. *Protein Sci.*, **23**: 243-259.



- Novi, V. T., Gonzalez, A., Brockgreitens, J. & Abbas, A. (2022). Highly efficient and durable antimicrobial nanocomposite textiles. *Sci. Rep.*, **12**: 17332.
- Novoa, C.C., Tortella, G., Seabra, A.B., Diez, M.C. & Rubilar, O. (2022). Cotton textile with antimicrobial activity and enhanced durability produced by l-cysteine-capped silver nanoparticles. *Processes.*, **10**: 958.
- Oliveira, J. & Reygaert, W.C. (2022). *Gram-negative Bacteria*. Available online at: <https://www.ncbi.nlm.nih.gov/books/NBK538213/> (Last access date: 30 July 2023).
- O'Toole, G.A. (2016). Classic spotlight: plate counting you can count on. *J. Bacteriol.*, **198**: 3127-3127.
- Patil, A.H., Jadhav, S.A., Gurav, K.D., Waghmare, S.R., Patil, G.D., Jadhav, V.D., Vhanbatte, S.H., Kadole, P.V., Sonawane, K.D. & Patil, P.S. (2019). Single step green process for the preparation of antimicrobial nanotextiles by wet chemical and sonochemical methods. *J. Text. Inst.*, **111**: 1380-1388.
- Priyanka, K.P., Sukirtha, T.H., Balakrishna, K.M. & Varghese, T. (2016). Microbicidal activity of TiO<sub>2</sub> nanoparticles synthesised by sol-gel method. *IET Nanobiotechnol.*, **10**: 81-86.
- Purwar, R. & Joshi, M. (2004). Recent developments in antimicrobial finishing of textiles: a review. *AATCC Rev.*, **4**: 22-26.
- Qian, J., Dong, Q., Chun, K., Zhu, D., Zhang, X., Mao, Y., Culver, J.N., Tai, S., German, J.R., Dean, D.P., Miller, J.T., Wang, L., Wu, T., Li, T., Brozena, A.H., Briber, R.M., Milton, D.K., Bentley, W.E. & Hu, L. (2022). Highly stable, antiviral, antibacterial cotton textiles via molecular engineering. *Nat. Nanotechnol.*, **18**: 168-176.
- Rahman, H.A. (2018). Climate change scenarios in Malaysia: engaging the public. *IJoM-NS*, **1**: 55-77.
- Rashid, M.M., Simončič, B. & Tomšič, B. (2021). Recent advances in TiO<sub>2</sub>-functionalized textile surfaces. *Surf. Interfaces*, **22**: 100890.
- Ravindra, K.B., Dinesh. Y.N. & Sekhara S.M.C. (2021). Antimicrobial properties of cotton and polyester/cotton fabrics treated with natural extracts. *Asian J. Text.*, **11**: 1-6.
- Ribeiro, A.I., Shvalya, V., Cvelbar, U., Silva, R., Marques-Oliveira, R., Remião, F., Felgueiras, H.P., Padrão, J. & Zille, A. (2022). Stabilization of silver nanoparticles on polyester fabric using organo-matrices for controlled antimicrobial performance. *Polymers*, **14**: 1138.
- Saleh, S.N., Khaffaga, M.M., Ali, N.M., Hassan, M.S., El-Naggar, A.W.M. & Rabie, A.G.M. (2021). Antibacterial functionalization of cotton and cotton/polyester fabrics applying hybrid coating of copper/chitosan nanocomposites loaded polymer blends via gamma irradiation. *Int. J. Biol. Macromol.*, **183**: 23-34.
- Sedighi, A., Montazer, M. & Hemmatinejad, N. (2014). Copper nanoparticles on bleached cotton fabric: in situ synthesis and characterization. *Cellulose*, **21**: 2119-2132.
- Shao, X., Mugler, A., Kim, J., Jeong, H.J., Levin, B.R. & Nemenman, I. (2017). Growth of bacteria in 3-d colonies. *PLoS Comput. Biol.*, **13**: e1005679.
- Silhavy, T. J., Kahne, D. & Walker, S. (2010). The bacterial cell envelope. *Cold Spring Harb. Perspect. Biol.*, **2**: a000414.
- Simoncic, B. & Tomsic, B. (2010). Structure of novel antimicrobial agents for textiles: a review. *Text. Res. J.*, **80**: 1721-1737.
- Singh, G., Joyce, E.M., Beddow, J. & Mason, T.J. (2012). Evaluation of antibacterial activity of ZnO nanoparticles. *J. Microbiol. Biotechnol. Food Sci.*, **2**: 106-120.
- Singh, P.K. & Goyal, M. (2020). Green synthesis using *Klebsiella pneumoniae* as well as its execution onto textiles for microbe resistance. *Mater. Sci. Eng.*, **988**: 012071.
- Skocaj, M., Filipic, M., Petkovic, J. & Novak, S. (2011). Titanium dioxide in our everyday life; is it safe?. *Radiol. Oncol.*, **45**: 227-247.
- Smith, J.G. (1980). Medical department, United States army-internal medicine in Vietnam, vol 1: skin diseases in Vietnam, 1965-72. *J. Am. Med. Assoc.*, **244**: 839-839.
- Staneva, D., Atanasova, D., Nenova, A., Vasileva-Tonkova, E & Grabchev, I. (2021). Cotton fabric modified with a pamam dendrimer with encapsulated copper nanoparticles: antimicrobial activity. *Materials*, **14**: 7832.
- Subhapiya, S. & Gomathipriya, P.J.M.P. (2018). Green synthesis of titanium dioxide (TiO<sub>2</sub>) nanoparticles by *Trigonella foenum-graecum* extract and its antimicrobial properties. *Microb. Pathog.*, **116**: 215-220.

- Tania, I.S. & Ali, M. (2021). Coating of ZnO nanoparticle on cotton fabric to create a functional textile with enhanced mechanical properties. *Polymers*, **13**: 2701.
- Taylor, T.A. & Unakal, C.G. (2022). *Staphylococcus aureus Infection*. Available online at: <https://www.ncbi.nlm.nih.gov/books/NBK441868/> (Last access date: 30 July 2023).
- Thiel, J., Pakstis, L., Buzby, S., Raffi, M., Ni, C., Pochan, D.E. & Shah, S.I. (2007). Antibacterial properties of silver-doped titania. *Small*, **3**: 799-803.
- Thite, A.G., Krishnanand, K., Sharma, D.K. & Mukhopadhyay, A.K. (2018). Multifunctional finishing of cotton fabric by electron beam radiation synthesized silver nanoparticles. *Radiat. Phys. Chem.*, **153**: 173-179.
- Turalija, M., Merschak, P., Redl, B., Griesser, U., Duelli, H. & Bechtold, T. (2015). Copper (I) oxide microparticles—synthesis and antimicrobial finishing of textiles. *J. Mater. Chem. B.*, **3**: 5886-5892.
- U. S. Army Center for Health Promotion and Preventive Medicine (2005). *Diagnosis and Treatment of Diseases of Tactical Importance to U. S. Central Command*. USACHPPM., Washington, United States.
- Vaou, N., Stavropoulou, E., Voidarou, C., Tsigalou, C. & Bezirtzoglou, E. (2021). Towards advances in medicinal plant antimicrobial activity: a review study on challenges and future perspectives. *Microorganisms*, **9**: 2041.
- Wolf, A.J. & Underhill, D.M. (2018). Peptidoglycan recognition by the innate immune system. *Nat. Rev. Immunol.*, **18**: 243-254.
- Wu, X. (2022). Applications of titanium dioxide materials. In Ali, H. M. (Ed.), *Titanium Dioxide-Advances and Applications*, IntechOpen Limited, London, United Kingdom, pp. 45-47.
- Xu, H., Shi, X., Lv, Y. & Mao, Z. (2013). The preparation and antibacterial activity of polyester fabric loaded with silver nanoparticles. *Text. Res. J.*, **83**: 321-326.
- Xue, Y., Xiao, H. & Zhang, Y. (2015). Antimicrobial polymeric materials with quaternary ammonium and phosphonium salts. *Int. J. Mol. Sci.*, **16**: 3626-3655.
- Yadav, A.K., Espallat, A. & Cava, F. (2018). Bacterial strategies to preserve cell wall integrity against environmental threats. *Front. Microbiol.*, **9**: 2064.
- Yusop, H.M., Ismail, W.N.W., Zulkifli, N.F.M & Tajuddin, S.N. (2023). *Effect of CuO antibacterial coating on cotton, polyester, and blend wool fabrics*. *Biointerface Res. Appl. Chem.*, **13**: 591 .
- Zhang, S., Lin, L., Huang, X., Lu, Y. & Zheng, D. (2022). Antimicrobial properties of metal nanoparticles and their oxide materials and their applications in oral biology. *J. Nanomater.*, **Vol. 2022**: 1-18.
- Zhou, C.E., Kan, C.W., Matinlinna, J.P. & Tsoi, J.K.H. (2017). Regenerable antibacterial cotton fabric by plasma treatment with dimethylhydantoin: antibacterial activity against *S. aureus*. *Coatings*, **7**: 11.
- Zhu, Y. & Zhang, S. (2020). Antibacterial activity and mechanism of lacidophilin from *Lactobacillus pentosus* against *Staphylococcus aureus* and *Escherichia coli*. *Front. Microbiol.*, **11**: 582349.

# COMPARISON OF MOISTURE MANAGEMENT PROPERTIES FOR MALAYSIAN GOVERNMENT UNIFORMS

Nurul Hidayah Abdul Aziz\* , Ikhwan Muaz Abd Rahman, Nor Hafizah Mohd Jais, Wan Elyn Amira  
Wan Adnan & Mohd Faris Mohd Rudi

Protection and Biophysical Technology Division (BTPB), Science and Technology Research Institute for  
Defence (STRIDE), Ministry of Defence, Malaysia

\*Email: hidayah.aziz@stride.gov.my

## ABSTRACT

*This paper explores the impact of fabric materials and compositions on moisture management in government clothings, particularly focusing on comfort, which is vital for uniforms of enforcement agencies and military in Malaysia. By choosing the right materials, protective clothing can enhance wearer satisfaction and protection. We evaluated nine fabric types for their moisture management performance, which involved transporting moisture (such as sweat) away from the body for quick evaporation in order to maintain wearer comfort. Among these fabrics, sample K06 (100% polyester) proved to be the most comfortable, excelling in efficient moisture transport without causing discomfort. In contrast, sample K02 (60% cotton, 40% polyester) was the least comfortable due to bottom coating that traps sweat. If coated fabrics were excluded, sample K05 (70% cotton, 30% nylon) was the least comfortable due to its thickness. The study also highlighted that 100% polyester fabrics outperformed 100% cotton fabrics in moisture management. Furthermore, lower mass per unit area and increasing cotton composition in cotton-nylon blends improve overall moisture management properties.*

**Keywords:** *Fabric comfort; moisture management properties; material composition; fabric mass; thickness.*

## 1. INTRODUCTION

One of the most important aspects that need to be considered before manufacturing textiles is to evaluate the thermophysiological comfort properties of the fabric for the wearer. Thermophysiology can be referred to as the body's ability to regulate the thermal environment, and coordinate the production and loss of body heat. These properties are influenced by environmental factors such as air movement, humidity and temperature, as well as how the fabric interacts with the body (Kamalha *et al.*, 2013). In the pursuit of optimal comfort, maintaining core body temperature of 37 °C plays a crucial role. Deviations from this ideal temperature can result in discomfort, disrupting the body's thermophysiological balance and if prolonged may lead to various health issues (Motlogelwa, 2018). Therefore, understanding and addressing the factors that influence thermophysiological comfort are crucial for ensuring the well-being and comfort of individuals that wear the textiles.

Additionally, thermophysiological comfort properties of textiles directly interact with the body's thermoregulatory system, thereby influencing the overall comfort and well-being of the wearer. When fabrics possess optimal thermophysiological comfort properties, they can enhance the thermoregulatory system's ability to maintain a stable body temperature in varying environmental conditions and activities. Thermoregulatory system is a mechanism to maintain body temperature with tightly controlled self-

regulation independent of external temperatures and can protect itself when feeling cold or hot (Osilla *et al.*, 2023). For instance, during a workout session, as the body temperature rises, the skin responds by releasing sweat to facilitate body cooling. The evaporation of sweat, which is a highly effective cooling process, helps the human body to dissipate heat and lower the temperature of the skin (Zou *et al.*, 2021).

Clothing is crucial for supporting the body's thermoregulation, but fabrics with poor thermophysiological comfort can cause discomfort. Wet, sweat-soaked clothing can be unpleasant, heavy, sticky, and restrict movement and breathability. Since the excess sweat cannot effectively be removed from the fabric, wearers may feel damp and cold after their activity, experiencing discomfort from the after-chill effect (Zou *et al.*, 2021). In order to evaluate these properties, various factors come into play, with moisture management being key. Moisture management properties refer to the controlled movement of liquid (perspiration) from the skin surface to the environment through the fabric (Chinta *et al.*, 2013). It is an important factor in optimising comfort and maximising performance of the fabric (Motlogelwa, 2018). The main objectives of achieving excellent moisture management properties in a fabric are to facilitate the rapid transport of humidity to the atmosphere and promote its evaporation, thereby making the skin feel dry (Basuk *et al.*, 2018).

In order to objectively measure the moisture management properties of textile fabrics, moisture management tests (MMT) are conducted following AATCC TM195-2011e2(2017)e3: Test Method for Liquid Moisture Management Properties of Textile Fabrics. The fabrics are evaluated on two sides, which are the top and bottom. The top is the part of the fabric that comes into contact with the wearer's sweat and skin, while the bottom is the part of the fabric that is exposed to the atmosphere.

The test evaluates several parameters, including wetting time (top / bottom), absorption rate (top / bottom), maximum wetted area (top / bottom), spreading speed (top / bottom), one-way transport index and overall moisture management capacity (OMMC), to determine the appropriateness of fabrics for different apparel end uses. Each of these factors are graded according to the AATCC standard. According to Basuk *et al.* (2018), the data obtained from the MMT can be used to classify the fabrics, as presented in Table 1. In addition, moisture management properties are influenced by type of yarn, material composition, fabric construction, thickness and mass per unit area (Messiry *et al.*, 2015; Suganthi & Senthilkumar, 2017; Motlogelwa, 2018).

Generally, there are two types of yarn used in textile production, which are natural and synthetic yarns. Natural yarns, such as cotton, wool, silk, and bamboo, originate from plants or animals. Synthetic yarns, such as polyester and nylon, are chemically synthesised by humans. Typically, natural yarn is used for general sports clothing and streetwear, while synthetic yarn is preferred for high-performance sportswear and textiles (Motlogelwa, 2018; Basuk *et al.*, 2018). Natural yarn textiles tend to offer greater comfort for daily wear and everyday activities (Basuk *et al.*, 2018). However, for intense physical activities that lead to increased sweat production, synthetic fibres with low moisture retention due to their hydrophobic properties are favoured. These fibres remain dry, and facilitate moisture transport and release efficiently (Onofrei *et al.*, 2011; Zou *et al.*, 2021). In contrast, natural yarns, being hydrophilic, tend to retain water within their fibres, resulting in poor moisture transport and release (Onofrei *et al.*, 2011).

Blended yarn, created by combining two or more fibres, enhances product quality by achieving specific properties for a defined purpose. Blending is especially valuable when natural and synthetic fibre vary in characteristics and quality. It allows for consistency and uniformity (Mahmoudi, 2010). Blended yarn can influence textile moisture management properties. For example, according to Namligöz *et al.* (2010), natural / synthetic blends exhibited very good accumulative one-way transport index (AOTI) values, indicating high performance. However, fabrics made solely from natural fibres have limited AOTI values (Namligöz *et al.*, 2010). Furthermore, material composition within the yarn also impacts moisture management properties (Motlogelwa, 2018). From the study of Vidhya *et al.* (2022), blended yarn of cotton

and polyester improves moisture management properties when the percentage of polyester in the blended yarn increases.

**Table 1: Type of fabric according to its properties (Basuk *et al.*, 2018).**

No.	Type of fabric	Properties
1.	Water Proof Fabric	Very slow absorption Slow spreading No one-way transport, no penetration
2.	Water Repellent Fabric	No wetting No absorption No spreading Poor one-way transport without external forces
3.	Slow Absorbing and Slow Drying Fabric	Slow absorption Slow spreading Poor one-way transport
4.	Fast Absorbing and Slow Drying Fabric	Medium to fast wetting Medium to fast absorption Small spreading area Slow spreading Poor one-way transport
5.	Fast Absorbing and Quick Drying Fabric	Medium to fast wetting Medium to fast absorption Large spreading area Fast spreading Poor one-way transport
6.	Water Penetration Fabric	Small spreading area Excellent one-way transport
7.	Moisture Management Fabric	Medium to fast wetting Medium to fast absorption Large spread area at bottom surface Fast spreading at bottom surface Good to Excellent one-way transport

This study is aimed at evaluating the moisture management performance of nine fabric samples from Malaysian government uniforms. These fabrics would have differences in terms of their properties, such as type of yarn, material composition, fabric construction, thickness and mass per unit area. The study also aims to identify the most suitable materials for achieving the required level of comfort.

## 2. MATERIALS AND METHOD

### 2.1 Preparation of Fabric Samples

In this study, nine fabrics from government uniforms were used. The names of the agencies were hidden due to confidentiality. All of the fabric samples were provided by the Textile Analysis & Technology Branch (CATT), Science & Technology Research Institute for Defence (STRIDE), and were coded from K01 to K09 (Table 2). Each fabric was cut at  $8 \times 8$  cm diagonally across the width of sample to ensure a standard set of length and width of yarns for the samples. In addition, five samples were prepared for each fabric to collect average data during the MMT test.

**Table 2: Physical properties of the fabric samples.**

<b>Sample</b> <b>Properties</b>	<b>Material Composition</b>	<b>Mass/Unit Area (g/m<sup>2</sup>)</b>	<b>Construction</b>	<b>Thickness (mm)</b>
K01	80C20N	248	Ripstop 3X3	0.52
K02	60C40P	224	Ripstop 3X3	0.49
K03	30C70P	229	Ripstop 3X3	0.45
K04	100C	208	Ripstop 3X3	0.43
K05	70C30N	241	Ripstop 3X3	0.69
K06	100P	174	Twill 2/2	0.41
K07	100P	185	Twill 2/2	0.39
K08	100C	240	Twill 3/1	0.57
K09	30C70P	114	Plain	0.26

Note: C = Cotton, N = Nylon and P = Polyester.

## 2.2 Sample Laundering

All of the samples were hand-laundered using STRIDE's in-house method. The samples were placed in a beaker containing home detergent and stirred for 15 min, then left to soak for 30 min. The samples were then dried on a flat, smooth, horizontal surface without tension.

## 2.3 Fabric Sample Conditioning

Before the MMT test was run, the samples were placed on a flat smooth, horizontal surface without tension to condition them to moisture equilibrium in an environment that was controlled at  $21 \pm 2^\circ\text{C}$  and  $65 \pm 5\%$  relative humidity (RH) as recommended by ASTM D1776: Standard Practice for Conditioning and Testing Textile.

## 2.4 Preparation of Test Solution

The solution was prepared by dissolving 9 g of sodium chloride in 1 L of distilled water and its electrical conductivity was adjusted to  $16 \pm 0.2$  milli Siemens (mS) at  $25^\circ\text{C}$  by adding sodium chloride or distilled water as necessary. The purpose of the solution was to provide a conductive medium for the instrument's sensors and not for the purpose of duplication of perspiration.

## 2.5 Moisture Management Test (MMT)

The MMT test was conducted following AATCC TM195-2011e2(2017)e3: Test Method for Liquid Moisture Management Properties of Textile Fabrics. Initially, the MMT start up, addition of test solution and the computer software's setup to collect the test data were done by following the instructions given by the manufacturer, which is SDL ATLAS.

After that, the upper sensor was raised to its locked position and a paper towel was placed on the lower sensor. The "Pump" button was pressed for 1 to 2 min until 0.22 cc of test solution was drawn from the container and dripped onto the paper towel, ensuring no air bubbles were present inside the tubing. The paper towel was then removed.

Then, the conditioned sample was placed on the lower sensor with the specimen's top surface up. The upper sensor was released until it freely rested on the sample and the door of the tester was shut. The "Pump-On Time" was set at 20 s to assure the predetermined amount (0.22 cc) of test solution was dispensed. For each sample, the percentage (%) of water content was set to 0.0 at the beginning of each test on the graph to avoid inaccurate test results. The "Measure Time" was set for 120 s and the test was started. At the end of the 120 s test time, the software automatically stopped the test and calculated all of the indices. Then, the upper sensor was raised and the test sample was removed.

Before inserting the next sample, the upper sensor was kept in its locked position. The area between the rings of pins on both the upper and lower sensors was dried using white AATCC textile blotting paper or a soft paper towel cut into narrow (0.5 cm) strips. A waiting period of 1 min or longer was observed to ensure that no residual test solution was present on the sensors. Otherwise, any remaining moisture would have caused an erroneous start. If salt deposits were observed on the sensors after drying, distilled water was used to remove them. After all of the samples were tested, distilled water was used to clean and purge the pump and tubing.

## 3. RESULTS AND DISCUSSION

### 3.1 Wetting Time

Wetting is the initial process involved in fluid spreading, where the fibre-air interface is replaced with a fibre-liquid interface. According to Basuk *et al.* (2018), wetting time for the top and bottom surfaces is defined as the time in seconds (s) when the slope of total water content at the top and bottom surfaces becomes greater than  $\tan(15^\circ)$  after the test begins. It represents the time taken to wet the top and bottom surfaces of the material after the initiation of the test or when exposed to moisture. From the grading scheme in accordance with AATCC TM195-2011e2(2017)e3, the longer the wetting time, the worse the fabric performs in terms of wettability. The wetting time values and grades for the samples are depicted in Figure 1.

Based on Figure 1 data, sample K07, consisting of 100% polyester with 2/2 twill construction, achieved the highest wetting time grade of 5 for both surfaces, as well as the lowest wetting times of 2.77 and 2.83 s, indicating excellent wetting time performance for both surfaces. Similarly, sample K06, also 100% polyester with the same weave, displayed excellent performance on its bottom surface with wetting time of 2.83 s, with grade 5 rating. Its top surface, while slightly slower, still exhibited commendable wetting time of 3.18 s, earning a grade 4 rating. Sample K08 demonstrated excellent wetting time performance for the top surface (2.85 s, grade 5) and fast wetting time performance for the bottom surface (3.03 s, grade 4).

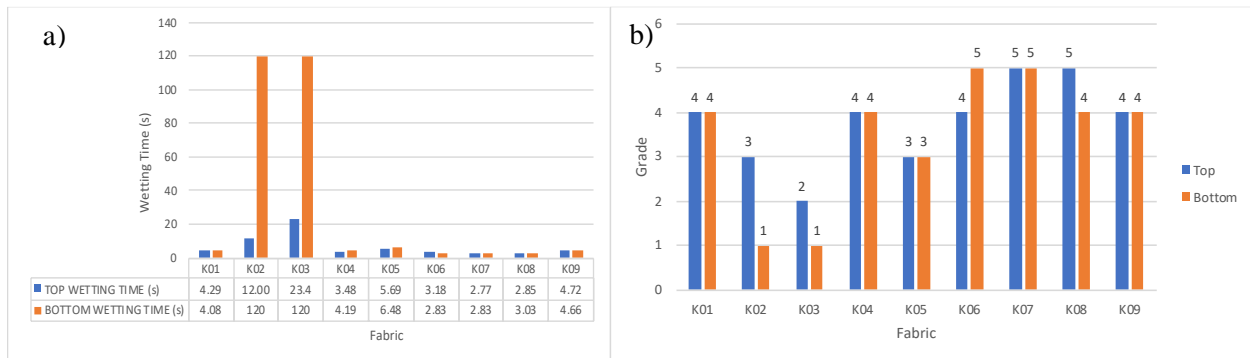


**Figure 1: (a) Wetting times and (b) wetting time grades of the fabric samples.**

The efficiency of wettability (wetting) is usually determined by the choice of yarn and fabric construction (Senthilkumar *et al.*, 2013). In this study, samples K07, K06 and K08 stand out as having the best wetting time performance among the other samples, which can be attributed to their fabric constructions. Samples K07 and K06 feature twill 2/2 construction, while K08 has twill 3/1 construction. These findings suggest that the twill 2/2 and 3/1 constructions contribute to higher wettability results in the fabric samples. Previous studies have reported that the 3/1 twill weave design is more porous than the 1/1 plain weave design (Umair *et al.*, 2016).

Furthermore, the wetting time is the slowest on the bottom surface of samples K02 and K03, with times of 120 s each, indicating no wetting (grade 1) occurred on the surface. These fabrics could be used for specific operations and missions that require coated fabrics to adapt with different climate environments. Additionally, the results reveal that cotton blended with polyester tends to exhibit low wetting time performance, as seen for samples K02 and K03 (only for the top surface). However, sample K09 demonstrated very good wetting time performance, which could be attributed to its mass per unit area and fabric thickness with values of 114 g/m<sup>2</sup> and 0.26 mm respectively, as well as its plain weave construction. In the comparison with samples of 3x3 ripstop construction, sample K04, which consists of 100% cotton, showed shorter wetting time than the blended fabrics (samples K01, K02, K03 and K05) on the top surface. Conversely, sample K01, a cotton-nylon blend with composition of 80% cotton and 20% nylon, had shorter wetting time than other samples on the bottom surface.

As for the cotton-polyester blends (samples K02 and K03), the wetting times show grades 3 and 2 respectively on the top surface. This is attributed to the hydrophobic property of polyester fibres, which only absorb a small amount of water and create more liquid water transfer channels through wicking force (Senthilkumar *et al.*, 2013). Additionally, it can be observed that higher cotton content leads to increased absorption and shorter wetting time. This trend is evident in the comparison between samples K01 (80% cotton and 20% nylon) and K05 (70% cotton and 30% nylon), where the higher cotton content in K01 contributes to better wetting time performance as compared to sample K05.

When comparing the results of thin and thick fabrics made of the same material, it is evident that thinner fabrics exhibit faster wetting than thicker ones when equal amounts of water are applied (Karthikeyan *et al.*, 2016). This observation is also reflected in Table 2 and Figure 1, which show a decrease in wetting time grade from 4 to 3 (i.e., from fast to medium) with an increase in thickness for cotton blended with nylon material (sample K01 and K05). The same trend is observed in sample K07, where the fabric is thinner and has a higher grade than sample K07. This finding is consistent with the research by Prakash *et al.* (2013), which suggests that thinner materials wet faster than thicker ones when the same amount of water is applied



### 3.2 Absorption Rate

Absorption rate, as defined by Basuk *et al.* (2018), represents the average moisture absorption ability (%/s) of the fabric's top and bottom surfaces during the pulping process. It measures the speed of liquid moisture absorption on both surfaces of the material during the initial change in water content during the test. By considering the absorption rate of fabrics, researchers and practitioners gain insights into the material's ability to absorb moisture rapidly or gradually. Figure 2 provides the absorption rate values and grades for the top and bottom surfaces of the fabric samples.

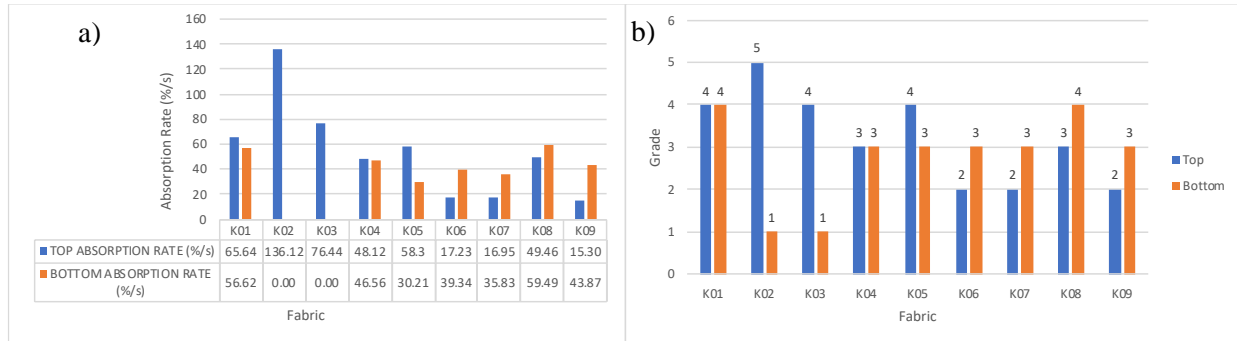


**Figure 2: (a) Absorption rates and (b) absorption rate grades of the fabric samples.**

Sample K02 exhibited the highest absorption rate with value of 136.12 %/s (grade 5) on the top surface. However, it is important to note that this sample is incapable of absorbing moisture from its bottom surface. Similarly, sample K03 also shows no absorption occurring at the bottom surface due to the coating. Absorption occurs only at the top surface, where sample K03 still demonstrates very good performance, not far behind sample K02, with value of 76.44 %/s.

On the other hand, sample K08, with 100% cotton material and twill 3/1 weave, showed the highest bottom surface absorption rate of 59.49 %/s due to cotton's hydrophilic nature. Cotton can efficiently absorb water due to its water-retaining spaces (Matusiak & Kamińska, 2022). Comparatively, K04, also 100% cotton, did not achieve grade 4 absorption rate at the bottom surface, possibly due to fabric construction differences affecting moisture absorption. Likewise, sample K05 (70% cotton, 30% nylon) and K01 (80% cotton, 20% nylon) share hydrophilic materials but exhibited slightly different absorption rates at the bottom surface. Materials such as cotton and nylon are hydrophilic and can absorb moisture but have limited capillary forces to transport the liquid (Matusiak & Kamińska, 2022). In contrast, polyester, a hydrophobic material, absorbs minimal water but exhibits good capillary action. Thus, a higher proportion of hydrophilic cotton in a sample results in a faster moisture absorption rate.

As observed in the results, sample K01, with higher content of cotton, exhibited higher absorption rate as compared to sample K05. This trend can also be seen in samples K02 and K03, where K02, with higher proportion of cotton, shows faster rate of absorption than K03. It is worth noting that sample K09 may be an exception to this trend due to its different construction. According to Kara & Akgun (2018), fabrics made from a blend of cellulosic and polyester have better liquid absorption and transport capabilities. The presence of cotton in fabric compositions enhances the hydrophilic nature of the material, allowing it to absorb and transport moisture more effectively. On the other hand, polyester in the blend contributes to the fabric's capillary action, which aids in the transfer of moisture. This combination of properties results in improved moisture management performance in fabrics with higher cotton content.

### 3.3 Maximum Wetted Radius

Maximum wetted radius refers to the maximum wetted ring radius at the top and bottom surfaces, where the slopes of total water content are greater than  $\tan(15^\circ)$ . This parameter is considered as one of the important factors in assessing moisture management properties (Basuk *et al.*, 2018). The maximum wetted radius values and grade for the top and bottom surfaces for all nine samples are given in Figure 3.

In order to ensure optimal moisture comfort, the inner layer of the sample should have quick liquid transmission properties, while the outer layer should have lower transmission properties to facilitate fast evaporation (Dhanapal & Dhanakodi, 2020). As sweat evaporates from the skin, the body loses heat, which can cause the wearer feel cooler, clammy and sweatier. Therefore, a fabric that has a strong capillary effect can be helpful in removing sweat and avoiding a cool sensation (Karthik *et al.*, 2018b; Dhanapal & Dhanakodi, 2020).

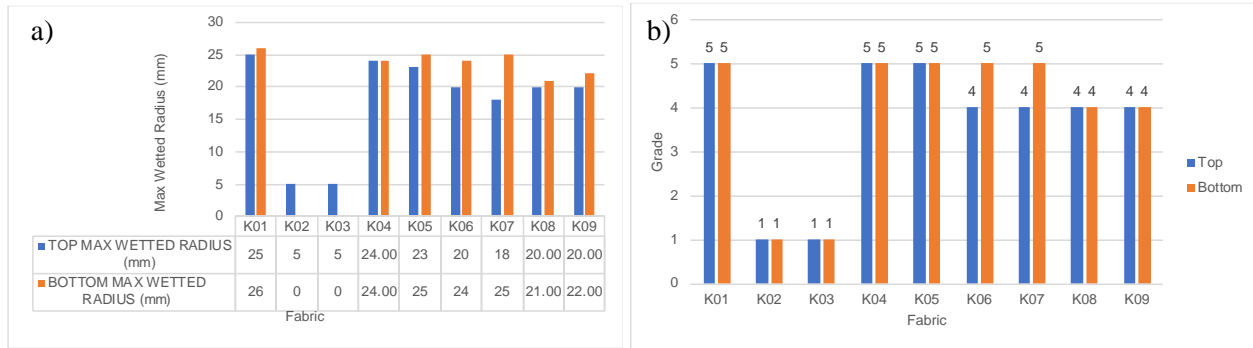


**Figure 3: (a) Maximum wetted radius values and (b) maximum wetted radius grades of the fabric samples.**

Therefore, based on Figure 3, it can be observed that samples that consist of 100% polyester, such as samples K06 and K07, have lower value of maximum wetted radius at the top surface (20 mm and 18 mm respectively) as compared to the bottom surface. Meanwhile, at the bottom surface, these two samples demonstrate a very large maximum wet radius with values of 24 and 25 mm respectively. This behaviour is due to the hydrophobic character of polyester as mentioned before.

In the case of samples K01, K04 and K05, they demonstrated much larger maximum wetted radius at both the top and bottom surfaces as compared to other samples and have been graded with the highest grade of 5 based on the grading scheme. These samples exhibited excellent performance in absorbing the test liquid due to the hydrophilic nature of cotton and nylon materials. Among these samples, sample K01 stood out with the highest maximum wetted radius values among all the samples, with values of 25 and 26 mm for the top and bottom surfaces respectively.

### 3.4 Spreading Speed

Spreading speed can be referred to as the accumulated rate of surface wetting from the centre of the sample where the test solution is dropped to the maximum wetted radius (Selli & Turhan, 2017). This parameter is closely linked to moisture transport, which occurs in parallel to the fabric surface (Venkatesh *et al.*, 2013). A higher spreading speed leads to better liquid spreading on the fabric surface, creating better conditions for the evaporation of sweat (Matusiak & Kamińska, 2022). If the spreading speed value of a sample is over the 4 mm/s, according to MMT rating indices, sweat solution spreads very quickly to the fabric surface. For this study, the spreading speed values and grades for the top and bottom surfaces of the fabric samples are depicted in Figure 4.

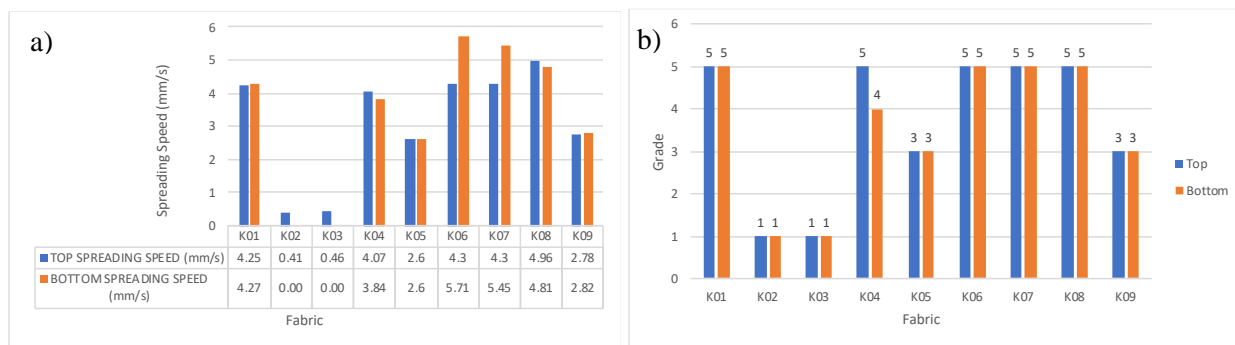


**Figure 4: (a) Spreading speed values and (b) spreading speed grades of the fabric samples.**

In Figure 4 (a), among the nine fabric samples, K08 had the highest top surface spreading speed at 4.96 mm/s and the third highest bottom surface speed at 4.81 mm/s. K06 topped the list with bottom surface speed of 5.71 mm/s, with top surface speed of 4.3 mm/s. Sample K07 also stood out, ranking second in bottom surface spreading speed at 5.45 mm/s, while matching K06's top surface speed of 4.3 mm/s. In contrast, both K02 and K03 had zero spreading speed at the bottom surface, likely due to their coatings. Additionally, K02 had the slowest top surface speed at 0.41 mm/s, while K03 was not far behind at 0.46 mm/s.

Based on these results, K01, K06, K07 and K08 are the top choices for creating favourable conditions for evaporation of perspiration from the skin. K06 and K07 owe their effectiveness to their hydrophobic properties of synthetic fibres, which in this case both of them are made up from 100% polyester. Generally, polyester has fewer bonding sites for water molecules on its surface, allowing it to remain dry and facilitate effective moisture transportation and release (Onofrei *et al.*, 2011). K08 also exhibits high spreading speed, which may be attributed to its fabric construction, which is a twill 3/1 weave and thickness of 0.57 mm. K06 stands out as the fastest-drying fabric based on spreading speed value, consistent with previous research linking moisture spreading capability and drying properties. From the study of Oğlakcıoğlu *et al.* (2018), wetting that occurs on hydrophobic fabric surfaces tend to dry faster as compared to a hydrophilic fabric surfaces. It is worth noting that fabrics K01, K07 and K08 also received grade 5 ratings for both top and bottom surface spreading speed, indicating their excellent performance in facilitating effective perspiration evaporation.

Moreover, fabric samples K06 and K07, which have the highest bottom surface spreading speed values among the fabric samples, are unique in that they are the only fabrics constructed with twill 2/2 weave. Additionally, K06 shares common composition with K07, as both are made of 100% polyester. Furthermore, these two fabrics have relatively lower mass as compared to the other samples (except sample K09), with mass of 174 g/m<sup>2</sup> for K06 and 185 g/m<sup>2</sup> for K07. These findings suggest that weave pattern, fabric mass and composition significantly influence the spreading speed performance, as previously discussed by Selli & Turhan (2017) and Mengüç (2020). Particularly the use of twill 2/2 weave, lower fabric mass and polyester material can lead to a better sweat management properties.

Despite the small difference in material composition, K01 demonstrated spreading speed grade of 5 for both the top and bottom surfaces, while K05 had spreading speed grade of 3 for both surfaces. The difference in fabric performance suggests that factors other than material composition might be influencing spreading speed. One such factor could be the thickness of the fabrics. K01 has thickness of 0.52 mm, while K05 has the highest thickness among the fabrics, measuring at 0.69 mm. This suggests that increase in fabric thickness leads to higher spreading speed, as discussed by Jhanji *et al.* (2017).

### 3.5 Accumulative One-Way Transport Index (AOTI)

AOTI can be defined as the difference between the area of liquid moisture content curves of the top and bottom surfaces of a sample with respect to time (Kan *et al.*, 2018). A fabric with high AOTI offers effective sweat management to the wearer. This is due to the fabric's ability to transport perspiration from the inner side towards the outer side of the fabric, away from the skin, resulting in a dry feeling for the wearer. Positive and high values of AOTI show that moisture can be transferred from the human skin to the outer surface easily and quickly. The higher the index value, the better the material is at transporting liquid (Kan *et al.*, 2018; Matusiak & Kamińska, 2022). The AOTI values and grades of the fabric samples are depicted in Figure 5.

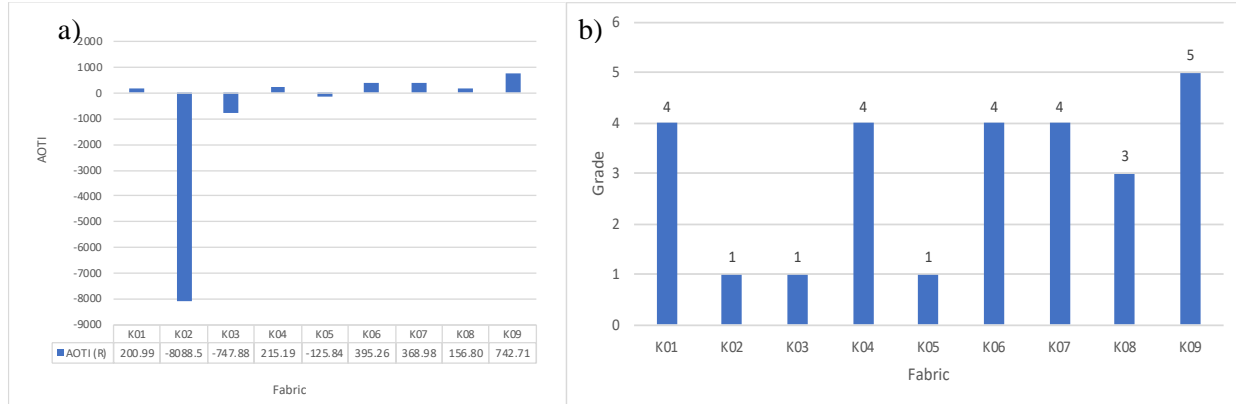


**Figure 5: (a) AOTI values and (b) AOTI grades of the fabric samples.**

According to Figure 5, sample K09 exhibited the highest AOTI with value of 742.71, while sample K06 is the second highest with value of 395.26, closely followed by sample K07 at 368.98. On the other hand, sample K02 had the lowest AOTI value of -8,088.48. The figure also reveals that three samples, namely K02, K03 and K05, had negative AOTI values, which means that sweat can be transferred from the surface next to skin to the opposite surface and spread quickly with large wetted area (Öner *et al.*, 2013). The remaining fabrics, K01, K04, K06 and K08, had positive values, which means that these fabrics can transfer sweat from the skin to the outer surface easily and quickly (Öner *et al.*, 2013).

The results in Figure 5 highlight that sample K09, a blend of 30% cotton and 70% polyester, excels in efficiently transporting liquid moisture from the fabric's inner side away from the skin. This performance is substantiated by its excellent grade 5 AOTI rating. In contrast, despite sharing the same material composition, sample K03's AOTI rating is unimpressive, receiving a poor grade 1. The key differentiator is sample K09's lower mass (114 g/m<sup>2</sup>) and thinner profile (0.26 mm), which are the lowest among the samples. This lightweight and thin design enhances AOTI, facilitating horizontal liquid movement through capillary action. These findings underscore the fabric's exceptional wicking properties, influencing AOTI and moisture management, even compared to samples K02 and K03, which both received poor AOTI grades (grade 1).

Although sample K09 demonstrated the highest AOTI value, it is not the only fabric that received high grade for AOTI. Samples K01, K04, K06 and K07 also received high AOTI rating of grade 4, indicating very good performance in this regard. These findings suggest that these fabrics, along with K09, have the ability for quickly and easily transporting perspiration from the skin towards the environment. Furthermore, samples K06 and K07 (third and second highest AOTI value) are made from 100% polyester and they both have two of the lowest mass after K09 among the samples, with masses of 174 and 185 g/m<sup>2</sup> for samples K06 and K07 respectively. This suggests that weave pattern, mass and composition of the samples,

specifically the use of twill 2/2 weave and polyester material, may play a significant role in influencing AOTI performance, as previously discussed by Selli & Turhan (2017) and Mengüç (2020), with these samples demonstrating favourable sweat management properties. In addition, the hydrophobic nature of polyester allows for effective moisture transportation and release.

In contrast, sample K02, which has the lowest AOTI value, exhibited poor AOTI rating of grade 1, indicating discomfort for the wearer. When sweating, the wearer may experience a wet skin sensation and potential chill effect due to the fabric's inability to effectively transport perspiration from the skin to the environment. Besides that, samples K03 and K05 also had similar AOTI grades of 1, suggesting similar poor performance in sweat management. Notably, fabric samples K02 and K03 are both composed of a blend of cotton and polyester, with K02 consisting of 60% cotton and 40% polyester, and K03 consisting of 30% cotton and 70% polyester. Both samples had negative AOTI score. Fabrics samples with negative or low AOTI values appear to absorb moisture more quickly but dry out more slowly than those with positive values, which indicate a faster transfer of liquid moisture from the skin to the outside surface (Shobanasree, *et al.*, 2023)

### 3.6 Overall Moisture Management Capability (OMMC)

OMMC is an index of the overall capability of a fabric to transport liquid moisture as calculated by combining three measured attributes of performance, which are liquid moisture absorption rate on the bottom surface, accumulative one-way transport index and maximum liquid moisture spreading speed on the bottom surface (Karthik *et al.*, 2018a). A higher value of OMMC indicates better ability of fabrics to manage liquid moisture, as it reflects their capacity to efficiently transport liquid sweat from next to the skin to the outer surface, keeping the skin dry (Namligoz *et al.*, 2010; Matusiak & Kamińska, 2022). Previous studies have also shown that OMMC has correlation with AOTI (Karthik *et al.*, 2018b; Hussain *et al.*, 2019).

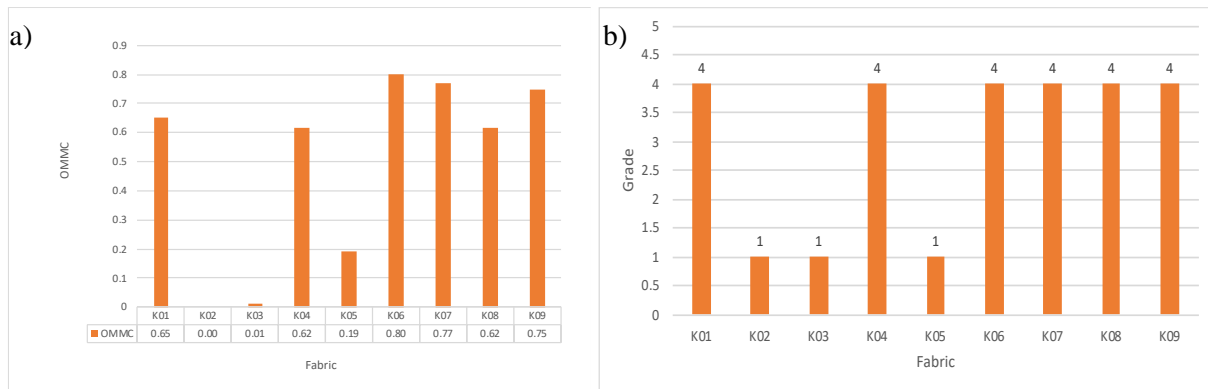


**Figure 6: (a) OMMC values of the fabric samples; (b) OMMC grades of the fabric samples.**

Figure 6 illustrates that sample K06 exhibits the highest OMMC value of 0.80, followed by K07 with value of 0.77, indicating that they have superior moisture management capabilities among the samples. In contrast, sample K02 has the lowest OMMC value of 0, while sample K03 was only slightly higher with value of 0.01, suggesting that they have poor moisture management performance among the samples.

Based on the data, sample K06 appears to be the most comfortable to wear among the samples, as it exhibits the ability to transport liquid moisture quickly and easily from the skin, keeping the skin dry and preventing a chill effect. This is supported by its OMMC grade of 4, which indicates very good performance. It is also

worth mentioning that samples K06 and K07 are used as working uniforms. However, fabric K06 is not the only fabric sample that received a grade of 4 for OMMC. Samples K01, K04, K07, K08 and K09 also achieved the same grade, suggesting that they also have favourable moisture management properties and may provide similar comfort to the wearer.

The finding that samples K06 and K07 exhibited the highest OMMC values among the samples suggest that mass, thickness and composition of the fabrics may play a significant role in influencing OMMC performance, leading to improved sweat management properties, as previously discussed by Selli & Turhan, 2017 and Mengüç (2020).

On the other hand, samples K02 and K03, with OMMC values of 0.00 and 0.01 respectively, demonstrated poor moisture management due to bottom surface coating. Similarly, K05 also scored a grade of 1 for moisture management, mainly because of its high thickness, which resulted in low OMMC value. Notably, both K02 and K03 are cotton-polyester blends, with K02 having 60% cotton and 40% polyester, and K03 comprising 30% cotton and 70% polyester. This suggests that increase in cotton content leads to decrease in OMMC value. This is as the proportion of hydrophilic fiber increases, the number of water absorbing groups also increase, which results in higher moisture regained (Bedeck *et al.*, 2011).

The OMMC grades for all the samples showed a strong correlation with their AOTI grades, which is consistent with findings reported by previous studies (Karthik *et al.*, 2018b; Hussain *et al.*, 2019). This correlation may be attributed to the fact that the OMMC calculation equation takes into account AOTI value.

### 3.7 Fabric Classification

As the moisture management properties have been evaluated, the samples can be classified into several classes according to Table 1 to further understand the type of fabrics that are being used in Malaysian government uniforms. The classification of the fabrics are done by evaluating and combining the performance moisture management properties of the fabric. Based on the fabric types given in Table 1, the classification of the nine fabric samples are recorded in Table 3.

**Table 3: Classification of fabric type.**

<b>Fabric</b>	<b>Type of Fabric</b>
K01	Moisture Management Fabric
K02	Water Proof Fabric
K03	Water Proof Fabric
K04	Moisture Management Fabric
K05	Fast Absorbing and Quick Drying Fabric
K06	Moisture Management Fabric
K07	Moisture Management Fabric
K08	Moisture Management Fabric
K09	Moisture Management Fabric

## 4. CONCLUSION

In summary, sample K06 ranks as the most comfortable fabric for wearers due to its highest OMMC value, indicating efficient moisture transport for a comfortable feel without causing chill or temperature disruptions. Conversely, sample K02 is the least comfortable choice, attributed to its bottom surface coating that can trap sweat on the skin, potentially affecting comfort. However, samples with coating on the outer

layer in a specific condition is needed in order to achieved thermal properties requirements; examples would be uniform used for military operations in different climates. Excluding the coated fabrics, sample K05 is the least comfortable due to its thickness, which can impede moisture wicking, causing discomfort, stickiness and temperature disturbances for the wearer.

Furthermore, each fabric's moisture management is notably influenced by its material composition and yarn type. Fabrics crafted from 100% polyester outperformed those made from 100% cotton, due to polyester's hydrophobic properties that enables efficient liquid transport. On the other hand, in blended yarns, higher cotton content in cotton-nylon blends enhances overall OMMC performance, indicating superior moisture management capabilities in fabrics with increased cotton composition.

Moreover, the fabric's mass per unit area impacts moisture management properties. This study reveals that as mass per unit area decreases, OMMC increases, as seen for samples K06 and K07. K06, with lower mass per unit area, boasts higher OMMC value. Additionally, fabric thickness also affects moisture management, with increased thickness leading to decreased overall performance, as exemplified by sample K05, which has the highest thickness of the samples. This study also explored four construction types, namely 3X3 ripstop, twill 2/2, twill 3/1 and plain, but lacked sufficient data for an in-depth evaluation of this property.

The findings of this study can have some implications for improving the comfort and wearability of government uniforms in Malaysia. By understanding how fabric properties influence moisture management, the study identifies materials that can provide better comfort in different environmental conditions. The results contribute important information for fabric selection in the apparel industry, with the aim of creating more comfortable and functional uniforms.

## REFERENCES

- Basuk, M., Choudhari, M., Maiti, S. & Adivarekar, R.V. (2018). Moisture management properties of textiles and its evaluation. *Curr. Trends Fashion Technol. Textile Eng.*, **3**: 555–611.
- Bedeck, G., Salaün, F., Martinkovska, Z., Devaux, E. & Dupont, D. (2011). Evaluation of thermal and moisture management properties on knitted fabrics and comparison with a physiological model in warm conditions. *Appl. Ergonomics*, **42**: 792–800.
- Chinta, S.K. & Gujar, P.D. (2013). Significance of moisture management for high performance textile fabrics. *Int. J. Innovative Res. Sci. Eng. Tech.*, **2**: 814–819.
- Dhanapal, V.K. & Dhanakodi, R. (2020). Influence of moisture management properties on socks made from recycled polyester, virgin cotton and its blends. *Fibres Text. East. Eur.*, **28**: 76–81.
- Hussain, S., Glombikova, V., Akhtar, N., Mazari, A., Mansoor, T. & Khan, K. (2019). Liquid moisture transportation properties of functional underwears: Part 1. *Autex Res. J.*, **19**: 97–103.
- Jhanji, Y., Gupta, D. & Kothari, V.K. (2017). Moisture management and wicking properties of polyester-cotton plated knits. *Indian J. Fibre Text.*, **42**:183–188.
- Kamalha, E., Zeng, Y., Mwasiagi, J.I. & Kyatuheire, S. (2013). The comfort dimension; a review of perception in clothing. *J. Sens. Stud.*, **28**: 423–444.
- Kan, C. W., Ko, C. M. C., Udon, S., Wanitchottayanont, S., Pangsai, M. & Mongkholrattanasit, R. (2018). Characteristics of fabric-foam-fabric plied material: Water transport capability. *Key. Eng. Mat.*, **777**: 13–16.
- Kara, G. & Akgun, M. (2018). Effect of weft yarn fiber contents on the moisture management performance of denim fabrics woven with different constructional parameters. *Text. App.*, **28**: 151–161.
- Karthik, T., Murugan, R. & Senthilkumar, P. (2018). Analysis of moisture management properties of cotton/milkweed blended rotor yarn fabrics. *Int. J. Cloth. Sci.Tech.*, **30**: 347–362.
- Karthik, T., Senthilkumar, P. & Murugan, R. (2018). Analysis of comfort and moisture management properties of polyester/milkweed blended plated knitted fabrics for active wear applications. *J. Ind.*

- Text.*, **47**: 897–920.
- Karthikeyan, G., Nalakilli, G., Shanmugasundaram, O.L. & Prakash, C. (2017). Moisture management properties of bamboo viscose/tencel single jersey knitted fabrics. *J. Nat. Fibres.*, **14**: 143–152.
- Mahmoudi, M.R. (2010). Blending and composite yarn spinning. In Lawrence, C.A. (Ed.), *Advances in Yarn Spinning Technology*, Woodhead Publishing, UK, pp. 102–118.
- Matusiak, M. & Kamińska, D. (2022). Liquid moisture transport in cotton woven fabrics with different weft yarns. *Materials*, **18**: 6489.
- Mengüç, G.S. (2020). Studies on moisture management properties of various textile products. *Turk. J. Fashion Design Manag.*, **2**: 31–35.
- Messiry, M.E., Ouffy, A.E. & Issa, M. (2015). Microcellulose particles for surface modification to enhance moisture management properties of polyester, and polyester/cotton blend fabrics. *Alex. Eng. J.*, **54**: 127–140.
- Motlogelwa, S. (2018). Comfort and durability in high-performance clothing. In McLoughlin, J. & Sabir, T. (Eds.), *High-Performance Apparel: Materials, Development, and Applications*, Elsevier, Amsterdam, Netherlands, pp. 209–219.
- Namligöz, E.S., Coban, S. & Bahtiyari, M.I. (2010). Comparison of moisture transport properties of the various woven fabrics. *Tekstil ve Konfeksiyon*, **2**: 93–100.
- Oğlacioğlu, N., Çay, A., & Sarı, B. (2018). Moisture management and drying properties of double face knitted fabrics. *Mat. Sci. Eng.*, **459**: 012056.
- Öner, E., Atasagun, H.G., Okur, A., Beden, A.R. & Durur, G. (2013). Evaluation of moisture management properties on knitted fabrics. *J. Text. Inst.*, **104**: 699–707.
- Onofrei, E., Rocha, A.M. & Catarino, A. (2011). The influence of knitted fabrics' structure on the thermal and moisture management properties. *J. Eng. Fibers Fabr.*, **6**: 10–22.
- Osilla, E.V., Marsidi, J.L., Shumway, K.R. & Sharma, S. (2023). Physiology, Temperature Regulation. Available online at: <https://www.ncbi.nlm.nih.gov/books/NBK507838> (Last access dates: 31 January 2024).
- Prakash, C., Ramakrishnan, G. & Koushik, C.V. (2013). Effect of blend proportion on moisture management characteristics of bamboo / cotton knitted fabrics. *J. Text. Inst.*, **104**: 1320-1326.
- Selli, F. & Turhan, Y. (2017). Investigation of air permeability and moisture management properties of the commercial single jersey and rib knitted fabrics. *Tekstil ve Konfeksiyon*, **27**: 27–31.
- Senthilkumar, M., Sampath, M.B. & Ramachandran, T. (2013). Moisture management in an active sportswear: Techniques and Evaluation - A review article. *J. Inst. Eng. (India): E.*, **93**: 61-68.
- Shobanasree, P.C., Prakash, C. & Kumar, M.R. (2023). Moisture management properties of cellulose single jersey fabrics. *Indian J. Fibre Text. Res.*, **48**: 287-294.
- Suganthi, T. & Senthilkumar, P. (2017). Moisture-management properties of bi-layer knitted fabrics for sportswear. *J. Ind. Text.* **47**: 1447-1463
- Umair, M., Hussain, T., Shaker, K., Nawab, Y., Maqsood, M. & Jabbar, M. (2016). Effect of woven fabric structure on the air permeability and moisture management properties. *J. Text. Inst.*, **107**: 596-605.
- Venkatesh, J.V., Gowda, K.N. & Subramaniam, V. (2013). Effect of plasma treatment on the moisture management properties of regenerated bamboo fabric. *Int. J. Sci. Res.*, **10**:1-8
- Vidhya, M., Parveen Banu K., Vasanth Kumar, D., Prakash, C. & Subramaniam, V. (2022). Study on single jersey knitted fabrics made from cotton/ polyester core spun yarns. Part II: Moisture management properties. *Textile Apparel*, **32**: 37- 46.
- Zou, C., Lao, L., Chen, Q., Fan, J. & Shou, D. (2021). Nature-inspired moisture management fabric for unidirectional liquid transport and surface repellence and resistance. *Energ. Buildings* , **248**, 111203.



# A COMPARATIVE STUDY ON INDOOR AIR QUALITY (IAQ) BETWEEN CENTRALISED AND SPLIT UNIT AIR CONDITIONING SYSTEMS IN A NAVAL SHIP

Amirul Faiz Kamaruddin<sup>1,2</sup>, Maryam Zahaba<sup>\*3</sup>, Nur Sarah Fatimah Tamsi<sup>3</sup>, Mohd Khusainy Anua<sup>4</sup>,  
Noor Artika Hassan<sup>5</sup>, Nur Sazwi Nordin<sup>6</sup> & Arman Ariffin<sup>7</sup>

<sup>1</sup>Department of Biotechnology Engineering, Kulliyah of Engineering, International Islamic University Malaysia (IIUM), Malaysia

<sup>2</sup>KD Laksamana Muhammad Amin, Royal Malaysian Navy (RMN) Lumut Naval Base, Malaysia

<sup>3</sup>Department of Chemistry, Kulliyah of Science, International Islamic University Malaysia (IIUM), Malaysia

<sup>4</sup>Inspectorate General Division, Royal Malaysian Navy (RMN) Headquarters, Ministry of Defence, Malaysia

<sup>5</sup>Department of Community Medicine, Kulliyah of Medicine, International Islamic University Malaysia (IIUM), Malaysia

<sup>6</sup>Department of Biomedical Science, Kulliyah of Allied Health Sciences, International Islamic University Malaysia (IIUM), Malaysia

<sup>7</sup>Engineering Department, Royal Malaysian Navy (RMN) Headquarters, Ministry of Defence, Malaysia

\*Email: maryamzahaba@iium.edu.my

## ABSTRACT

*This study determines the compliance of indoor air quality (IAQ) in areas served by different heating ventilation and air conditioning (HVAC) systems in a naval ship, namely centralised and split unit air conditioning systems. A total of nine IAQ parameters, which include physical parameters (temperature, relative humidity (RH) and air movement (AM)), chemical parameters (formaldehyde (CH<sub>2</sub>O), particulate matters (PM<sub>10</sub>), total volatile organic compounds (TVOC) and carbon dioxide (CO<sub>2</sub>)) and biological parameters (total bacterial count (TBC) and total fungal count (TFC) were assessed using calibrated handheld IAQ devices at ten different areas in the ship. The results show that the percentage of compliance is higher in areas served by centralised air conditioning systems as compared to split unit air conditioning systems. The Mann-Whitney test (p-value < 0.05) shows significant difference between the centralised and split unit air conditioning areas for all the IAQ parameters except for temperature. These findings indicate that centralised air conditioning systems, which can introduce fresh air into their served areas contribute to the decrease of concentration of chemical and biological parameters, provided that the units are well maintained.*

**Keywords:** *Indoor air quality (IAQ); naval ship; centralised and split unit air conditioning; indoor air sampling; Mann-Whitney test.*

## 1. INTRODUCTION

Each ship has a unique indoor environment, including indoor air quality (IAQ). IAQ in a ship depends on the design and efficiency of the ship's heating ventilation and air conditioning (HVAC) system to provide proper ventilation and maintain thermal comfort condition throughout the ship (Kharitonova, 2014). Ships are equipped with several types of HVAC systems. Centralised unit air conditioning systems are commonly found on ships, enabling the the mixture of fresh and recirculated air to be supplied to the ship compartments (Mihai & Rusu, 2021). There are also ships installed with split unit air conditioning systems due to limited space and budget. However, a few studies have emphasised on issues of air pollutants accumulation in building settings using this system due to restricted air

circulation (Hussin *et al.*, 2017; Rasli *et al.*, 2021). For marine transportation, there is a lack of studies conducted to investigate the IAQ parameters onboard ships with split unit air conditioning systems.

Previous studies have found that poor IAQ onboard ships due to factors such as pollutants accumulation and poor ventilation can lead to discomfort and health risks to the crew, and can also cause equipment breakdown (Rozzi-ochs, 2006; Zahaba *et al.*, 2022; Tamsi *et al.*, 2023). Furthermore, previous studies have demonstrated that IAQ has significant impact on health status, and leads to acute and chronic health effects (Hazrin *et al.*, 2017). This is due to human exposure to air pollutants from various sources such as personal products, cleaning chemicals and building materials (Tham, 2016). For example, exposure to poor IAQ onboard can lead to sick boat syndrome (SBoS) (Dąbrowiecki *et al.*, 2015; Mohammad Zin *et al.*, 2023). Therefore, IAQ is a critical factor in providing a safe and healthy working environment. Both thermal comfort and ventilation are key factors to ensure good IAQ, providing a productive environment to the crew and significantly boosting their morale while working. These key factors are linked to the HVAC system onboard (Pan *et al.*, 2021).

There have been limited studies specifically addressing IAQ with a focus on HVAC systems, particularly onboard ships. Therefore, this paper attempts to determine IAQ parameter compliance to the available IAQ standard in Malaysia, which is the Industry Code of Practice on Indoor Air Quality 2010 (ICOP IAQ 2010) and compare IAQ parameters between areas served by different HVAC systems, namely centralised and split unit air conditioning systems, in a naval ship.

## **2. METHODOLOGY**

### **2.1 Indoor Air Sampling**

Ten sampling points were selected in a naval auxiliary ship based on the two types of air conditioning systems installed, namely centralised and split unit systems. The sampling points with centralised air conditioning systems were the Bridge, Cabin 1, Cabin 2, Cabin 3, Common Room 1 and Sick Bay, while the sampling points with split unit air conditioning systems were the Electrical Room, Office, Cabin 4 and Common Room 2. All the sampling techniques and procedures were adopted ICOP IAQ 2010. There were nine parameters that were measured using the instruments shown in Table 1. The physical and chemical parameters were taken using direct reading every 5 min for 30 min durations at four timeslots for 8 h of sampling. At the end of the sampling, the 8 h total weight average ( $TWA_8$ ) was calculated for the sampling points. For the biological parameters, the air at the sampling points was sampled on two media agar, tryptic soy agar (TSA) and maltose extract agar (MEA), using active sampling at 100 L/min flow rate in triplicate, following the NIOSH Manual of Analytical Methods (NMAM) 0800 method. The plates then were sent for incubation at the selected condition for microbial growth, as stated in Table 1. Total bacterial count (TBC) and total fungal count (TFC) then were counted in colony forming unit per meter cubic ( $CFU/m^3$ ) after the incubation period.

### **2.2 Data Analysis**

The  $TWA_8$  readings for physical and chemical parameters, and the mean of TBC and TFC were compared to the acceptable limit from ICOP IAQ 2010 to observe the compliance of the parameters measured. Data then was analysed using the Mann-Whitney test for comparison between the median readings of sampling points for the centralised and split unit air conditioning systems.

**Table 1: List of IAQ parameters and instruments.**

Parameters		Instruments	
Physical parameters	Temperature Relative humidity (RH)	TSI VelociCalc 9565	
	Air movement (AM)	Testo 440dP	
Chemical parameters	Formaldehyde (CH <sub>2</sub> O)	Kanomax Gas Monitor 2700 Series with Aeroqual Sensor Head	
	Respirable particulates (PM <sub>10</sub> )	Kanomax Digital Dust Monitor Model 3443	
	Total volatile organic compounds (TVOC)	RAE Systems ppbRAE 3000	
	Carbon dioxide (CO <sub>2</sub> )	TSI VelociCalc 9565	
Biological parameters	Total bacterial count (TBC)	TSA agar (37°C, 24 h)	PBI International SAS Super IAQ
	Total fungal count (TFC)	MEA agar (30°C, 5 days)	

### 3. RESULTS AND DISCUSSION

#### 3.1 Compliance of IAQ Parameters

The TWA<sub>8</sub> of IAQ parameters readings were calculated and shown in Table 2. The data was compared to the ICOP IAQ 2010 acceptable limits as the reference standard to observe the compliance of the IAQ parameters readings in the ten sampling points with different types of air conditioning systems. Based on the table, the IAQ parameter readings at all the sampling points were within the acceptable limits for PM<sub>10</sub> and TFC. However, for the other parameters, there was at least one sampling point recorded that exceeded the limit of ICOP IAQ 2010.

In this study, regardless of the type of air conditioning system used, low air temperature was observed at almost all the sampling points, except for Common Room 2 and Bridge. Only Common Room 2 recorded temperature within the acceptable limit of ICOP IAQ 2010. Meanwhile, the exceeded limit of temperature recorded in the Bridge was possibly due to heat radiation from solar passing through the window. The study by Mohammad Zin *et al.* (2023) also found similar results for the temperature at a bridge. In this study, the temperature of the sampling points could be adjusted and set using thermostats for both types of air conditioning systems. Therefore, in this study, the lower temperature selection suits the thermal comfort of the crew onboard.

**Table 2: TWA<sub>s</sub> of IAQ parameters readings at the sampling points.**

Air Conditioning System	Sampling Point	Temp (°C)	RH (%)	AM (m/s)	CH <sub>2</sub> O (ppm)	PM <sub>10</sub> (mg/m <sup>3</sup> )	TVOC (ppm)	CO <sub>2</sub> (ppm)	TBC (CFU/m <sup>3</sup> )	TFC (CFU/m <sup>3</sup> )
Centralised System	Bridge	27.6	64.1	0.13	0.10	0.006	0.33	782	100	130
	Cabin 1	22.1	56.6	0.15	0.07	0.003	0.32	724	157	33
	Cabin 2	20.3	63.1	0.09	0.09	0.003	0.33	673	45	50
	Cabin 3	21.5	60.6	0.12	0.06	0.004	0.27	869	173	40
	Common Room 1	22.8	55.3	0.11	0.09	0.003	0.34	662	107	60
	Sick Bay	22.1	51.5	0.06	0.22	0.002	0.44	616	40	67
Split Unit System	Electrical Room	22.2	51.8	0.27	0.56	0.034	3.60	2184	510	557
	Office	22.4	59.0	0.27	0.17	0.004	0.55	945	303	927
	Cabin 4	21.8	76.7	0.15	0.25	0.004	1.44	976	670	380
	Common Room 2	25.9	65.8	0.22	0.95	0.003	4.64	1538	60	163
Reference Standard: ICOP IAQ 2010	23.0 – 26.0	40.0 – 70.0	0.15 – 0.50	0.10	0.15	3	C1000	500	1000	

\*The values highlighted in red colour are out of the acceptable limits specified by ICOP IAQ 2010.

For the RH parameter, only Cabin 4 recorded an exceeded reading of RH among all the sampling points. The high RH was suspected due to the higher occupancy of the accommodation area, with an adjacent bathroom near the sampling point.

This study also found that the sampling points with centralised air conditioning systems recorded lower AM readings as compared to the ones with split unit systems. Kwong *et al.* (2018) also reported similar findings for AM readings and justified that the medium fan speed used in split unit air conditioning systems provide higher AM in the area as compared to centralised systems. In addition, low AM in the area served by the centralised system could be due to pneumatic friction and local resistance of the air as it moves along the ducting used in the system (Yaropud, 2021).

The compliance of temperature, RH and AM parameters is important in providing thermal comfort to the ship crew and for them to work in high productivity and comfortable conditions. As mentioned by Carter & Japsen (2014), Krystosik-Gromadzińska (2017) and Sagaro *et al.* (2021), ship crew are commonly exposed to thermal discomfort due to machinery, working nature and solar radiation.

For the chemical parameters, this study found a trend of higher and exceeded readings of CH<sub>2</sub>O, TVOC and CO<sub>2</sub> concentrations recorded at the sampling points with split unit air conditioning systems. Chemical concentrations, such as CH<sub>2</sub>O, onboard are derived from off-gassing emissions from the furniture, especially wooden products, carpeting and paint (Kim & Lee, 2010; Gabriel *et al.*, 2020; Avram *et al.*, 2020). According to Wagdi *et al.* (2018) and Kim *et al.* (2019), the concentration of CH<sub>2</sub>O increases with higher temperature and RH. This supports the finding of high CH<sub>2</sub>O concentration along with high temperature and RH in the Bridge.

The source of TVOC in the ship could be from diesel exhaust, air freshener, paint and cleaning products (Cretescu *et al.*, 2019; Kim *et al.*, 2019; Landwehr *et al.*, 2020). According to Tian *et al.*, (2018), TVOC concentrations might consist of harmful volatile organic compounds such as benzene and toluene, which are likely found in diesel emissions.

CO<sub>2</sub> concentration reflects the occupancy of the area since the main source of CO<sub>2</sub> in an indoor area is human exhalation. The most prominent gaseous effluent from humans is CO<sub>2</sub> produced metabolically and emitted at rates of tens of grams per hour (Tang *et al.*, 2016). Therefore, CO<sub>2</sub> concentration could be used to indicate the ventilation performance of an area.

Similar to the chemical parameters, the split unit air conditioning system also recorded exceeded concentrations of biological parameter TBC for the Electrical Room and Cabin 4. According to Gebrihiwot (2020), TBC in an indoor area is attributed to human factors and hygiene practices. From the findings, high CO<sub>2</sub> concentration in the Electrical Room and Cabin 4 supported the result of high TBC that was recorded.

Overall, this study found that the sampling points with split unit air conditioning systems were reported to have more noncompliance of IAQ parameters as compared to the sampling points with centralised air conditioning systems. Table 3 shows the percentage of IAQ parameter compliance to ICOP IAQ 2010 for both types of air conditioning systems.

**Table 3: Percentage of overall compliance readings for each air conditioning system.**

Type of Air Conditioning	Total Sampling Points	Number of Overall Compliance Readings	Number of Overall Non-Compliance Reading	Percentage of Compliance (%)
Centralised Unit System	6	41	13	75.9
Split Unit System	4	22	14	61.1

From the table, the centralised air conditioning system had more percentage of overall compliance reading for IAQ parameters (75.9%) as compared to the split unit system (61.1%). This indicates that centralised air conditioning systems could provide better IAQ as compared to split unit air conditioning systems. According to Gabriel *et al.* (2020), a centralised air conditioning system allows for the introduction of fresh air to the served area, thus providing better dilution of air pollutants in the area. On the other hand, the area served by the split unit air conditioning system does not have the introduction of fresh air as the system only allows for the recirculation of air inside the area. This causes

the air pollutants emitted from indoor sources and activities to accumulate in the area. This explains the higher and exceeded IAQ parameter readings of CH<sub>2</sub>O, TVOC, CO<sub>2</sub>, and TBC in most of the sampling points served by the split unit in this study. The accumulation of air pollutants in an area leads to human discomfort and health symptoms such as eye irritation, skin rashes and nausea to the occupants.

### 3.2 Statistical Analysis

In order to observe the influence of different types of air conditioning systems used on the IAQ onboard the ship, this study also ran a statistical analysis for the IAQ parameters in the areas served by the centralised and split unit air conditioning systems. Table 4 shows the results of the Mann-Whitney test for all the IAQ parameters monitored in this study.

**Table 4: The median of centralised and split unit air conditioning areas.**

Parameter	Median (IQR)		Z statistics	p-value*
	Centralised unit air conditioning areas	Split unit air conditioning areas		
Temperature (°C)	22.0 (2.7)	23.0 (3.0)	-1.644	0.100
RH (%)	58.3 (8.4)	62.5 (15.8)	-3.572	< 0.05
AM (m/s)	0.11 (0.09)	0.16 (0.16)	-5.028	< 0.05
CO <sub>2</sub> (ppm)	618 (62)	954 (1044)	-12.542	< 0.05
CH <sub>2</sub> O (ppm)	0.08 (0.07)	0.34 (0.33)	-10.341	< 0.05
TVOC (ppm)	0.28 (0.18)	2.57 (2.95)	-12.693	< 0.05
PM <sub>10</sub> (mg/m <sup>3</sup> )	0.003 (0.002)	0.004 (0.009)	-4.309	< 0.05
TBC (CFU/m <sup>3</sup> )	110 (65)	315 (460)	-2.912	0.003
TFC (CFU/m <sup>3</sup> )	70 (60)	345 (688)	-4.580	< 0.05

\*Mann-Whitney test  $p$ -value < 0.05 shows significant difference between the centralised and split unit air conditioning areas.

From the analysis, this study found that there were significant differences ( $p$ -value < 0.05) for all the IAQ parameters, except for temperature. This shows that there was a notable influence in installing the two types of air conditioning systems. Therefore, it is important to decide on the best types of air conditioning unit system to be installed to provide better IAQ for the occupants. This study found that the installation of split unit air conditioning systems resulted in significantly higher air chemical concentrations and recorded more noncompliant IAQ parameters. Although centralised air conditioning systems are recommended based on the findings, good hygiene practices and maintenance of the units need to be highlighted as poor IAQ is often associated with the centralised system, especially in crowded areas, as well as poor maintenance and condition of the units (WHO, 2011; Nasir *et al.*, 2016; ILO,

2018). The maintenance of centralised air conditioning systems is often neglected due to system complexity, lack of awareness and budgeting. Zainal *et al.* (2019) reported that a poorly maintained centralised air conditioning system caused significant increase in eye and upper respiratory symptoms among building occupants. The same study also reported higher prevalence of sick building syndrome symptoms in areas served by centralised systems as compared to those with split unit systems, due to factors of poor maintenance and ventilation. Focussing on the ship, the selection of the type of air conditioning systems to be installed in the ship compartments and cabins is crucial considering the ship's nature, crew's activities and environmental factors. Regardless of the type of air conditioning system, good maintenance and hygiene practice is always important to prevent cases of SBoS symptoms and ship-acquired diseases, which commonly occurs among crew members, especially in crowded areas.

#### 4. CONCLUSION

In conclusion, this paper sheds light on the effects of different HVAC systems, namely centralised and split unit air conditioning systems, within the context of naval ships. It is observed that areas served by centralised air conditioning systems exhibit higher percentage of compliance with ICOP IAQ 2010 as compared to those served by split unit air conditioning systems. This is as the centralised systems have better capability to introduce fresh air into the serviced areas, thus effectively reducing the concentration of chemical and biological air pollutants. Furthermore, the application of split unit air conditioning systems in naval ships is deemed inadvisable due to the air pollutants accumulation and inadequate ventilation. Nevertheless, it is understandable that some ships use this system due to space limitation and ease of maintenance. Therefore, good practices need to be suggested to prevent pollutants from being accumulated inside the compartments.

This study also underscores the significance of proper HVAC system maintenance for ensuring good IAQ. Even though the centralised unit air conditioning provided better IAQ as in the findings, poorly maintained unit systems can give poor ventilation, which would lower the IAQ at the area. It is emphasised that addressing IAQ issues requires a holistic approach, integrating human factors such as awareness of good IAQ management practices. Overall, these insights contribute valuable considerations for optimising HVAC systems in naval settings, aiming to enhance both operational efficiency and the well-being of onboard personnel.

#### 5. REFERENCES

- Carro, G., Jacobs, W., Storme, P., Cabal, A., Demeyer, S., & Schalm, O. (2020). A new approach to make indoor air quality in the accommodation of ships understandable and actionable for seafaring staff. *Proc. 8th Int. Conf. Maritime Transport: Tech., Innov. Research (Maritime Transport 2020)*, Universitat Politècnica de Catalunya.
- Carter, T. & Jepsen, J.R. (2014). Exposures and health effects at sea: report on the NIVA course: maritime occupational medicine, exposures and health effects at Sea Elsinore, Denmark. *Int. Marit Health*. **65**: 114-121.
- Cretescu, I., Isopescu, D.N., Lutic, D. & Soreanu, G. (2019). Indoor air pollutants and the future perspectives for living space design. In Korhan, O (Ed.), *Indoor Environment and Health*. InTechOpen, London, UK, pp. 85-100.
- Dąbrowiecki, Z., Dąbrowiecka, M., Olszański, R., Siermontowski, P. & Józwiak, D. (2015). Sick boat syndrome. *Pol. Hyp. Res.*, **53**: 81-92.
- DOSH. (2010). *Industry Code of Practice on Indoor Air Quality*. Available online at: <https://www.dosh.gov.my/index.php/legislation/codes-of-practice/chemical-management/594-02-industry-code-of-practice-on-indoor-air-quality-2010>
- Gabriel, M.F., Felgueiras, F., Fernandes, M., Ribeiro, C., Ramos, E., Mourão, Z., & de Oliveira Fernandes, E. (2020). Assessment of indoor air conditions in households of Portuguese families

- with newborn children. Implementation of the HEALS IAQ checklist. *Environ. Res.*, **182**: 108966.
- Gebrehiwot, M. (2022). Quality of indoor air environment and hygienic practices are potential vehicles for bacterial contamination in University cafeteria: case study from Haramaya University, Ethiopia. *Int. J. Environ. Health Res.*, **32**: 511-521.
- Hazrin, A.H., Maryam, Z., Hizri, A., Norhidayah, A., Samsuddin, N. & Mohd Shukri, M.A. (2017). Occupancy implications on indoor air quality (IAQ) in selected primary school classrooms around Kuantan, Pahang. *Malaysian J. Public Health Med.*, **17**: 94–105.
- Hussin, M., Ismail, M.R., & Ahmad, M.S. (2017). Air-conditioned university laboratories: Comparing CO<sub>2</sub> measurement for centralized and split unit systems. *J. King Saud Univ. Eng. Sci.*, **29**:191–201.
- ILO (International Labour Organisation) (2018). *Maritime Labour Convention 2006 (Amended 2018)*. International Labour Organisation (ILO), Geneva, Switzerland.
- Kharitonova, T. (2014). *Indoor Climate in Ships*. Bachelor Thesis, Mikkeli University of Applied Sciences, Finland.
- Kim, H.H., Park, G.Y. & Lee, J. H. (2019). Concentrations of particulate matter, carbon dioxide, VOCs and risk assessment inside Korean taxis and ships. *Environ. Sci. Pollut. Res.*, **26**: 9619-9631.
- Kwong, Q.J., Abdullah, J., Tan, S.C., Thio, T.H.G. & Yeaw, W.S. (2019). A field study of indoor air quality and occupant perception in experimental laboratories and workshops. *Manag. Environ. Qual.*, **30**: 467-482.
- Landwehr, K.R., Larcombe, A.N., Reid, A. & Mullins, B.J. (2021). Critical review of diesel exhaust exposure health impact research relevant to occupational settings: are we controlling the wrong pollutants?. *Expos. Health.*, **13**: 141-171.
- Mihai, V. & Rusu, L. (2021). An overview of the ship ventilation systems and measures to avoid the spread of diseases. *Inventions*, **6**: 55.
- Mohammad Zin, N.A.T., Kamaruddin, A.F., Tamsi, N.S.F., Zamri, M.F., Hassan, N.A., Ariffin, A. & Zahaba, M. (2023). Indoor air quality (IAQ) onboard a naval ship: a comparative study between areas. *Defence S&T Tech. Bull.*, **16**: 64–72.
- Nada, S.A. & Said, M.A. (2017). Performance and energy consumptions of split type air conditioning units for different arrangements of outdoor units in confined building shafts. *Appl. Therm. Eng.*, **123**: 874–890.
- Nasir, Z.A., Campos, L.C., Christie, N. & Colbeck, I. (2016). Airborne biological hazards and urban transport infrastructure: current challenges and future directions. *Environ. Sci. Pollut. Res.*, **23**: 15757-15766.
- Pan, Y., Du, C., Fu, Z. & Fu, M. (2021). Re-thinking of engineering operation solutions to HVAC systems under the emerging COVID-19 pandemic. *J. Build. Eng.*, **43**: 102889
- Rozzi-ochs, J. A. (2006). *Shipboard Ventilation Systems and Design Standards on Board*. Doctoral Dissertation, University of Florida.
- Sagaro, G. G., Dicanio, M., Battineni, G., Samad, M. A., & Amenta, F. (2021). Incidence of occupational injuries and diseases among seafarers: A descriptive epidemiological study based on contacts from onboard ships to the Italian Telemedical Maritime Assistance Service in Rome, Italy. *BMJ Open*, **11**: e044633.
- Tamsi, N.S.F., Zahaba, M., Kamaruddin, A.F., Mohammad Naufal, M.S., Norhidayah, A. & Ariffin, A. (2023). Concentration of indoor air chemical parameters at different ship conditions and engine sequences. *ASM Sc. J.*, **18**: 1015.
- Tang, X., Misztal, P.K., Nazaroff, W.W. & Goldstein, A.H. (2016). Volatile organic compound emissions from humans indoors. *Environ. Sci. Tech.*, **50**: 12686-12694.
- Tham, K.W. (2016). Indoor air quality and its effects on humans—A review of challenges and developments in the last 30 years. *Energy Build.*, **130**: 637–650.
- Tian, J., Tan, J., Hu, N., Liu, T., Wang, Y., Zhong, H., Cheng, J. & Zhang, X. (2018). Characteristics analysis for total volatile organic compounds emissions of methanol-diesel fuel. *J. Energy Inst.*, **91**: 527-533,
- Wagdi, D., Tarabieh, K. & Zeid, M.N.A. (2018). Indoor air quality index for preoccupancy assessment. *Air Qual. Atmos. Health.*, **11**: 445-458.



- WHO (World Health Organization) (2011). *Handbook for Inspection of Ships and Issuance of Ship Sanitation Certificates* (No. WHO/HSE/IHR/LYO/2011.3). World Health Organization (WHO), Geneva, Switzerland.
- Xue, H., Chou, S.K. & Zhong, X.Q. (2004). Thermal environment in a confined space of high-rise building with split air conditioning system. *Build Environ.*, **39**: 817–823.
- Yahaya, R., Arif, H.M., & Kamel, S.N.M. (2012). Preliminary study on indoor air quality (IAQ) on a Royal Malaysian Navy (RMN) ship. *Defence S&T Tech. Bull.*, **5**: 11-20.
- Yaropud, V. (2021). Analytical study of the automatic ventilation system for the intake of polluted air from the pigsty. *Sci. Horiz.*, **24**: 19-27.
- Yau, Y.H. & Pean, H.L. (2014). The performance study of a split type air conditioning system in the tropics, as affected by weather. *Energy Build.*, **72**: 1–7.
- Zahaba, M., Tamsi, N.S.F., Engliman, S., Kamaruddin, A.F., Hassan, N.A. & Ariffin, A. (2022). Indoor air quality (IAQ) in a naval ship after refit program: a time variation analysis. *IOP Conf. Ser.: Earth Environ. Sci.*, **1013**: 012004.
- Zhou, X., Yan, D. & Shi, X. (2017). Comparative research on different air conditioning systems for residential buildings. *Front. Archit. Res.*, **6**: 42–52.

# FUSION DATASETS FOR ULTRASONIC WELD DEFECT CLASSIFICATION WITH TRANSFER LEARNING IN NEURAL NETWORKS

Suhairy Sani<sup>1,2</sup>, Mohamad Hanif Md Saad<sup>1</sup>, Norsalim Muhammad<sup>3</sup>, Siti Fatahiyah Mohamad<sup>4</sup> & Megat Harun Al Rashid Megat Ahmad<sup>2</sup>

<sup>1</sup>Department of Mechanical and Materials Engineering, Faculty of Engineering and Built Environment, Universiti Kebangsaan Malaysia (UKM), Malaysia

<sup>2</sup>Industrial Technology Division, Malaysian Nuclear Agency, Malaysia

<sup>3</sup>Faculty of Mechanical Engineering, Universiti Teknikal Malaysia Melaka (UTeM), Malaysia

<sup>4</sup>Radiation Processing Technology Division, Malaysian Nuclear Agency, Malaysia

\*Email: suhairy@nm.gov.my

## ABSTRACT

*Fusion datasets from ultrasonic signals for welds have potential as an alternative method for defect classification with neural network algorithms. This paper evaluates the effectiveness of fusion datasets in classifying various types of weld defects. Artificial neural networks (ANN) are used to establish features data, and convolutional neural networks (CNN) are used to predict image features. The study consists of three stages: (i) model evaluation, (ii) defect classification, and (iii) transfer learning. The analysis begins with model evaluation based on the accuracy and precision of the chosen classifier. Then, the potential datasets are used: single datasets (sA and iA), and fusion datasets (sVer, sHor, iOl and iCont) for both ANN and CNN respectively. Finally, a comparative study is conducted using precision and recall to obtain the model predictions. The effectiveness of the data fusion is evaluated using accuracy, precision and recall during the transfer learning process. Each model shows a unique output, whereby DNN5 (sHor dataset) and VGG19 (iCont dataset) show the highest accuracy for ANN and CNN respectively. For all the tested models, precision and recall demonstrate consistent data across multiple defect types. From this work, the data is significant for application in ultrasonic testing (UT), specifically in weld defect classification.*

**Keywords:** *Weld defect; ultrasonic testing (UT); data fusion; neural networks; transfer learning.*

## 1. INTRODUCTION

Various techniques have been developed and utilised in non-destructive testing (NDT) to ensure the quality and reliability of welded structures (Babu *et al.*, 2016; Opacic *et al.*, 2022). Among these techniques, ultrasonic testing (UT) has been widely adopted in neural network for the detection and characterisation of weld defects due to its provision of valuable information on weld joints (Esther Florence *et al.*, 2018; Provencal & Laperrière, 2021). However, precise classification of weld defects from the signals remains a complex task due to the small differences in data patterns for different types of defects. Additionally, the interpretation of the ultrasonic signals is subjective and heavily relies on the experience and expertise of the operators. This can lead to inconsistencies and variations in defect classification, thereby hindering the effectiveness of quality control processes (Murta *et al.*, 2018; IAEA, 2018; Niccolai *et al.*, 2021).

Previous researches have focused on addressing the issue of signal defect analysis and classification using various algorithms. One of the primary goals in defect analysis is to improve the accuracy of neural network models, and the significance of utilising large datasets has been emphasised (Dave & Dutta, 2014). Experiments using acoustic emission (AE) techniques have been conducted to investigate defect detection and identification in welds, as well as their relationship with propagating distance

(Droubi *et al.*, 2017). Researchers have proposed data fusion methodologies to enhance defect characterisation in ultrasonic inspection, particularly focusing on multiple-view images obtained from the total focusing method (TFM) (Bevan *et al.*, 2020). Another data fusion method has been developed by combining artificial neural networks (ANN) and machine learning techniques to improve defect detectability (Cormerais *et al.*, 2021). In order to achieve efficient flaw detection, a segmented analysis approach utilising time-of-flight diffraction (TOFD) ultrasound signals has been suggested (Silva *et al.*, 2020). In the domain of phased array ultrasonic testing (PAUT), a convolutional neural network (CNN)-based approach has been introduced to streamline the process and enhance the efficiency of weld defect recognition (Jiang *et al.*, 2021). Additionally, Inoue (2018) proposed a data augmentation technique known as sample pairing to address the challenge of limited training sample sizes in image classification tasks. Augmentation methods have been employed to improve the datasets, and the accuracy of the models has been evaluated by comparing them with other pretrained deep convolutional neural network models (Ajmi *et al.*, 2020).

Neural networks, including deep learning models such as ANN and CNN, have been extensively studied by previous researchers in the context of pattern recognition and classification tasks. These studies provide evidence for the effectiveness of both ANNs and CNNs in analysing, classifying and assessing weld defects (Sudhamayee, 2019; Amiri *et al.*, 2020; Jiang *et al.*, 2021). However, there is still a research gap when it comes to investigating the effectiveness of data fusion techniques in weld defect classification. Further research and the development of novel approaches are needed to improve the accuracy and reliability of classification methods.

This study aims to address the effectiveness of features fusion datasets that are extracted from ultrasonic signals to achieve better results in weld defect classifications. The study specifically focuses on evaluating features fusion for weld defect identification using ANN and CNN models. It considers five types of weld defects: centre crack (CCr), slag inclusion (SI), lack of fusion (LOF), cluster porosity (Po) and lack of penetration (LOP), as well as intact conditions (N - no defects) as the baseline reference. The study comprises of three main elements: exploring the effectiveness of fusion datasets for UT, evaluating the performance of ANN and CNN models in weld defect classification, and comparing the transfer learning process of the fusion datasets.

## 2. METHODOLOGY

### 2.1 Fusion Datasets

The classification of fusion datasets weld defects from the features-based approach using ANN and the image-based approach using CNN is illustrated in Figure 1. The extracted features obtained from full-wave pulse echo (FWPE) signals from a previous study (Sani *et al.*, 2022) were used to construct three categories of datasets for ANN:

- a) *sA*: Datasets collected only from side A (*sA*) with eight features. The training dataset comprises of 4,200 data elements (700 rows of data per class with six types of defects), and the test dataset contains 1,800 data elements (300 rows of data per class with six types of defects).
- b) *sVer*: Datasets fused vertically from side A (*sA*) and side B (*sB*), resulting in eight features. The training dataset consists of 8,400 data elements (1,400 rows of data per class from each side with six types of defects), and the test dataset contains 3,600 data elements (600 rows of data per class from each side with six types of defects).
- c) *sHor*: Datasets fused horizontally from side A (*sA*) and side B (*sB*), resulting in 16 features. The training dataset comprises 4,200 data elements (700 rows of data per class with six types of defects), and the test dataset contains 1,800 data elements (300 rows of data per class with six types of defects).

For CNN, the image was recorded at maximum peak using lateral movement scanning on the both sides of the weld. Image frames were set in a scanning range from half skip distance (HSD) to full skip

distance (FSD) plus half weld cap at 100% of full screen height (FSH), while observing defect echoes. The image datasets used for the CNN model consist of 560 train and 240 test images from different sets of specimens. Datasets from both sides of the image were fused in different data processing approaches and three categories of image datasets were used for CNN:

- iA*: Image dataset from side A (*iA*) only.
- iOl*: Image datasets fused in overlap from side A (*iA*) and side B (*iB*).
- iCont*: Image datasets fused continuously from side A (*iA*) and side B (*iB*).

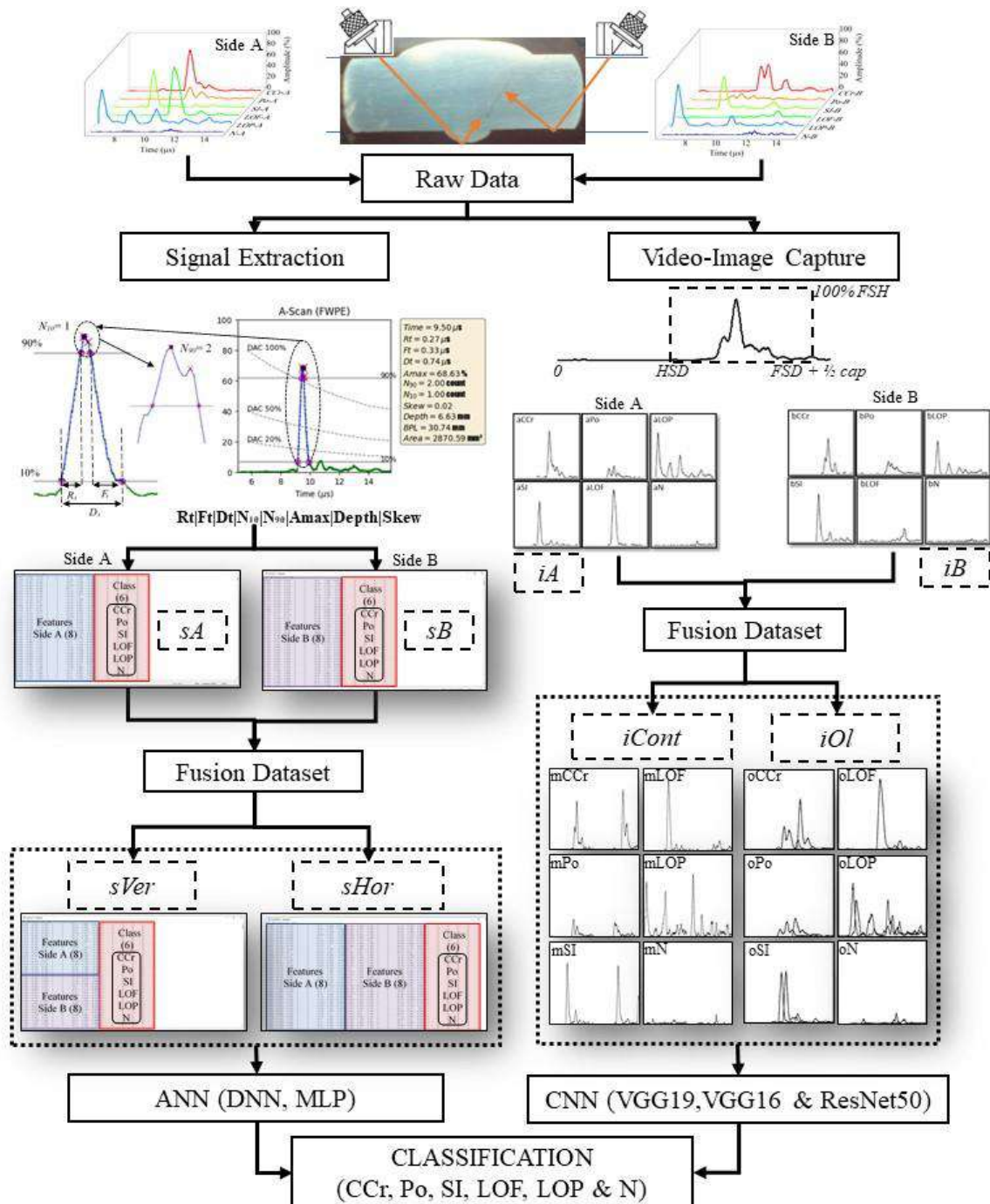


Figure 1: Flowchart of fusion datasets for ANN and CNN.

## 2.2 Neural Network (NN) Models Architectures

In the ANN model, different architectures were employed using multi-layer perceptron (MLP) (three layers), five-layer deep neural network (DNN) (DNN5) and seven-layer DNN (DNN7) for experimentation and performance comparison in weld defect classification. For DNN models, a sequential model was implemented using the TensorFlow framework with the Keras application programming interface (API). These models consist of an input layer with 64 units and rectified linear unit (ReLU) activation, while the output layer had six units for multi-class classification using softmax activation. The model was compiled with the Adam optimiser, category loss function and an accuracy metric for training. The training data was fitted to the model for 100 epochs with a batch size of 32 to improve both the speed and effectiveness. The DNN model performance was evaluated using a validation split of 0.3 (30% test data, 70% training data). The trained model was saved to a file (h5 format) and a confusion matrix was computed to compare predicted labels with true labels using the argmax function. For the MLP model, scikit-learn modules were imported to build the model. A MLP classifier object was created with specific hyperparameters, including learning rate, batch size and hidden layer size. The model was trained on the training data using the fit function and saved to a file (sav format) using the Pickle module.

In the CNN models, VGG-16, VGG-19 and ResNet-50 architectures were utilised to extract features from 128x128-pixel images with three color channels. Pre-trained weights from the ImageNet datasets were used to extract 16 layers for VGG-16, 19 layers for VGG-19 and 50 layers for ResNet-50. Then, fully connected (FC) layers with locally connected layers were used for further processing of these features. The FC was implemented as a sequential model in Keras, with input layers of (4, 4, 512) for VGG models and (4, 4, 2084) for ResNet-50. After the locally connected layers, the final classification was added using softmax activation to assign probabilities to the classes. The model employed categorical and Adam optimiser parameters during training while evaluating the data in batches. By leveraging pre-trained architectures, feature extraction and employing an FC, the CNN models effectively capture image information and learn representations for classification.

The saved models were loaded from the file, and its accuracy and loss values were recorded, along with a metrics report containing precision, recall and F1-score for each class to evaluate and analyse the performance of the weld defect classification.

## 2.3 Data Analysis

Figure 2 shows the evaluation results, including a confusion matrix, classification report and transfer learning plot. The confusion matrix compares predicted and real labels to offer an overview of the performance of the model. In order to measure the accuracy of the model, the classification report presents detailed metrics such as precision, recall and F1 score for each class. Transfer learning plots illustrate the progress of the model during training and validation, showing its learning trend. These evaluation metrics provide information on the model performance in classifying weld defects and normal conditions, guiding decision-making and potential improvements.

The following performance metrics were used to evaluate a classifier (Géron, 2017):

$$\text{Precision (specificity)} = \frac{TP}{TP + FP} \quad (1)$$

$$\text{Recall (sensitivity)} = \frac{TP}{TP + FN} \quad (2)$$

Precision and recall are used to measure how well the classifiers perform on an imbalance dataset. The balance between the precision (P) and the recall (R) scores is described by F1-score as:

$$F1 - score = \frac{2 \times Precision \times Recall}{Precision + Recall} \quad (3)$$

On the other hand, the accuracy metric is given by:

$$Accuracy = \frac{TP + TN}{TP + TN + FP + FN} \quad (4)$$

which represents the percentage of correctly classified activities, where TP is true positive, TN is true negative, FP is false positive and FN is false negative.

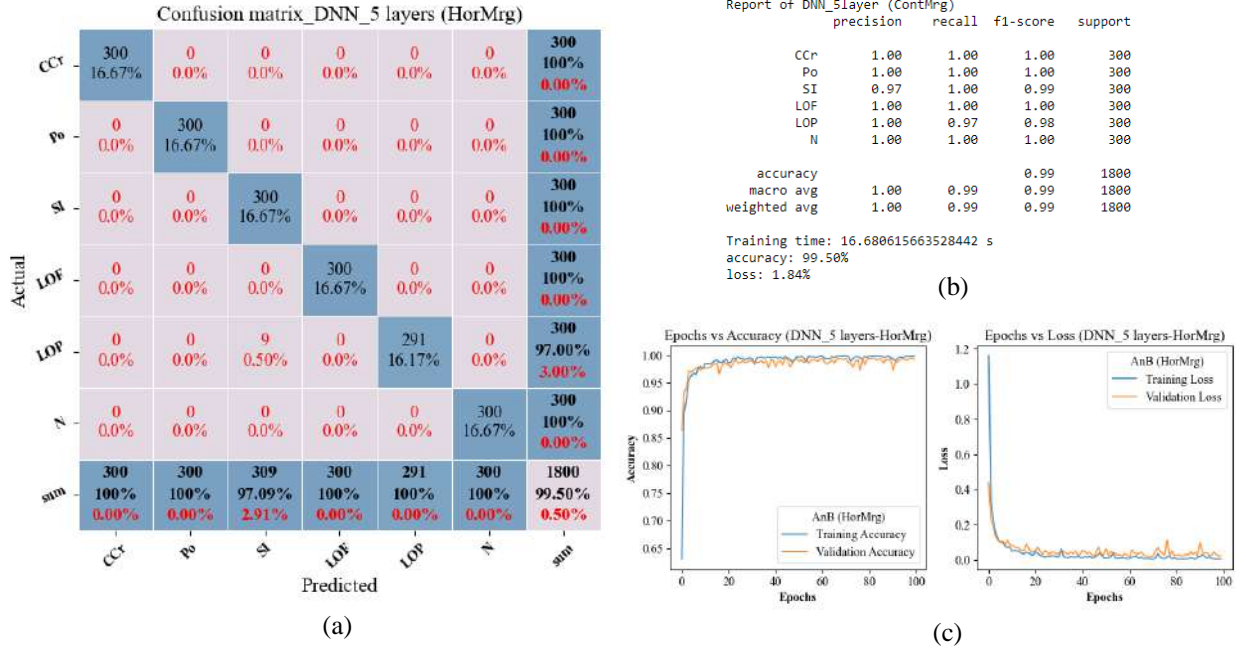


Figure 2: (a) Confusion matrix, (b) classification report, and (c) transfer learning plot.

### 3. RESULTS & DISCUSSION

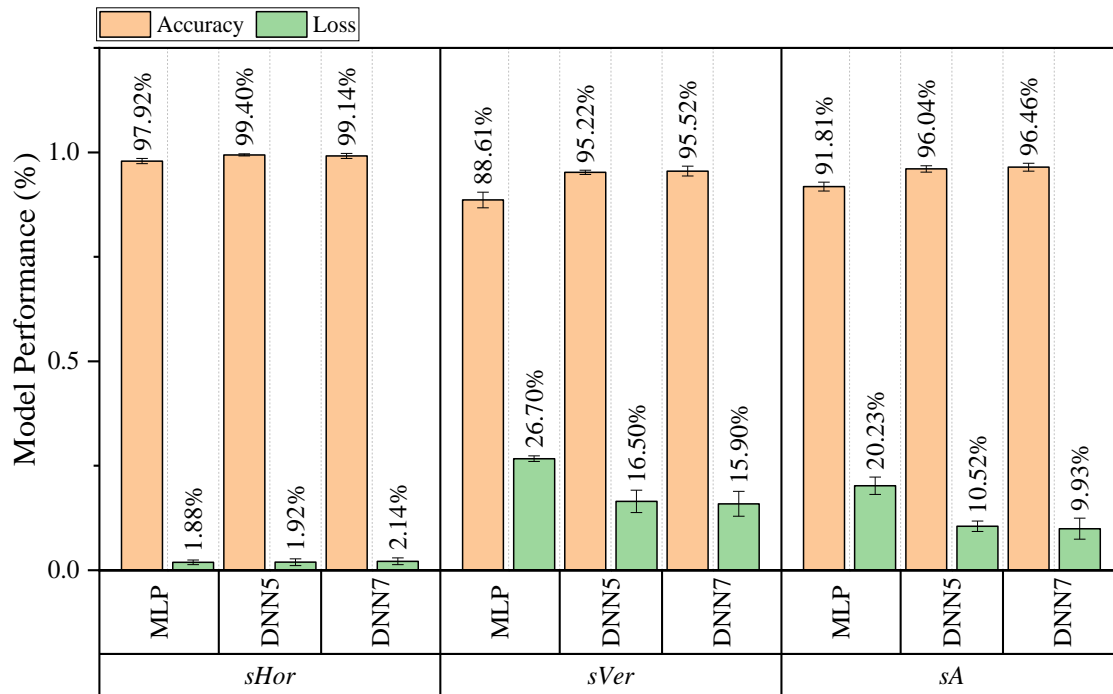
#### 3.1 ANN Evaluation Performance

Figure 3 shows the model performance of the three different models (MLP, DNN5 and DNN7) on the test datasets, namely *sVer*, *sHor* and *sA*, as explained in the methodology. The models were evaluated based on accuracy and loss. From the tested models, DNN provided higher classification accuracy with mean value above 95% as compared to MLP. At the same time, the results of the *sHor* datasets show the highest accuracy mean value of above 97% (with the lowest loss of around 2%) as compared to the other datasets.

The results from *sHor* dataset indicated slightly different accuracy for the three models used in the classification process. DNN5 showed the highest accuracy, followed by DNN7 and MLP at 99.40, 99.14 and 97.92% respectively. On the other hand, MLP with the *sVer* dataset exhibited the lowest accuracy mean value of 88.61% and the highest loss mean value of 26.70% as compared to the other models.

The results indicate that DNN5 shows the optimal number of layers for the classification. Meanwhile, the DNN7 is likely to have overfitting due to excessive information processing, while MLP may result in the underfitting due to the lack of information for capturing the data effectively (Yamashita *et al.*, 2018; Ciaburro & Iannace, 2022). Furthermore, *sHor* was found to be the best fusion dataset as it offered

more features (16) with less datasets as compared to *sVer* that provided more data with less features (8). Overall, the evaluation of model performance showed that DNN5 with the *sHor* dataset performed most efficiently in classification when compared to the other algorithm models, and this will be discussed further in the class performance.



**Figure 3: ANN model performance of accuracy and loss results for different pre-trained models and datasets.**

Based on the different datasets (*sHor*, *sVer*, and *sA*), the performances of the DNN5 model with different classes were evaluated in Figure 4. For the *sHor* datasets, all classes showed perfect precision, recall and F1-scores of 1.0, indicating that the DNN5 model performed exceptionally well on this dataset. The DNN5 model performance was particularly strong for classification of CCr, Po, LOF, LOP and N. For SI, the DNN5 model also performed well, leading to a high F1-score of 0.982.

For the *sVer* dataset classification, the DNN5 model performance demonstrated better evaluation metrics, but not consistently as compared to the *sHor* dataset. The results of precision, recall and F1-scores are satisfactory for above 0.9, with some variation between defect types. The DNN5 model performed slightly better on Po, LOP and N as compared to CCr, SI and LOF.

For the *sA* datasets, the DNN5 model performance for this dataset is generally good, but there is some variability across the defect types. It seems to perform well on Po, LOF, LOP and N with high precision, recall and F1-scores. However, its performance for CCr and SI has slightly lower F1-score of 0.915 and 0.902 respectively.

Based on the provided analysis, the DNN5 model seems to perform consistently well across most defect types and datasets, with a few variations. The *sHor* dataset generally provides the highest and most consistent performance across the defect types, followed by *sVer* and *sA*. Certain types of defects appear more challenging to the model, especially SI and CCr due to their diverse shapes and sizes, making them more difficult to identify and distinguish from other data features in defect classification (Cruz *et al.*, 2017; IAEA, 2018).

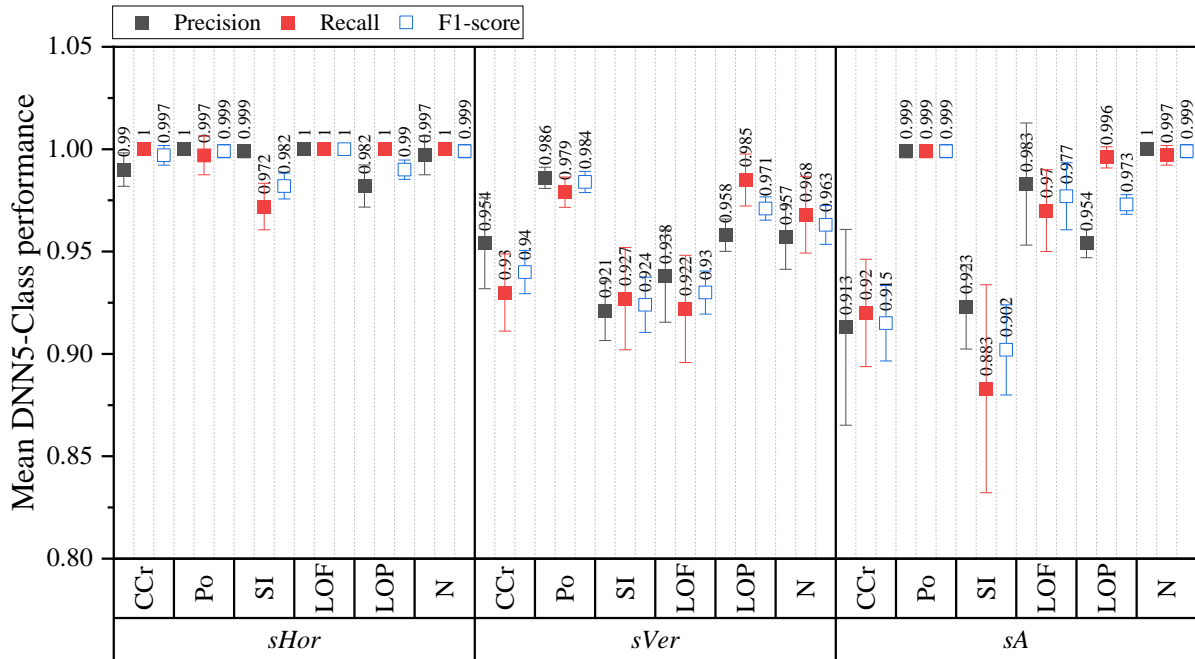


Figure 4: ANN class performance of DNN5 pre-trained model with different datasets.

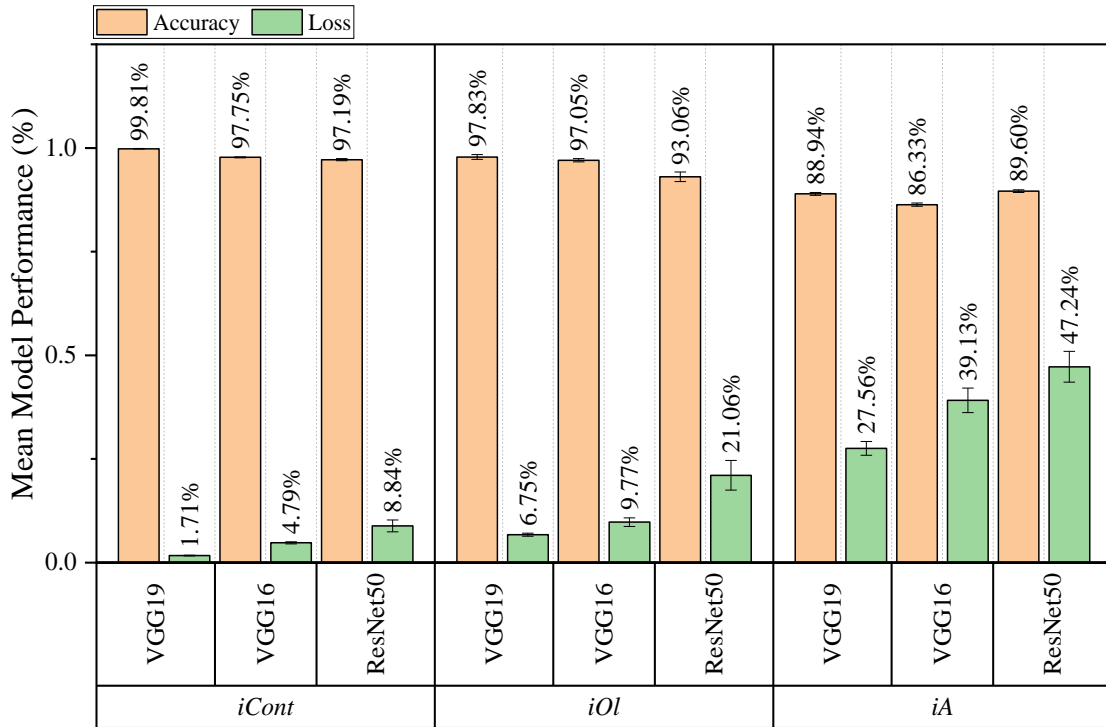
### 3.2 CNN Evaluation Performance

Figure 5 shows the model performance of three different CNN models (VGG19, VGG16 and ResNet50) on the test datasets, namely *iA*, *iOl* and *iCont*, as explained in the methodology. The models were evaluated based on accuracy and loss, whereby the *iCont* dataset showed the highest accuracy (97.2 - 99.8%) and lowest loss (1.7 - 8.8%) for the three models. Classification from the *iOl* dataset indicated slightly lower accuracy (93.0 - 97.8%) with increase in percentage of loss (6.6 - 21.0%) as shown in the figure. The results were poor for the *iA* dataset with further decrease in accuracy (86.3 - 89.6%) and significant increase in the percentage of loss (27.6 - 47.2%). This indicates that the arrangement of image matrix, specifically the fusion of datasets, can influence the classifications performance.

From the *iCont* dataset, VGG19 showed the highest accuracy, followed by VGG16 and ResNet50 at 99.81, 97.75 and 97.19% respectively. Simultaneously, the *iCont* dataset also indicated the lowest loss value, followed by VGG16 and ResNet50 at 1.71, 4.79 and 8.84%, respectively. The similar trends in accuracy and loss are also observed in the *iOl* and *iA* datasets for the three models.

The results indicate that the model performance of VGG19 is better than VGG16 and ResNet50. This is probably due to the deeper architecture of VGG19 that increases its model capacity, making it an effective tool to extract and classify features from images (Elmuogy *et al.*, 2021). These factors enable VGG19 to capture more complex patterns, reduce the risk of underfitting, and balance the risk of overfitting through regularisation techniques, resulting in improved accuracy and reduced loss. On the whole, the evaluation of model performance indicated that VGG19 with the *iCont* dataset performed the best in classification as compared to the other method models, and this will be discussed further in the class performance.





**Figure 5: CNN model performance of accuracy and loss results for different pre-trained models and datasets.**

In the CNN image classification, the performances of VGG19 models with different datasets (*iCont*, *iOl* and *iA*) for each defect type based on the provided metrics (precision, recall and F1-score) were evaluated in Figure 6. For the *iCont* dataset, the VGG19 model generally exhibited high performance metrics values of approximately 1.0 across all defect types, indicating that the model is effective at correctly classifying defects in this dataset.

The performance on the *iOl* dataset is also quite good, but there are some variations across defect types. The results of precision, recall and F1-scores are satisfactory for above 0.95, with some variation between defect types. Some defect types, such as CCr, Po, and SI, have slightly lower precision, recall, and F1-scores as compared to LOF and LOP with higher scores, similar to the *iCont* dataset.

The *iA* dataset, which contains images from side A only, shows more varied performance as compared to the fusion datasets. The VGG19 model performs well for SI and LOF that demonstrated a perfect recall of 1.0, which indicates perfect classification. However, CCr and LOP exhibited lower recall of 0.847 and 0.658 respectively, suggesting that the model struggles to correctly identify these defects in this dataset. Precision varies across defect types, indicating that while the VGG19 model can correctly identify some defect types, it might also produce false positives for others.

The *iCont* dataset, which combines information from both sides A and B, yields the most consistent and effective results. The *iOl* dataset also performs well overall but has some variations in performance across different defect types. The *iA* dataset, which only contains images from side A, proves to be the most challenging for the model, particularly for certain defect types such as CCr, LOP and Po.

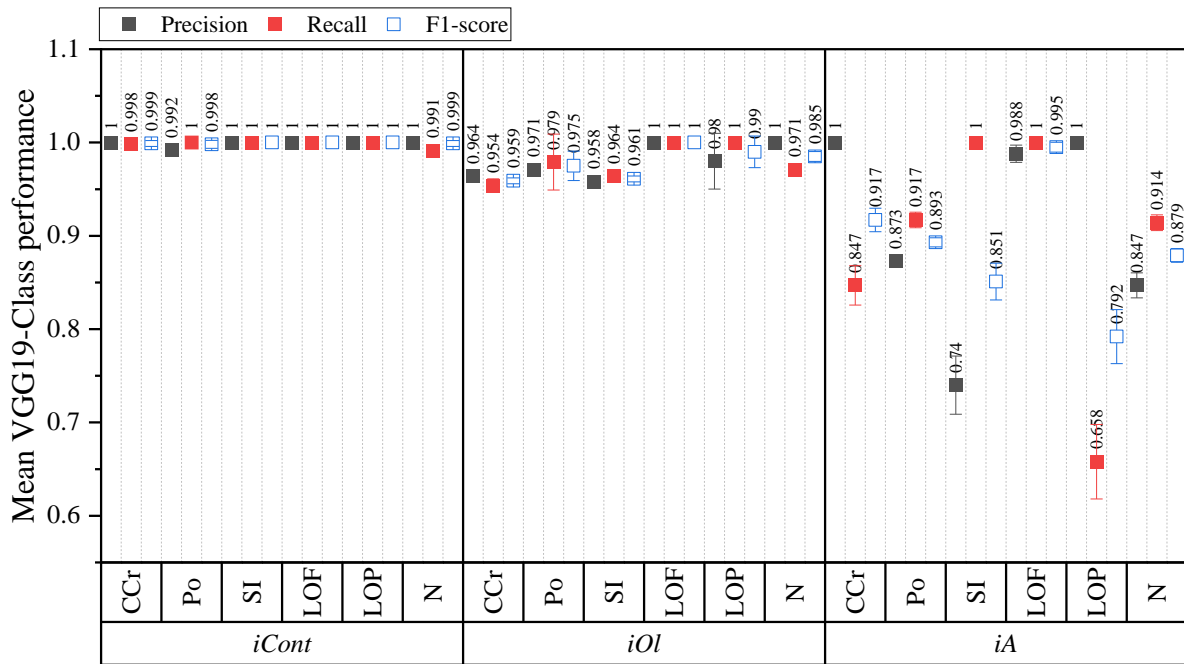


Figure 6: CNN class performance of VGG19 pre-trained model with different datasets.

### 3.3 Transfer Learning Comparison for ANN and CNN

In order to evaluate the effectiveness and quality of the ANN and CNN model performance, the best datasets obtained from Sections 3.1 and 3.2 are used. The comparison is evaluated base on accuracy and loss of both models.

The transfer learning performance of the DNN5 model for comparison with different datasets (*sHor*, *sVer* and *sA*) is shown through the accuracy and loss plots over epochs in Figure 7. It is evident that the DNN5 model with the *sHor* dataset exhibits the most stable curves, and achieves the highest training and validation accuracy. The accuracy curves for both the training and validation data experience rapid increases, reaching around 97% within the first five epochs, and then converge to over 99% after epoch 100. As for the loss curves of the training and validation data, they decrease quickly to approximately 0.1% with a high learning rate within the initial five epochs and remain stable up to 100 epochs. On the other hand, when examining the accuracy and loss curves of the *sA* and *sVer* datasets, it is noticeable that the training and validation accuracy fluctuate considerably, resulting in training accuracy of approximately 95% after 100 epochs, with a slight indication of overfitting. Similarly, the validation data accuracy curve reaches around 95% as well.

From the results, there is no significant gap observed between the training and validation curves for all the fusion datasets. Thus, it is difficult to determine whether the DNN5 model with the *sHor* dataset is overfitting or underfitting at any specific epoch, as the training and validation accuracies are nearly equal. In this experiment, the fusion datasets were applied to the training set, which made the training set easier to predict, while the validation set had a slightly higher accuracy due to the higher learning rate. Overall, the results demonstrate that the DNN5 model with the *sHor* dataset performs the best among the three fusion datasets, exhibiting stable accuracy and loss curves with high accuracy values. Conversely, both the *sA* and *sVer* datasets show more fluctuations and slightly lower accuracy, indicating potential for overfitting.

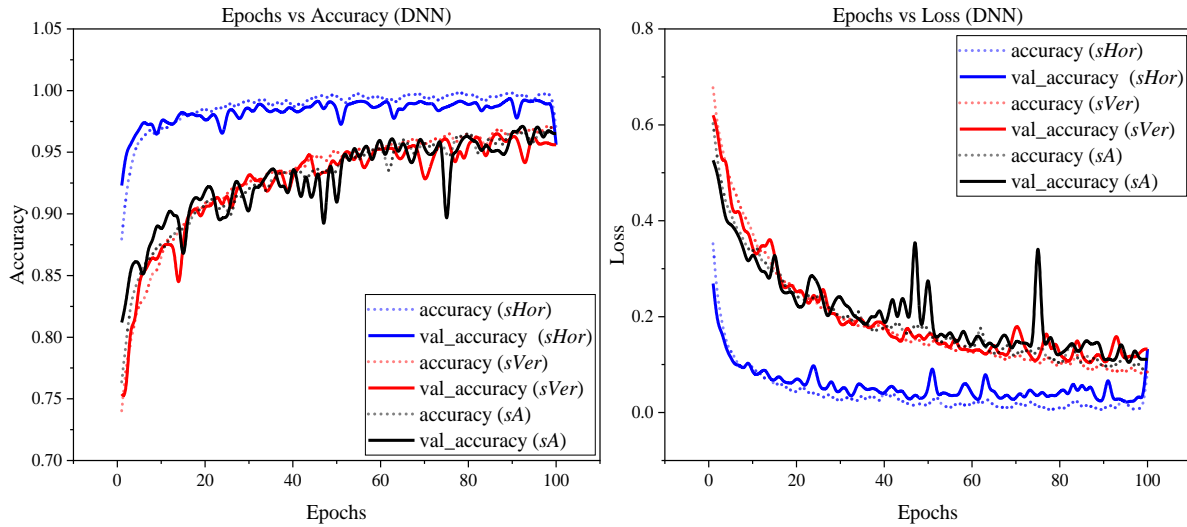


Figure 7: ANN transfer learning for the DNN5 model with different datasets.

For CNN, the accuracy and loss performance over time (epochs) for the image fusion datasets of *iCont*, *iOl* and *iA* are shown in Figure 8. It can be seen that the VGG19 model with the *iCont* dataset has the most stable curves, and provides the highest training and validation accuracy. The accuracy curve for the training and validation data increases rapidly from epoch 0 to 5 and stabilises at a value of more than 99% until epoch 100. As for the loss curve for the training and validation data, the high learning rate decreases rapidly to about 0.1% in the first five epochs and gradually remains stable thereafter.

However, for the accuracy and loss curves for the *iA* dataset, it is noted that the training accuracy fluctuates significantly and results in training accuracy of about 88% after 100 epochs with strong overfitting. Similarly, the validation curve for the *iOl* dataset reaches about 97% with slight overfitting as compared to the *iA* dataset. The validation loss curve also shows that the exponential reduction in significant learning rate is slower for the *iA* and *iOl* datasets as compared to the *iCont* dataset. Therefore, the VGG19 model with the *iCont* dataset is the most effective image fusion dataset with a higher learning rate as compared to the others.

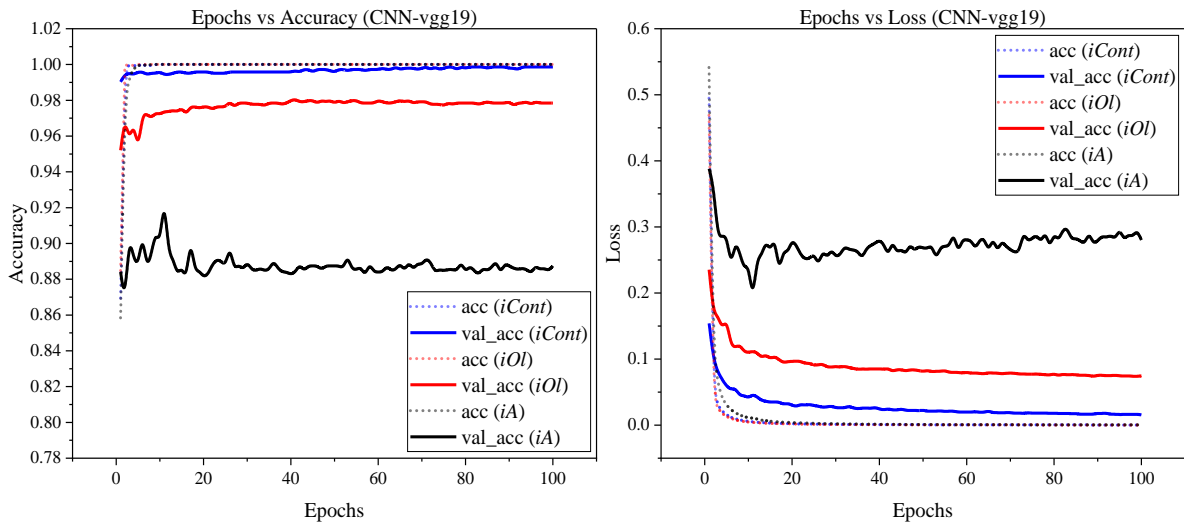


Figure 8: CNN transfer learning for VGG19 model with different datasets

## 4. CONCLUSION

The fusion datasets generated from ultrasonic signals at welds hold considerable promise as a practical alternative for defect classification with neural network algorithms. This paper undertook a thorough investigation into the manipulation of these fusion datasets to assess their efficiency in identifying a wide range of weld defects. Consequently, this study employs ANN to establish feature data, while also employing CNN to accurately predict image features.

Among the ANN models, the DNN5 (5 layers) model achieved the highest classification accuracy as compared to the MLP (3 layers) and DNN7 (7 layers) models. The *sHor* fusion dataset was particularly effective for the DNN5 model, resulting in the highest accuracy and lowest loss. This model achieved an exceptional accuracy of 99.40%, and demonstrated superior precision and recall across different defect types.

Regarding the CNN models, the VGG19 model consistently outperformed the VGG16 and ResNet50 models in terms of accuracy and loss metrics. The *iCont* fusion dataset was found to be the best choice for the VGG19 model, leading to the highest accuracy and lowest loss. The VGG19 model combined with the *iCont* dataset achieved an impressive accuracy of 99.81%, and exhibited commendable precision and recall for various defect types.

Furthermore, in the field of ANN models, the DNN5 model with the *sHor* dataset excelled in terms of accuracy, precision and recall. Similarly, among the CNN models, the VGG19 model utilising the *iCont* dataset showcased remarkable accuracy, and robust precision and recall metrics. Overall, both ANN and CNN models demonstrate their suitability for effectively identifying and classifying weld defects.

## ACKNOWLEDGEMENT

The authors would like to express their appreciation to the Ministry of Science, Technology & Innovation (MOSTI) and Malaysian Nuclear Agency for their support for this project.

## REFERENCES

- Ajmi, C., Zapata, J., Martínez-Álvarez, J.J., Doménech, G. & Ruiz, R. (2020). Using deep learning for defect classification on a small weld X-ray image dataset. *J. Nondestruct. Eval.*, **39**: 1–13.
- Amiri, N., Farrahi, G.H., Kashyzadeh, K.R. & Chizari, M. (2020). Applications of ultrasonic testing and machine learning methods to predict the static & fatigue behavior of spot-welded joints. *J. Manuf. Process.*, **52**: 26–34.
- Babu, S.K., Chan, A. & Chan, W.T. (2016). Productivity and reliability study of non destructive testing techniques for inspection of structural welds in construction industry. *19<sup>th</sup> World Conf. NDT*, **19**: 35–39.
- Bevan, R.L.T., Budyn, N., Zhang, J., Croxford, A.J., Kitazawa, S. & Wilcox, P.D. (2020). Data fusion of multiview ultrasonic imaging for characterization of large defects. *IEEE Trans. Ultrason. Ferroelectr. Freq.*, **67**: 2387–2401.
- Ciaburro, G., & Iannace, G. (2022). Machine-learning-based methods for acoustic emission testing: A review. *Appl. Sci.*, **12**: 1–30.
- Cormerais, R., Duclos, A., Wasselynck, G., Berthiau, G. & Longo, R. (2021). A data fusion method for non-destructive testing by means of artificial neural networks. *Sens.*, **21**, 1–12.
- Cruz, F.C., Simas Filho, E.F., Albuquerque, M.C.S., Silva, I.C., Farias, C.T.T. & Gouvêa, L.L. (2017). Efficient feature selection for neural network based detection of flaws in steel welded joints using ultrasound testing. *Ultrason.*, **73**: 1–8.
- Dave, V.S. & Dutta, K. (2014). Neural network based models for software effort estimation: A review. *Artif. Intell. Rev.*, **42**: 295–307.
- Droubi, M.G., Faisal, N.H., Orr, F., Steel, J.A. & El-Shaib, M. (2017). Acoustic emission method for

- defect detection and identification in carbon steel welded joints. *J. Constr. Steel Res.*, **134**, 28–37.
- Elmuogy, S., Hikal, N.A. & Hassan, E. (2021). An efficient technique for CT scan images classification of COVID-19. *J. Intell. Fuzzy Syst.*, **40**: 5225–5238.
- Esther Florence, S., Vimal Samsingh, R. & Babureddy, V. (2018). Artificial intelligence based defect classification for weld joints. *IOP Conf. Ser.: Mater. Sci. Eng.*, **402**: 1–14.
- Géron, A. (2017). Part 1: The Fundamentals of Machine Learning (Chapter 3: Classification). In Tache, N. (Ed.), *Hands-On Machine Learning with Scikit-Learn & TensorFlow* (1<sup>st</sup> ed.), O'Reilly Media, Inc.
- IAEA (International Atomic Energy Agency). (2018). *Training Guidelines in non-Destructive Testing Techniques: Manual for Ultrasonic Testing at Level 2 (IAEA-TCS-67)*. International Atomic Energy Agency (IAEA). Vienna.
- Inoue, H. (2018). Data augmentation by pairing samples for images classification. *ArXiv:1801.02929*.
- Jiang, H., Hu, Q., Zhi, Z., Gao, J., Gao, Z., Wang, R., He, S. & Li, H. (2021). Convolution neural network model with improved pooling strategy and feature selection for weld defect recognition. *Weld. World*, **65**:731–744.
- Murta, R.H.F., Vieira, F. de A., Santos, V.O. & de Moura, E.P. (2018). Welding defect classification from simulated ultrasonic signals. *J. Nondestruct. Eval.*, **37**: 1-10.
- Niccolai, A., Caputo, D., Chieco, L., Grimaccia, F. & Mussetta, M. (2021). Machine learning-based detection technique for ndt in industrial manufacturing. *Math.*, **9**: 1–16.
- Opacic, M., Sedmak, A., Bakic, G., Milošević, N. & Milovanovic, N. (2022). Application of advanced NDT methods to assess structural integrity of pressure vessel welded joints. *Procedia Struct. Integr.*, **42**: 1185–1189.
- Provencal, E. & Laperrière, L. (2021). Identification of weld geometry from ultrasound scan data using deep learning. *CIRP Conf. Manuf. Syst.*, **104**: 122–127.
- Sani, S., Saad, M.H.M., Jamaludin, N., Muhammad, N., Mohamad, S.F. & Ahmad, M.H.A.R.M. (2022). Evaluation of weld defects signal features using ultrasonic full wave pulse echo methods. *Defence S&T Tech. Bull.*, **15**: 110–123.
- Silva, L.C., Simas Filho, E. F., Albuquerque, M.C.S., Silva, I.C. & Farias, C.T.T. (2020). Segmented analysis of time-of-flight diffraction ultrasound for flaw detection in welded steel plates using extreme learning machines. *Ultrason.*, **102**: 106057.
- Sudhamayee, K. (2019). Pipeline monitoring using ultrasonic sensors. *Int. J. Eng. Adv. Technol.*, **8**: 1937-1940.
- Yamashita, R., Nishio, M., Do, R.K.G. & Togashi, K. (2018). Convolutional neural networks: an overview and application in radiology. *Insights Imaging*, **9**: 611–629.

# QUASI-STATIC INDENTATION TESTING OF STAINLESS STEEL WIRE MESH / EPOXY LAMINATED COMPOSITES

Nurul Zakiah Zamri Tan<sup>1</sup>, Azrin Hani Abdul Rashid<sup>1\*</sup>, Md. Mominur Rahman Mohd<sup>2</sup>, Mohd Yazid Yahya<sup>3,4</sup>, Mohd Yuhazri Yaakob<sup>5</sup>, Risby Mohd Sohaimi<sup>6</sup> & Anis Amirah Nor Anuwar<sup>7</sup>

<sup>1</sup>Faculty of Engineering Technology, Universiti Tun Hussein Onn Malaysia (UTHM), Johor, Malaysia

<sup>2</sup>Department of Textile Engineering, Daffodil International University, Bangladesh

<sup>3</sup>Faculty of Mechanical Engineering, Universiti Teknologi Malaysia (UTM), Johor, Malaysia

<sup>4</sup>Centre for Advanced Composite Materials, Universiti Teknologi Malaysia (UTM), Johor, Malaysia

<sup>5</sup>Faculty of Industrial and Manufacturing Technology and Engineering, Universiti Teknikal Malaysia Melaka (UTeM), Melaka, Malaysia

<sup>6</sup>Faculty of Engineering, National Defence Universiti of Malaysia (UPNM), Malaysia

<sup>7</sup>Maxim Textile Technology Sdn. Bhd., Senai, Johor

\*Email: azrin@uthm.edu.my

## ABSTRACT

*This study presents the analysis of the quasi-static indentation behaviour of stainless steel wire mesh / epoxy laminate composites, with particular focus on their energy absorption characteristics and damage under impact conditions. The research explores the performance of composites reinforced with two grades of stainless steel wire mesh, 304 and 316, with varying mesh sizes and wire diameters. The composites were fabricated using a hand lay-up technique in an open mould, ensuring consistent quality and reproducibility. The experimental setup for the quasi-static indentation tests was designed to measure the maximum indentation force, displacement at maximum force, total displacement, and energy absorbed at maximum indentation. The tests were conducted in accordance with ASTM standards, and the results were statistically analysed using Tukey's pairwise comparisons to determine significant differences between the samples. The findings reveal that the A2 (304) composite, with its finer mesh size, exhibits the highest energy absorption capacity, making it a prime candidate for applications requiring lightweight and high-impact resistant materials. The study also compares the specific energy absorption (SEA) of the samples, which is the energy absorbed per unit mass, highlighting the superior performance of the A2 sample in this regard. Damage assessment was carried out by capturing images of the front and back surfaces of the indented laminates and analysing them using ImageJ. The damage patterns, including matrix cracking, bulging, wire shearing and wire breakage, were observed and quantified. The 304 grade wire mesh composite showed larger damage areas as compared to the 316 grade composite, suggesting differences in the materials' ability to resist crack propagation and deformation under stress. The study concludes that the composition of the wire mesh, particularly the presence of molybdenum in the 316 grade, contributes to its lower deformation rate and higher resistance to crack propagation. The comprehensive analysis of the composites' impact behaviour provides valuable insights into the design and selection of materials for safety-critical applications where energy absorption and damage tolerance are important.*

**Keywords:** *Laminate composite; stainless steel wire mesh; quasi-static indentation; energy absorption; damage mode.*

## 1. INTRODUCTION

The increasing demand for polymer composite materials is driven by their exceptional performance in impact-related applications across diverse industries. The unique mechanical properties of polymer composites, including high strength-to-weight ratio, impact resistance and energy absorption

capabilities, have positioned them as indispensable materials for applications where impact performance is critical. Industries such as automotive, aerospace, sports equipment and protective gear have increasingly relied on polymer composites to enhance impact resistance and structural integrity, thereby fuelling the demand for advanced composite materials. Researchers have been drawn to investigate various materials for impact applications, particularly focusing on natural fibres and innovative reinforcement techniques (Malingam *et al.*, 2018; Feng *et al.*, 2020; Nik Ismail *et al.*, 2023). One such reinforcement material that has garnered significant attention is wire mesh, which offers unique opportunities for enhancing the impact resistance and structural integrity of composite materials. Studies have explored the incorporation of wire mesh as a reinforcement component in composite materials to address impact-related challenges and improve overall performance (Asavavisithchai *et al.*, 2018; Wang *et al.*, 2022).

Similarly, the study by Mahdad *et al.* (2018) emphasised on the potential for more durable and impact-resistant materials through the use of stainless steel wire mesh laminates as compared to glass fibre laminates, indicating improved safety and longevity for critical applications. Additionally, Asavavisithchai *et al.* (2018) presented significant advancement in ballistic protection, offering enhanced ballistic resistance, cost-effectiveness and weight reduction through the development of composite armours using natural rubber reinforced with stainless steel wire mesh. Krishnasamy *et al.* (2021) highlighted the potential for hybrid composites reinforced with jute fibre and 304 wire mesh in epoxy resin to be utilised in lightweight applications due to their high mechanical properties and low density, offering advancements in energy absorption and impact resistance. The findings by Sakthivel *et al.* (2017) indicated the potential for incorporating stainless steel wire mesh in glass fibre reinforced composites to significantly enhance their performance, particularly in terms of impact resistance and energy absorption.

Table 1 provides a comprehensive overview of the characteristics and testing parameters associated with various types of wire mesh utilised in composite materials. The studies encompass a diverse range of wire mesh materials, including 304 stainless steel, glass wire mesh, stainless steel fine and aluminium 2200. The studies were conducted to explore the potential of wire mesh in various applications, such as for ballistic panels (Asavavisithchai *et al.*, 2018; Arulmurugan *et al.*, 2023) and automotive body parts (Elumalai *et al.*, 2022). Each entry in Table 1 details the specific manufacturing method employed, type of matrix used and impact test velocity. The parameters that influence energy absorption include stacking sequence (Sakthivel *et al.*, 2017), interfacial bonding, impact energy, impactor mass, wire mesh orientation (Krishnasamy *et al.*, 2021), type of reinforcement (Arunprakash *et al.*, 2018), density of wire mesh (Asavavisithchai *et al.*, 2018; Alev *et al.*, 2023) and material of wire mesh of composite layers. (Alev *et al.*, 2023). This comprehensive compilation offers valuable insights into the impact of wire mesh characteristics on energy absorption in composite materials, providing a holistic view of the research landscape in this domain.

**Table 1: Previous research on wire mesh as reinforcement material in composites.**

Type of Wire Mesh	Manufacturing Method	Matrix Use	Impact Testing
304 stainless steel (Sakthivel <i>et al.</i> , 2017)	Hand lay-up and vacuum bag moulding	Epoxy resin	Low-velocity impact tests
304 stainless steel (Wang <i>et al.</i> , 2021)	Not specified	Not specified	Low-velocity impact tests
304 stainless steel (Krishnasamy <i>et al.</i> , 2021)	Hand lay-up method	Epoxy	-
Glass wire mesh (Alev <i>et al.</i> , 2023)	Vacuum infusion method	Epoxy	Low-velocity impact tests
Stainless steel fine (Mahdad <i>et al.</i> , 2018)	Compression moulding technique	Polypropylene (PP)	Quasi-static indentation tests
Stainless steel (Asavavisithchai <i>et al.</i> , 2018)	Embedding into pre-vulcanised natural rubber latex	Natural rubber (NR) latex	Ballistic impact test
Aluminium 2200 (Arulmurugan <i>et al.</i> , 2023)	Hand lay-up and vacuum bag moulding	Epoxy resin	Ballistic impact test

Quasi-static indentation testing has emerged as a popular method for gaining fundamental insights into the impact behaviour and performance of composite materials (Lu *et al.*, 2003; Sutherland *et al.*, 2012). This testing approach provides valuable data on material response to localised loading, offering crucial insights into the mechanical properties and impact resistance of polymer composites, thereby informing on material design and optimisation strategies (Fernandes *et al.*, 2014; Wagih *et al.*, 2016; Pach *et al.*, 2021). Despite extensive research on wire mesh reinforcement and impact testing, there exists a notable research gap pertaining to the comparison of different grades of stainless steel wire mesh (grades 304 and 316) under quasi-static loading conditions. The selection of the two grades of stainless steel wire mesh for quasi-static indentation test is based on their widespread use and availability in the market. The findings of the study conducted by Zhao *et al.* (2023) on using grade 316 wire mesh in laminated composites subjected to ballistic impact testing suggest that this grade along with grade 304 show promise for high-end applications. However, comparative studies are limited, which are essential to ascertain the most effective material selection among the various wire mesh grades to unlock their highest potential. Therefore, a comparative analysis of the mechanical properties, failure modes, and energy absorption capacities of these two stainless steel wire mesh grades is conducted in this study.

The objective of this study is to assess the behaviour of stainless steel wire mesh / epoxy laminated composites under quasi-static indentation. It compares the performance of 304 and 316 mesh grades, which vary in mesh size and wire diameter. The assessment of their impact performance is conducted through quasi-static indentation tests. The results are analysed in terms of force-displacement curve, energy absorption and damage. Additionally, statistical analysis is employed to evaluate the impact behaviour of the different grades of stainless steel wire mesh laminated composites.

## 2. MATERIAL AND METHODS

### 2.1 Epoxy SP84 and Hardener SP76

The matrix system for the composite fabrication containing Epoxy (SP84) and hardener (SP76) was supplied by the Penchem Technologies, Malaysia. The SP84 epoxy is a high purity bisphenol A diglycidylether with density of 1.16 g/ml at 25 °C and viscosity of 4,000 – 6,000 cps. This type of resin ensures consistent performance and remarkably low viscosity, low chloride content and light colour. It is also suitable for a wide variety of curing agents at ambient temperatures. It is also easy to work with in hand lay-up applications and allows for easy air release (Dow Chemical Company, 2009).

### 2.2 Wire Mesh

The materials used in this study were austenitic stainless steel of grades 304 and 316, which were procured from Malaysia Wire Mesh. The wire meshes were cut into sizes of 100 x 100 mm. The wire meshes that were used to produce laminate composites are shown in Figure 1. The number of holes in one inch of the mesh is the mesh size. The holes are smaller when the mesh size is higher. For example, the holes of a 20 mesh are smaller than those of a 16 mesh. For example, a 16 mesh has 16 openings per inch, while a 20 mesh has 20 openings per inch. The higher the mesh number, the smaller the openings and the finer the mesh. The manufacturers provided the mesh specifications, which included the number of openings per inch (mesh size), diameter of the wire and aperture of mesh size. Their sample codes and characteristics are listed in Table 2.

**Table 2: Physical properties of stainless steel wire mesh.**

Alloy	Mesh Size	Sample Code	Wire diameter (mm)	Aperture mesh size (mm)
304 stainless steel	16 x 16	A1	0.24	1.35
	20 x 20	A2	0.24	1
316 stainless steel	16 x 16	B1	0.4	1.19
	20 x 20	B2	0.4	0.7



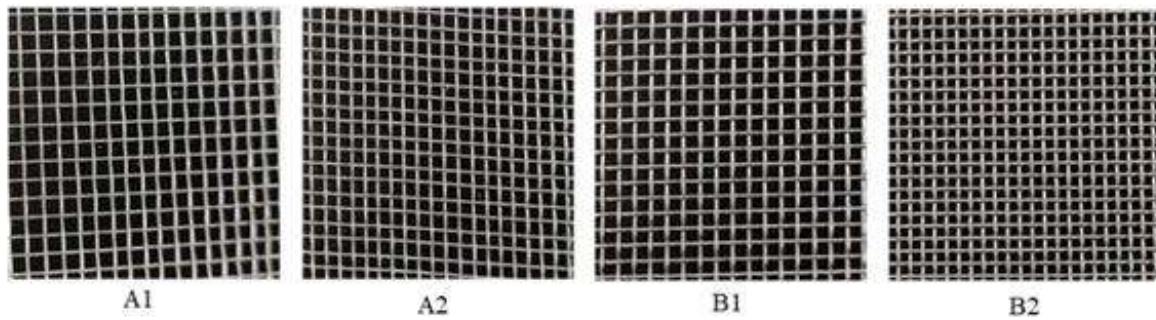


Figure 1: Four grades of wire mesh used in this study.

### 2.3 Fabrication of Composites

In this study, four varieties of laminate composites were prepared. Table 3 presents the physical properties of all the wire mesh composites. The laminate composites were fabricated using the hand layup method in an open mould at room temperature as shown in Figure 2. For the purpose of binding wire mesh lamina, epoxy (SP84) and hardener (SP76) were combined in a ratio of 5:1 epoxy-hardener. The wire mesh was then meticulously stacked on top of one another. Epoxy resin was applied to each layer separately. An aluminium plate was used as an open mould and placed on a flat surface, with a plastic material positioned on top of the plate to facilitate the detachment of the wire mesh laminate composite. The wire mesh lamina was then applied to the plastic material, and the wire mesh was arranged while epoxy was applied in successive layers until the desired layer was reached. In order to construct composites with thickness greater than 3 mm, varying quantities of layers were utilised for each composite type. Types A1 and A2 wire mesh laminate composites consisted of eight layers, whereas types B1 and B2 wire mesh laminate composites consisted of five layers. Each wire meshes was then encased in plastic, and an additional aluminium plate was placed on top. The aluminium with the wire meshes was clamped using a G-clamp to apply pressure to the composite. The composite was left to cure at ambient temperature for 24 h. Subsequently, the clamps were removed and the plastic wrap was detached from the wire mesh laminate composite.

Table 3: Wire mesh laminate composite physical properties.

Sample Code	Number of layers	Laminate Thickness (mm)	Areal density (kg/m <sup>2</sup> )
A1	8	4.05 ± 0.19	7.02 ± 0.28
A2	8	4.75 ± 0.22	7.18 ± 0.20
B1	5	4.44 ± 0.08	9.79 ± 0.13
B2	5	4.23 ± 0.15	8.63 ± 0.22



Figure 2: Laminating process of wire mesh composite.

## 2.4 Quasi-Static Indentation Test

Figure 3 depicts the experimental configuration, showcasing the placement of the sample, indenter and fixture with a hollow support at the centre. The quasi-static indentation test was carried out utilising a 50 kN GOTECH universal testing machine. A hemispherical-tipped indenter made of stainless steel, with a tip diameter measuring 12.7 mm, was utilised in compliance with ASTM D6264: Standard Test Method for Measuring the Damage Resistance of a Fibre-Reinforced Polymer-Matrix Composite to a Concentrated Quasi-Static Indentation Force. The quasi-static indentation tests were conducted under displacement control, utilising a fixed loading rate of 1.27 mm/min. The sample was secured between both plates to avoid the sample from detaching from the support when load is subjected on the composite. Each wire mesh laminate composite underwent three repeated indentation tests, and the average findings were recorded for analysis and evaluation (12 samples in total). The quasi-static indentation test responses were focused on the maximum indentation force, energy absorption and damage of all wire mesh laminate composites.

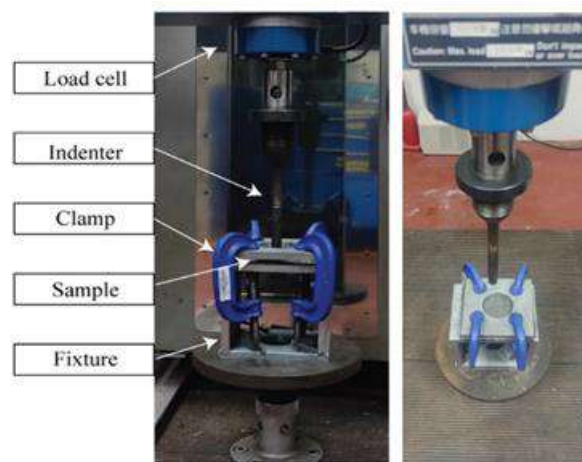


Figure 3: Experimental setup for quasi-static indentation test.

## 2.5 Statistical Analysis

For this study, statistical evaluations were conducted using the Minitab software (Version 20.4) to assess the difference in impact behaviour among various grades of wire mesh laminate composites. Impact behaviour is characterised by several response parameters, including maximum force during indentation, displacement at maximum force, total displacement, energy absorbed at maximum force ( $TEA^{max}$ ), total energy absorbed (TEA), energy of crack propagation, ductility index, specific energy absorbed at maximum force ( $SEA^{max}$ ), specific energy absorbed (SEA), and impact resistance. When significant discrepancies were detected, Tukey's pairwise comparison test was utilised. This test method allows for the assessment of all possible mean pairs to identify significant differences between the means of multiple groups, acknowledging the complexity involved in multiple comparisons. The test outcomes showed that there were statistically significant differences among the tested wire mesh laminate composites, with significance level established at  $p < 0.05$ .

## 2.6 Damage Assessment

The method involved conducting damage assessment of the wire mesh laminate composites under quasi-static conditions using hemispherical steel indenters. Following the quasi-static penetration test, the front and back surfaces of the laminates were photographed to capture the damage. Additionally, the damage assessment included scanning the samples with a Brother DCP-T500W flatbed scanner, and adjusting brightness and contrast to facilitate the measurement of the damaged area using ImageJ, as shown in Figure 4.

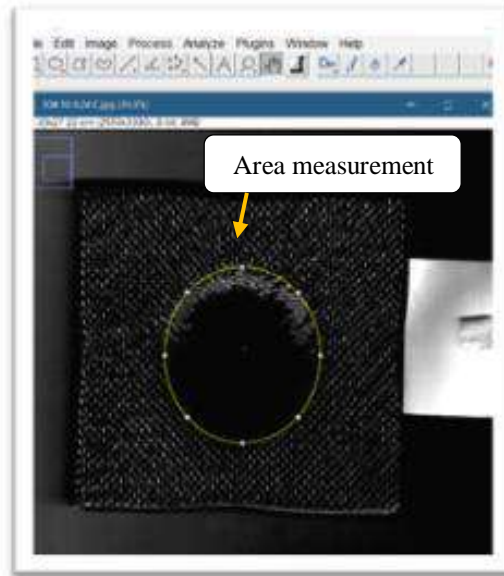


**Figure 4: Measurement of the area of the front surface using ImageJ.**

### 3. RESULTS AND DISCUSSION

The quasi-static indentation behaviour of the wire mesh laminate composites was investigated under controlled conditions. An indenter pressed into the composites during the test allowed for the measurement of the maximum indentation force and associated crosshead displacement. Upon the test's completion, each sample underwent damage assessment. The energy absorption related to the indentation process was determined by calculating the area beneath the force-displacement curve. This curve, which encapsulates the force and displacement data acquired, served as the basis for evaluating the quasi-static indentation outcomes. Characteristically, the curves shared a similar pattern, delineated into three distinct phases: elastic, damage and frictional (Yahaya *et al.*, 2014; Pach *et al.*, 2021). Specifically, Phase I corresponds to the elastic region, Phase II to the damage region and Phase III to the friction region.

Figure 5 illustrates the force-displacement curve and the material's behaviour during the quasi-static indentation test. During the elastic phase, the indenter was moved deeper into the vertical axis by increasing the applied force. The wire mesh laminate composites were deformed elastically and the force required to continue indenting is exactly proportional to its displacement. The slope of the force-displacement curve in the Phase I region indicates the stiffness of the wire mesh laminate composites. An increase in both height and steepness of the peak on the curve indicates that the sample being tested possesses better stiffness. The force-displacement curve displays a linear relationship throughout this elastic phase.

Meanwhile, in the damage phase, the force-displacement curve abruptly increases due to the incapacity of the wire mesh laminate composite to deform and accommodate the indenter. This demonstrates that the wire mesh laminate composite has reached its yield point and can no longer deform elastically. As the indenter is driven further, the wire mesh laminate composite begins to deform plastically and the force-displacement curves flatten gradually. At this time, the layer of epoxy matrix was cracked, weakening its overall strength and stiffness. The force-displacement curve at the frictional phase is nearly flat at the plateau because of the frictional force between the indenter and wire mesh laminate composite. During this phase, the force to move the indenter further remains constant and reaches its ultimate strength. In this test, the indentation ceases when the wire mesh breaks, creating a dome, and there is no total penetration owing to the indentation. In the final phase, the curve shows fluctuations and a generally downward trend, indicating a decrease in the load-bearing capacity of the material. This phase is associated with penetration and increased friction, leading to the breaking point where the material ultimately fails and breaks apart.

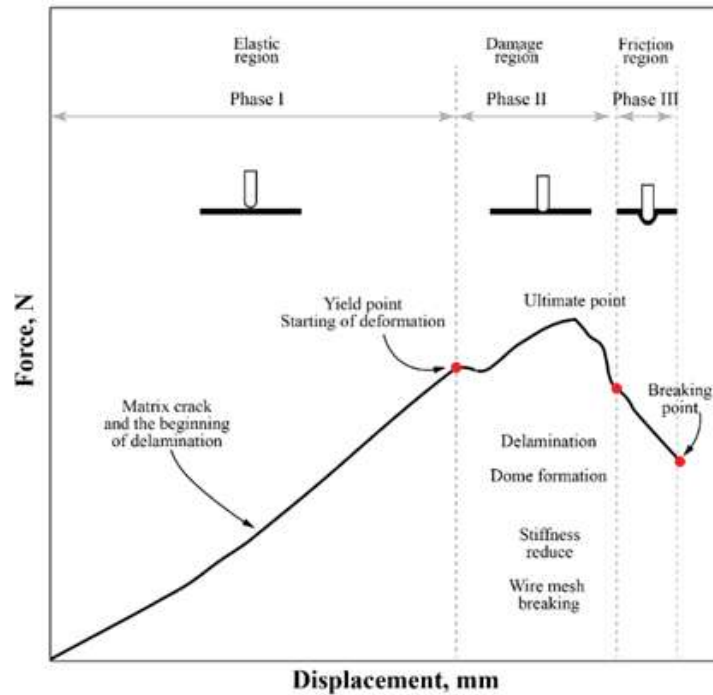


Figure 5: Force–displacement curve for the wire mesh laminate composites (Bulut *et al.*, 2018).

### 3.1 Impact Response of A1 and A2 Wire Mesh Laminate Composites

Figure 6 depicts the force-displacement curves of the A1 and A2 wire mesh laminate composites. The samples comprised of eight layers of wire mesh, with aperture mesh sizes of 1.35 and 1 mm, respectively. It demonstrates that the force-displacement response for each kind of wire mesh laminate composite varied significantly. It was observed that A2 achieved the highest maximum load of 7.78 kN, while it is 5.70 kN for A1. A steeper slope suggests a higher Young's modulus, indicating that the material is stiffer, and takes greater effort to deform or stretch. This is due to the fact that material with greater Young's modulus is better able to retain its shape under stress or strain. The samples traverse all three phases under the force-displacement curve, elastic, damage and frictional, and hence their trends are identical. A2 showed the maximum indentation force with higher maximum displacement as compared to the A1. This indicates that A2 has better strain to failure property as compared to A1.

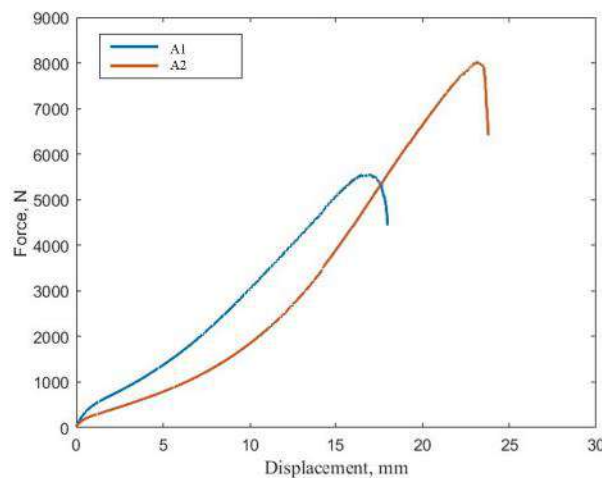


Figure 6: Force-displacement curves for A1 and A2 wire mesh laminate composites.

Table 4 presents the impact response data for the A1 and A2 wire mesh laminate composites, including maximum indentation force, displacement at maximum indentation force, total displacement, energy absorbed at maximum indentation and total energy absorbed. Meanwhile, Table 5 displays the values for propagation energy, ductility index, specific total energy absorbed and impact strength. The mean results and standard deviations for three repetitions of the test are provided in both tables. Tukey's pairwise comparisons were utilised to analyse the mean grouping results, providing valuable insights into the significant differences between A1 and A2. This statistical tool is effective for comparing the means of multiple groups, aiding in the determination of any significant discrepancies.

The total energy absorbed (TEA) for A1 and A2 indicates significantly different means, denoted by the superscript letters 'a' and 'b', signifying the substantial difference between the two groups. This suggests that A2 exhibits superior impact performance as compared to A1, with energy absorption values of 77.85 and 51.50 J, respectively. Specific energy absorption (SEA), representing the energy absorbed per unit mass of the sample, was calculated using the equation:  $SEA = TEA / \text{mass}$ . The results indicate that A2 possesses higher SEA as compared to A1, with mass values of 0.077 and 0.075 kg respectively. The force-displacement curve and tabulated results demonstrate consistent correlation, with no statistically significant discrepancies observed in the propagation and ductility indices between the two wire mesh laminate composites.

The impact response data and statistical analysis reveal that A2 exhibits superior energy absorption and impact performance as compared to A1. The SEA values further emphasise the enhanced capabilities of A2 in absorbing energy, highlighting its potential for various applications requiring high impact resistance.

**Table 4: Mean scores of impact response for the A1 and A2 wire mesh laminate composites.**

Type of sample	Maximum indentation force (kN)	Displacement at maximum indentation force (mm)	Total displacement (mm)	Energy absorbed at maximum indentation (J)	Total energy absorbed (TEA) (J)
A1	5.70±0.41 <sup>b</sup>	19.61±2.32 <sup>a</sup>	20.56±2.50 <sup>a</sup>	46.44±3.04 <sup>b</sup>	51.50±1.14 <sup>b</sup>
A2	8.00±0.01 <sup>a</sup>	22.98±0.28 <sup>a</sup>	23.65±0.21 <sup>a</sup>	72.63±6.58 <sup>a</sup>	77.85±0.57 <sup>a</sup>

\*Means that do not share a letter are significantly different.

**Table 5: Mean scores of propagation energy, ductility index, specific energy absorbed and impact strength for the A1 and A2 wire mesh laminate composites.**

Type of sample	Propagation Energy (J)	Ductility index	Specific energy absorbed (SEA) (J/kg)	Impact strength (J/m <sup>2</sup> )
A1	5.06±1.96 <sup>a</sup>	10.38±4.79 <sup>a</sup>	7.35±0.47 <sup>b</sup>	368±24.10 <sup>b</sup>
A2	5.21±0.58 <sup>a</sup>	14.02±1.44 <sup>a</sup>	10.29±0.03 <sup>a</sup>	576.48±4.44 <sup>a</sup>

\*Means that do not share a letter are significantly different.

### 3.2 Impact Response of B1 and B2 Wire Mesh Laminate Composites

Figure 7 illustrates the force-displacement curves for the B1 and B2 wire mesh composite laminate composites. The samples have five layers of wire mesh, with aperture mesh sizes of 1.19 and 0.7 mm respectively. Each of the samples attained the maximum force, with B2 displaying better maximum force as compared to B1, as evidenced by the recorded values of 8.19 and 5.95 kN respectively. This suggests that B2 exhibited better ability to resist deformation under load, indicating its better mechanical properties in comparison to B1. Multiple peaks are noticed in the curve for B2, which is due to fibre rupture (Bulut *et al.*, 2018).

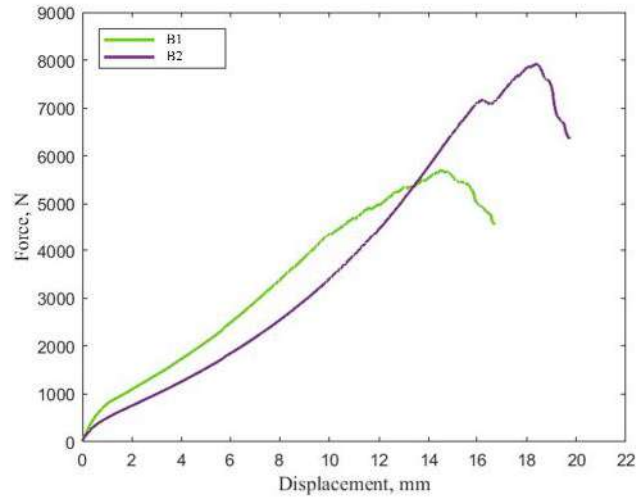


**Figure 7: Force-displacement curves for B1 and B2 wire mesh laminate composites.**

From Table 6, the TEA for B1 and B2 is concluded to be significantly different as the Tukey’s pairwise comparisons show a dissimilar superscript letter with the obtained TEA values of 55.40 and 75.17 J respectively. Meanwhile the energy absorbed at maximum indentation force are and 45.84 and 66.32 J respectively. For both samples, the propagation energy and ductility index listed in Table 7 are inferred as not significantly different means. In this study, it is clear that B2 has higher SEA as compared to B1. The force-displacement curve and tabulated results demonstrate a consistent correlation, wherein the propagation and ductility indices exhibit no statistically significant discrepancies.

**Table 6: Mean scores of impact response for the B1 and B2 wire mesh laminate composites.**

Sample	Maximum indentation force (kN)	Displacement at maximum indentation force (mm)	Total displacement (mm)	Energy absorbed to peak load (J)	Total energy absorbed (TEA) (J)
B1	5.95±0.33 <sup>b</sup>	14.87±0.33 <sup>b</sup>	16.60±0.66 <sup>b</sup>	45.84±0.85 <sup>a</sup>	55.40±3.48 <sup>b</sup>
B2	8.19±0.38 <sup>a</sup>	18.90±0.72 <sup>a</sup>	20.07±0.50 <sup>a</sup>	66.32±1.83 <sup>a</sup>	75.14±0.57 <sup>a</sup>

\*Means that do not share a letter are significantly different.

**Table 7: Mean scores of propagation energy, ductility index, specific energy absorbed and impact strength for the B1 and B2 wire mesh laminate composites.**

Sample	Propagation energy (J)	Ductility index	Specific energy absorbed (SEA) (J/kg)	Impact strength(J/m <sup>2</sup> )
B1	9.57±3.67 <sup>a</sup>	5.49±2.75 <sup>a</sup>	5.66±0.28 <sup>b</sup>	363.79±6.76 <sup>b</sup>
B2	8.82±1.26 <sup>a</sup>	7.62±1.30 <sup>a</sup>	8.81±0.27 <sup>a</sup>	526.4±14.5 <sup>a</sup>

\*Means that do not share a letter are significantly different.

### 3.3 Comparison of All 304 and 316 Grade Wire Mesh Laminate Composite Samples

For all the types of wire mesh laminate composite samples, it can be concluded that for the TEA for each sample, as shown in Table 8, there are two groups of samples that can be inferred to be significantly different. This is because they share different superscript letters ‘a’ and ‘b’. Tukey’s pairwise comparison concludes A2 and B2 have similar capability of TEA, as they share the same superscript letter ‘a’. Similarly, A1 and B1 were not found to be significantly different, as they share the same

superscript letter 'b'. The number of layers, shown in the superscript letter 'a' cluster, appears to have no significant effect on the TEA, as A2 has eight layers, while B2 has five layers. In addition, the two samples have different wire diameters of 0.24 and 0.4 mm respectively. The same applies to the 'b' cluster. In general, from Tukey's pairwise comparisons, A2 and B2 have the highest TEA values.

**Table 8: Tukey's pairwise comparison of TEA for all the samples.**

Type of sample	Layers	Total energy absorbed (TEA) (J)
A1	8	51.50±1.14 <sup>b</sup>
A2	8	77.85±0.57 <sup>a</sup>
B1	5	55.40±3.48 <sup>b</sup>
B2	5	75.14±0.57 <sup>a</sup>

In order to evaluate the maximum indentation test, as shown in Table 9, Tukey's pairwise comparisons reveal that the means for samples B2 with five layers and A2 with eight layers are not significantly different and are denoted with the same letter 'a'. Similarly, the means for samples B1 with five layers and A1 with eight layers are also not significantly different and are denoted by the letter 'b'. However, the means for the samples in different groups a and b are significantly different from each other. The observation is similar to the findings for TEA. Higher maximum indentation force may indicate a more durable material that can withstand greater impact forces.

**Table 9: Tukey's pairwise comparison of maximum indentation for all the samples.**

Type of sample	Layers	Maximum indentation force (kN)
A1	8	5.95±0.33 <sup>b</sup>
A2	8	8.00±0.01 <sup>a</sup>
B1	5	5.70±0.41 <sup>b</sup>
B2	5	8.19±0.38 <sup>a</sup>

When considering the weight and calculating the SEA for all the samples, as shown in Table 10, the highest SEA value is for sample A2, followed by B2, A1 and B1 as in Table 10. All the results were found to be significantly different for all the samples through Tukey's pairwise comparisons. If all samples are compared for the purpose of lightweight polymer composite usage, sample A2 has the highest potential.

**Table 10: Tukey's pairwise comparison of SEA for all the samples.**

Type of sample	Specific energy absorbed (SEA) (J/kg)	Weight (kg)
A1	7.34±0.47 <sup>c</sup>	0.105
A2	11.03±0.10 <sup>a</sup>	0.077
B1	5.66±0.28 <sup>d</sup>	0.075
B2	8.81±0.27 <sup>b</sup>	0.092

Based on the given results, it can be implied that the 304 grade samples (A1 and A2) have higher ductility and lower propagation energy as compared to the 316 grade samples (B1 and B2) that have lower ductility and higher propagation energy. The higher ductility of the 304 grade samples indicates that it can undergo greater plastic deformation before failure. On the other hand, the lower ductility of the 316 grade samples suggests that it is less deformable and more likely to fail under tensile loads. The higher propagation energy of the 316 grade samples suggests that it is more resistant to crack propagation and has better fracture toughness as compared to the 304 grade samples. This makes the 316 grade samples more suitable for applications where high resistance to cracking and fracture is required.

### 3.4 Damage Assessment

The damage surfaces of wire mesh laminate composites were indented under quasi-static condition by hemispherical steel indenters. After the quasi-static penetration test, photos were captured of both the front and back surfaces of the laminates. Figure 8 shows close ups of the most damaged area, which is on the area that was penetrated with the indenter. For all the samples, the bulging creates a dome with similar shape to hemispherical tip indenter. Damages were observed in all the wire mesh laminate composites related to matrix cracking, bulging, wire shearing and wire breakage. The damages caused reduction in strength and stiffness as well as material deformation, leading to failure. Both grades of wire mesh laminate composites, 304 (A1 and A2) and 316 (B1 and B2) showed the same behaviour of failure mode. Each wire mesh laminate composite showed slight delamination of mesh and no full penetration.

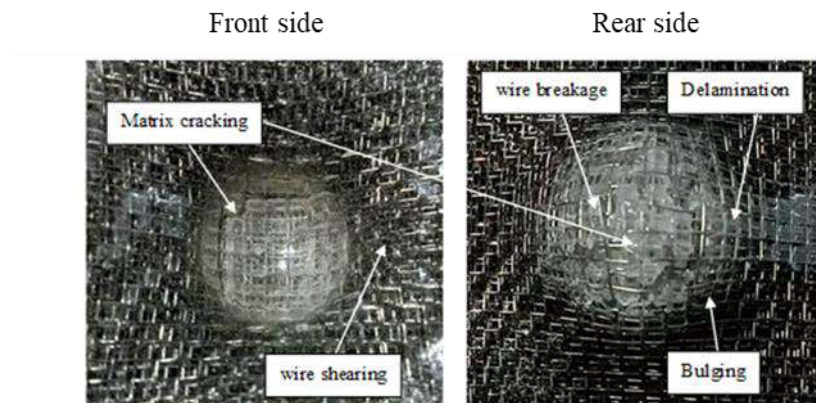










**Figure 8:** Close ups of the most damaged area on front and rear sides for the samples.

In general, a circular shape was noticed on the front side of each sample surrounding the contact region between the indenter and the samples. The damages on the front and back surfaces of each sample are shown in Table 11. The dimensions of the circular shape are compared to the propagation energy detailed in Tables 5 and 7. This comparison emphasises the resistance to crack propagation exhibited by the 304 grade samples, labelled A1 and A2, which show lower resistance in comparison to the 316 grade samples, B1 and B2. Additionally, the magnitude of damage in the 304 grade samples is greater than that observed in the 316 grade samples. Tukey's pairwise comparisons showed that samples A1 and A2 belong to the same group of means. This is also observed for samples B1 and B2. These two group means have been inferred to be significantly different. It is possible that the wider ability of grade 316 wire mesh laminate composites (B1 and B2) to restrain crack propagation can be attributed to the composition of its constituent materials, which includes molybdenum that have lower deformation rate when subjected to stress and strain as compared to grade 304 wire mesh wire mesh laminate composites (A1 and A2) (Martins *et al.*, 2014).

The propagation energy values in this study, 5.06 J for A1, 5.21 J for A2, 9.57 J for B1 and 8.82 J for B2, indicate the energy needed to propagate a crack. Higher propagation energy typically signifies better resistance to crack growth, leading to potentially smaller damage areas upon impact. Figure 12 suggests that A1 and A2 have higher damage areas due to lower propagation energy as compared to B1 and B2.



**Table 11: Surface damage (front and back) and penetration behaviour.**

Sample	Front	Back	Damage area (front) (cm <sup>2</sup> )
A1			$21.24 \pm 0.95^b$
A2			$21.78 \pm 0.20^b$
B1			$17.59 \pm 0.35^a$
B2			$18.69 \pm 0.13^a$

\*Means that do not share a letter are significantly different.

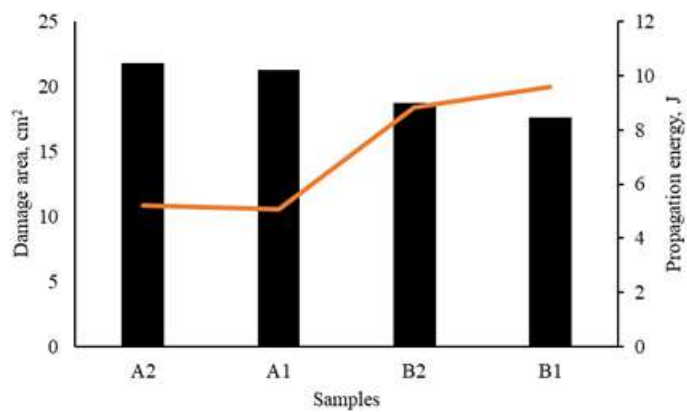


**Figure 12: The relation of damage area and propagation energy.**

#### 4. CONCLUSION

The comprehensive study on the quasi-static indentation behaviour of stainless steel wire mesh / epoxy laminate composites has yielded significant insights into their energy absorption characteristics and damage under impact conditions. The research focused on two grades of stainless steel wire mesh, 304 and 316, with varying mesh sizes and wire diameters, fabricated using a hand lay-up technique to ensure consistent quality. The experimental results, guided by ASTM standards, revealed that the A2 composite, which utilises a finer mesh of the 304 grade, possesses the highest energy absorption capacity. These findings position A2 as an ideal material for applications that demand lightweight structures with exceptional impact resistance. The SEA of A2 was also found to be the highest among the samples tested, indicating its superior efficiency in absorbing energy relative to its mass.

Damage assessment conducted through visual analysis and ImageJ software quantification showed that the 304 grade wire mesh composites exhibited larger damage areas as compared to the 316 grade composites. This suggests that the 316 grade, with its inclusion of molybdenum, offers lower deformation rate and greater resistance to crack propagation, making it more suitable for applications where high resistance to cracking and fracture is required. The statistical analysis using Tukey's pairwise comparisons highlighted significant differences in the impact behaviour among the wire mesh laminate composites. The A2 and B2 samples demonstrated similar capabilities in TEA, despite differences in wire diameters and the number of layers, indicating that both grades have high TEA values and are not significantly different in their impact resistance. The 304 grade composites, despite their large damage areas, have lower propagation energies, suggesting a predisposition towards easier crack extension. However, their considerable TEA implies that they can withstand significant energy inputs before failure. In contrast, the 316 grade composites exhibited smaller damage areas and higher propagation energies, indicating a stronger resistance to crack propagation. Their substantial TEA values demonstrate overall material toughness. These distinctions highlight the superior mechanical resilience of the 316 grade, which combines both higher resistance to crack propagation and ample energy absorption capacity. The relationship between energy absorption and damage is critical for materials used in situations where absorbing and dissipating energy is important, such as in impact resistant materials and protective gear.

In summary, the study concludes that the composition and structure of the wire mesh reinforcement are critical factors in the performance of laminate composites under impact loading. The A2 composite, with its finer mesh size and superior energy absorption, is particularly promising for lightweight, high-impact resistant applications, such as for ballistic panel. Meanwhile, the 316 grade composites, with their enhanced resistance to crack propagation, are well-suited for scenarios where durability and fracture toughness are essential. These findings provide a valuable foundation for the design and selection of materials in safety-critical applications, where energy absorption and damage tolerance are of paramount importance.

#### ACKNOWLEDGEMENT

This research was supported by the Collaborative Research Grant (CRG) (vot K036). We are grateful to Universiti Tun Hussein Onn Malaysia (UTHM) for providing the facilities to conduct this research.

#### REFERENCES

- Alev, K. I., Kaman, M. O., Albayrak, M. & Yanen, C. (2023). Investigation of the mechanical response of laminated composites reinforced with different type wire mesh. *J. Brazilian Soc. Mech. Sci. Eng.*, **45**: 1–15.
- Arulmurugan, M., Sankaranarayanan, G., Rajendran, S., Paramaguru, T. & Sakthivel, K. (2023). Effect of Glass / Kevlar Fibre / Aluminium 2200 Wire Mesh. *Reinf. Compos.*, **19**: 1098–1113.
- Asavavisithchai, S., Marlaiwong, T. & Nuttayasakul, N. (2018). Development of composite armors

- using natural rubber reinforced with steel wire mesh for ballistic resistance. *IOP Conf. Ser. Mater. Sci. Eng.*, **409**: 012001.
- Bulut, M. & Erklığ, A. (2018). The investigation of quasi-static indentation effect on laminated hybrid composite plates. *Mech. Mater.*, **117**: 225–234.
- Dow Chemical Company (2009). *D.E.R.<sup>TM</sup> 332 Liquid Epoxy Resin*. Dow Chemical Company, Michigan, US
- Elumalai, P.V., Dhineshababu, N.R., Varsala, P., Anjani Devi, S., Sitaramamurthy, A.S.S.M., Saleel, C.A. & Hasan, N. (2022). Effects of asna fibre reinforced with epoxy resin with and without steel wire mesh and simulation of car bumper. *Mater. Res. Express*, **9**: 055301.
- Feng, N.L., Malingam, S.D., Subramaniam, K., Selamat, M.Z. & Juan, W.X. (2020). The investigation of the tensile and quasi-static indentation properties of pineapple leaf / kevlar fibre reinforced hybrid composites. *Defence S&T Tech. Bull.*, **13**: 117–129.
- Fernandes, A.J.G., de Amorim Junior, W.F., Filho, W.B., Guedes, I.P., Silva, A.L. & Porto, W.L. (2017). Behavior of fiberglass polymer composites under ballistic impact and quasi-static punch shear tests. *Mater. Sci. Forum*, **881 MSF**: 300–306.
- Krishnasamy, P., Rajamurugan, G. & Thirumurugan, M. (2021). Dynamic mechanical characteristics of jute fiber and 304 wire mesh reinforced epoxy composite. *J. Ind. Text.*, **51**: 540–558.
- Lu, G. & Yu, T. (2003). *Energy Absorption of Structures and Materials*. Elsevier, Amsterdam, Netherlands.
- Mahdad, M., Saada, A.A., Belaidi, I., Mokhtari, A. & Benidir, A. (2018). Damage modelling in thermoplastic laminates reinforced with steel and glass fibres under quasi-static indentation loading at low-velocity. *Adv. Compos. Lett.*, **27**: 251–260.
- Malingam, S.D., Feng, N.L., Sean, N.C., Subramaniam, K., Razali, N. & Mustafa, Z. (2018). Mechanical properties of hybrid kenaf / Kevlar fibre reinforced thermoplastic composites. *Defence S&T Tech. Bull.*, **11**: 209–224.
- Martins, C.M.B., Moreira, J.L. & Martins, J.I. (2014). Corrosion in water supply pipe stainless steel 304 and a supply line of helium in stainless steel 316. *Eng. Fail. Anal.*, **39**: 65–71.
- McCarthy, N. (2020). *Infographic: Plastic Can Take 500 Years To Bio-Degrade In The Ocean*. Available online at: <https://www.statista.com/chart/15905/the-estimated-number-of-years-for-selected-items-to-bio-degrade> (Last access date: 20 February 2024).
- Nik Ismail, N.A., Nazrul Roslan, M., Ismail, A.E. & Yazid Yahaya, M. (2023). Influence of reinforcement stacking sequence and mesh size on the tensile performance of novel hybrid bamboo fiber/aluminium mesh reinforced polymer composites. *Mater. Today Proc.*, 2023.03.315.
- Pach, J. & Kuterek, E. (2021). Investigation of the quasi-static penetration resistance behaviour of carbon/aramid fibre-reinforced pp laminate. *Mater.*, **14**: 709.
- Rashid, A.H.A., Mohamad, S.N.H., Nasir, K., Shaari, M.F., Roslan, M.N., Marsi, N., Nasir, S.H., Esa, M.F. & Mahmood, S. (2019). Puncture impact performance of coir-aramid/epoxy hybrid composite: Effects of stacking configurations. *Int. J. Mech. Eng. Robot. Res.*, **8**: 368–373.
- Sakthivel, M. & Vijayakumar, S. (2017). Influence of stainless-steel wire mesh on the mechanical behaviour in a glass-fibre-reinforced epoxy composite. *J. Mater. Technol.*, **51**: 455–461.
- Sutherland, L.S. & Guedes Soares, C. (2012). The use of quasi-static testing to obtain the low-velocity impact damage resistance of marine GRP laminates. *Compos. Part B Eng.*, **43**: 1459–1467.
- Wagih, A., Maimí, P., Blanco, N. & Costa, J. (2016). A quasi-static indentation test to elucidate the sequence of damage events in low velocity impacts on composite laminates. *Compos. Part A Appl. Sci. Manuf.*, **82**: 180–189.
- Wang, C., Wang, H., Shankar, K. & Hazell, P. J. (2022). Dynamic failure behavior of steel wire mesh subjected to medium velocity impact: Experiments and simulations. *Int. J. Mech. Sci.*, **216**: 106991.
- Wang, C., Wang, H., Shankar, K., Morozov, E.V. & Hazell, P.J. (2021). On the mechanical behaviour of steel wire mesh subjected to low-velocity impact. *Thin-Walled Struct.*, **159**: 107281.
- Yahaya, R., Sapuan, S. M., Jawaid, M., Leman, Z. & Zainudin, E. S. (2014). Quasi-static penetration and ballistic properties of kenaf-aramid hybrid composites. *Mater. Des.*, **63**: 775–782.
- Zhao, Q., Xiao, X., Ge, R., Zhang, Y., Chen, X. & Jia, B. (2023). Experimental-numerical study on ballistic impact behavior of 316L austenitic stainless steel plates against blunt and ogival projectiles. *Int. J. Hydrogen Energy*, **48**: 8526–8548.

# MANPACK GROUND SURVEILLANCE RADAR AS SUPPORTING EQUIPMENT FOR THE INDOONESIAN ARMY

Yussi Perdana Saputera<sup>1,2,3\*</sup>, Moh. Khusaini<sup>1</sup>, Dhiana Puspitawati<sup>1</sup> & Arif Harnanto<sup>4</sup>

<sup>1</sup>Doctoral Program Graduate School, Brawijaya University, Indonesia

<sup>2</sup>Faculty of Electrical Engineering, Telkom University, Indonesia

<sup>3</sup>Indonesian Defence Industry (PT.RTI), Indonesia

<sup>4</sup>Ministry of Defence of the Republic of Indonesia, Indonesia

\*Email: yussips@telkomuniversity.ac.id

## ABSTRACT

In this research, a manpack radar is designed using frequency modulated continuous wave (FMCW) technology. The signal is continuously transmitted by separate antennas with microstrip array antenna technology for the transmitter and receiver. The use of new technology allows the manpack radar to detect targets using low transmit power ( $\leq 10$  W) so that it can operate on batteries. With dimensions of 520 mm (W) x 410 mm (H) x 108 mm (D) and weighing only 15.9 kg, this radar can be easily carried by personnel for maneuvering in the field. Although the dimensions of this manpack radar system are small, it has high detection capability, whereby it can detect drones, humans, small vehicles and large vehicles at ranges of up to 2, 3, and 5 km respectively. In addition, this radar system not only detects targets horizontally, but also vertically so that it can calculate the height of the target. It can also track multiple targets simultaneously and display the parameters of each target, such as distance, speed and altitude. With these aspects, this radar system design is effective for use by Indonesian National Armed Forces (TNI) personnel in the field to conduct surveillance for supporting combat operations.

**Keywords:** *Manpack radar; surveillance; frequency modulated continuous wave (FMCW); radar cross section (RCS); low transmit power.*

## 1. INTRODUCTION

A study conducted by *Badan Pusat Statistik* (BPS) showed that Indonesia is the largest archipelago state with more than 17,000 islands (BPS, 2022). Based on this, Indonesia needs radar devices that can monitor land and water areas throughout the archipelago, which can be used in remote places with difficult access. With the geographical conditions of Indonesia that has a very large land and sea areas, coupled with the limited number of permanent radars owned, portable radar systems, hereafter referred to as manpack radar, are needed that can be installed temporarily in certain areas to be able to conduct mobile surveillance.

A radar system was developed in a previous work (PT. RTI, 2022), but with larger size and could only be mounted on vehicles or towers. Even though the range of its detection is large, its weight is almost 50 kg and the length of the antenna reaches about 1 m. Therefore, it cannot be packed into a smaller mechanical frame, thereby losing its flexibility to be carried freely and is not “manpack” size.

This study is aimed at developing a manpack ground surveillance radar that can be mobile operated with easy and fast preparation. This radar can be used for border and battlefield surveillance as well as for security of military and civilian facilities. For easy portability, the radar is designed to be small and lightweight so that it can be carried on the back. Its dimensions are less than 50 cm and weighs only 15.9 kg, so that it can be easily carried individually when changing places of use. This manpack radar research is an effort to improve operational and supervisory capabilities in protecting the territory of the Republic of Indonesia by the Indonesian National Armed Forces (TNI).

In this research, improvements will be made to the radio frequency (RF) section, with the addition of a radar dome, so that it is not affected by weather. In addition, digital signal processing (DSP) and display software will also be developed. The manpack radar is used to detect moving targets on the ground such as people, vehicles and low-flying aircraft. This radar is designed using frequency modulated continuous wave (FMCW) technology, which is a radar technology that emits signals continuously and uses two separate antennas for the transmitter and receiver. The FMCW technology allows for long-range radar detection with very low power consumption (10 watts or less) (Anantoep, 2011). With this low power consumption, the radar can be operated using batteries. This radar system is designed so that preparation for radar operations can be done easily in less time. It is divided into several large separate parts, namely the antenna system, radio frequency (RF) and intermediate frequency (IF) components, digital data processor, as well as radar display and control (PT. RTI, 2020). For field use, a tripod is used as a radar support that can be adjusted in height as needed. In addition, this radar system is designed to meet environmental protection standards such as ingress protection (IP) level 65 against particles, dust and water, as well as against mechanical resistance.

## 2. RADAR MANPACK GROUND SURVEILLANCE SYSTEM DESIGN

In this research, the design of the manpack ground surveillance radar system consists of antenna, RF and IF, control, power supply, and mechanical systems, as well as signal processing and display software and (Figure 1).

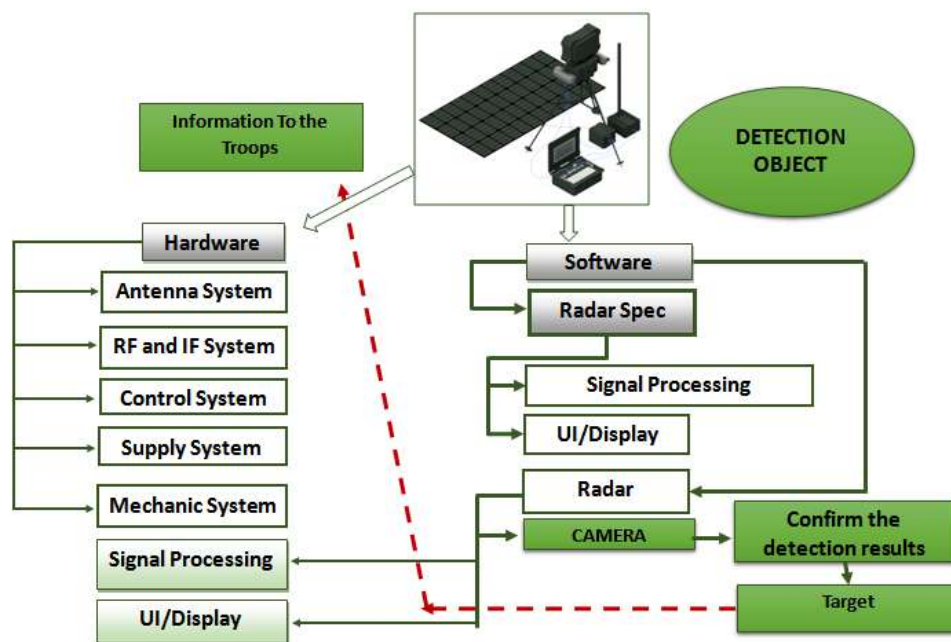


Figure 1: Radar system design.

### 2.1 Antenna System

Antenna is one of the most important parts in a radar. It converts electrical quantities from the transmission line into electromagnetic (EM) waves to be emitted into the air. In addition, it can also capture EM waves from the free air to be converted back into electricity through the transmission line. In other words, an antenna is a device that converts guided waves from a transmission line into free waves in the air and vice versa (Lighthart, 2011). Each antenna has characteristics that relate to each other. These characteristics include antenna cross-sectional area (aperture), bandwidth, antenna radiation pattern, gain, efficiency and polarity (Kraus & Marhefka, 2001).

The antenna is designed in the form of a rectangular microstrip antenna with a uniform array rationing technique with a target gain of 25 dB with horizontal polarization using Roger Duroid 4003 material that has permittivity value of 3.8 (Figure 2).

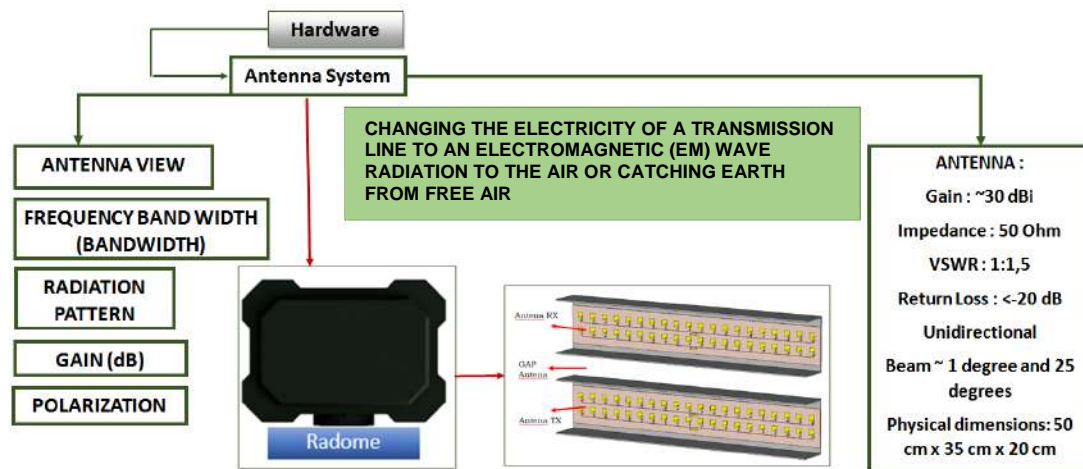


Figure 2: Antenna system design.

## 2.2 RF and IF System

The RF system is a component that can detect EM wave signals that are processed by the radar system for both the transmitter and receiver, where the transmitter emits EM wave signals that are generated by the dielectric resonator oscillator (DRO) and amplified by the power amplifier and forwarded to the antenna, and vice versa for the received signal that is obtained from the reflection of objects detected (Mashury *et al.*, 2013). EM waves that enter the antenna are processed into guided waves and forwarded to the antenna section and continue to the low noise amplifier (LNA) and RF components to make it into a baseband signal, or into an IF signal. This IF signal is an RF signal that has been down-converted into a baseband signal and the up-converted into a RF signal. The LF signal will be processed by the signal processing section to be converted into a digital signal. The EM wave signal emitted through the antenna has an amplitude, frequency and interval, and has properties that can change at any time to present information. The design of the RF and IF system is shown in Figure 3.

## 2.3 Control System

The control system is the part that serves to control the movement of the radar, sensors and radar automation process when it is turned on for both for electrical automation and data connectivity. As mentioned in control system design (Figure 4), the hardware consists of antenna, RF and IF, and control systems that is integrated to control radar movements, sensors and radar automation process.

## 2.4 Power Supply System

The power supply system (Figure 5) is the power source system for the radar, which is used from an alternating current (AC) power source that can be obtained from a generator or power line. The AC power source will be passed to the uninterruptible power supply (UPS), and then to the radar hardware and radar console. For field use, solar panels are used as a power source that will be connected to a battery or UPS.

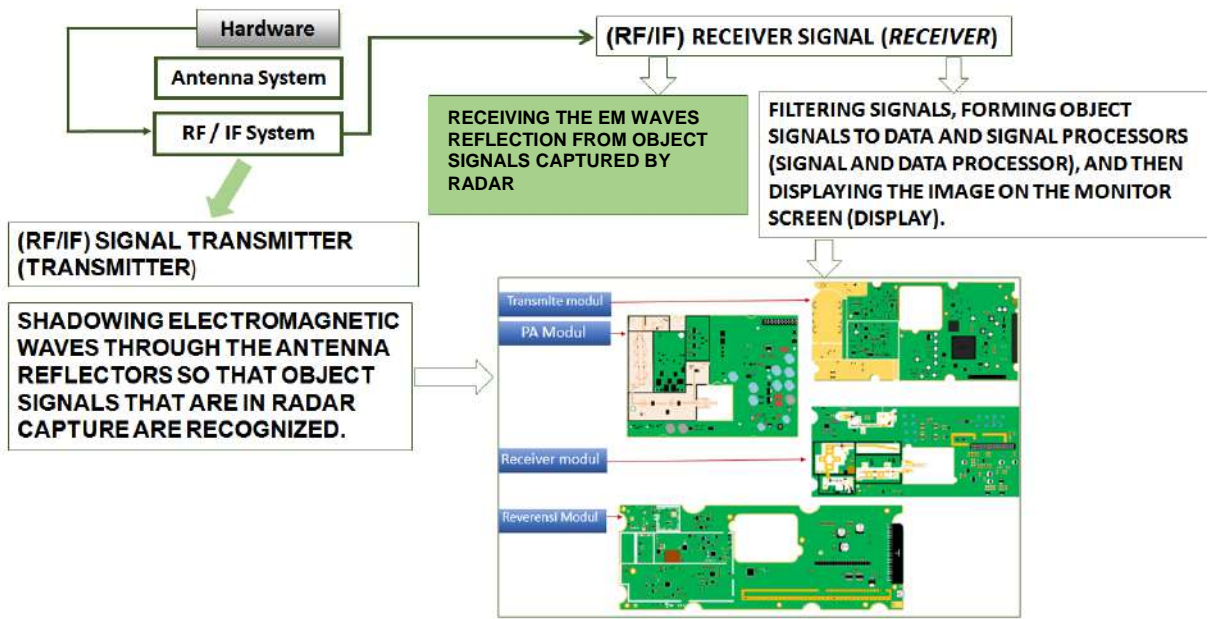


Figure 3: RF and IF system design.

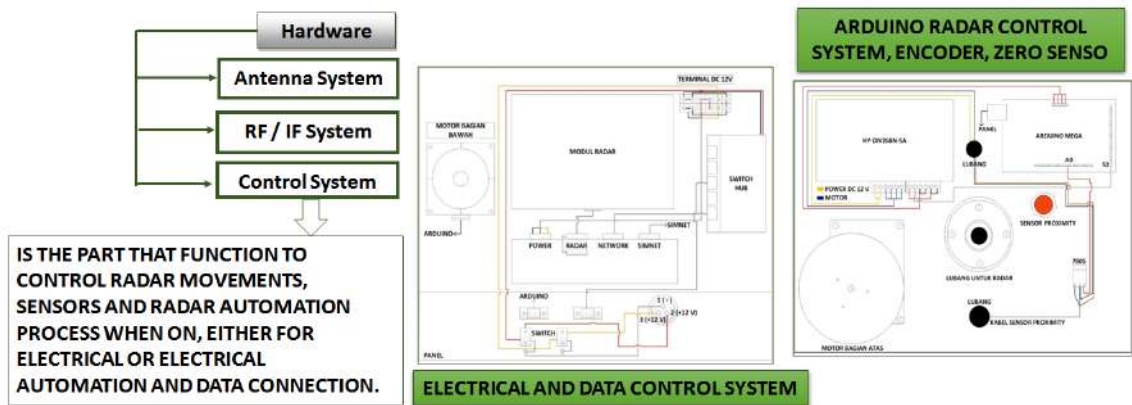


Figure 4: Control system design.

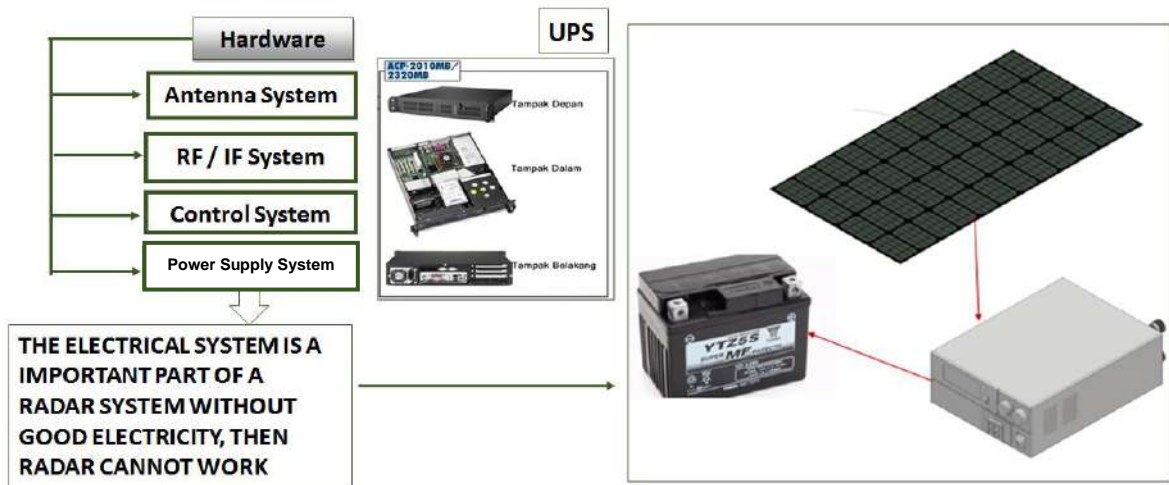


Figure 5: Power supply system design.

## 2.5 Mechanical System

The mechanical system is the mechanical frame of the radar as a whole for the antenna, RF and IF, control, and power supply systems, as well as motors and consoles. In the mechanical system design (Figure 6), the hardware consists of the systems that are integrated into one packed mechanical frame that can be mounted on top of a customized tripod. On the right and left side of the mechanical frame is a slot for the thermal and long-range cameras so that all of the supporting devices can be installed in one tripod.



Figure 6: Mechanical system design.

## 2.6 Software

The radar display system (Figure 7) is part of the radar signal processing system that is used to produce a radar display (Figure 8) whose information can be understood by the user. This software consists of two pieces of software, namely user interface software installed on the main computer and data processing software located on the pedestal ground surveillance radar section. This display is a type of plan position indicator (PPI) display that is commonly used on radar displays. In this display, there is a circle in the middle of the screen that has corner numbers written on the edge and in the center of the circle, there is a line from the center of the circle to the edge of the circle. The line in the middle of this circle will rotate according to the direction, speed and angle of rotation of the radar antenna drive motor. The object display on the screen shows the position of the object to the location of the monitoring radar. Some information related to the object will be displayed on the right side of the screen.

In the software system design, there is software that change analog signals into digital data that is processed with signal processing so it can be displayed on radar display by developing the user interface to be human readable. Further action after reading the radar display is to check the target with the camera where the display software is already integrated in the console display so that the target detection can be verified by through human vision, whether it is a real target or just false detection. This shows that the radar system and camera complement each other.



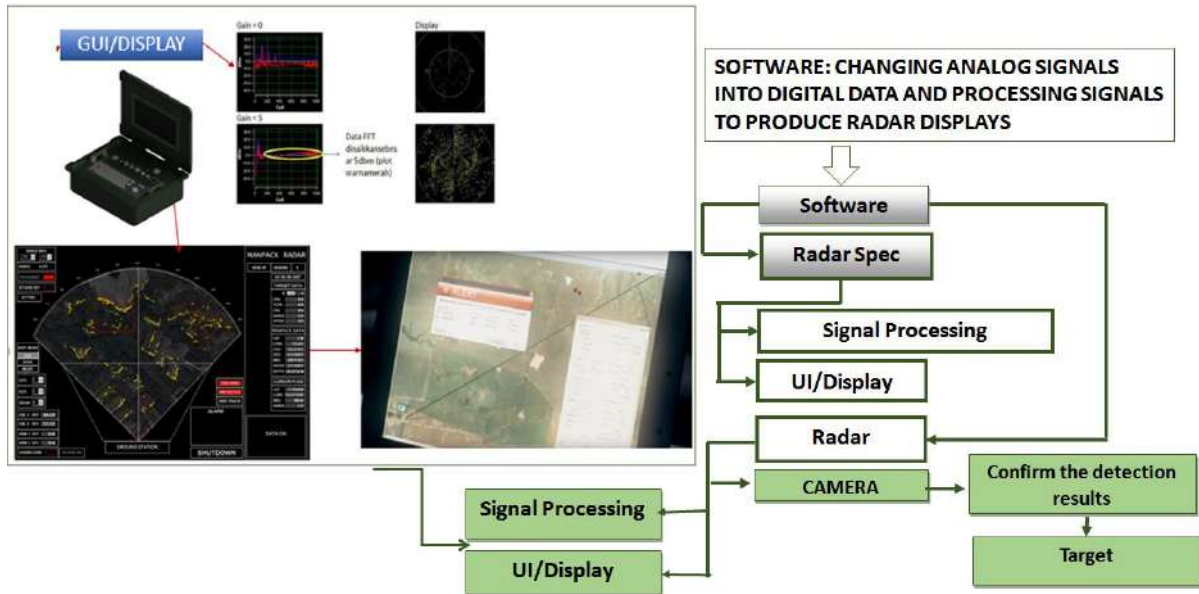


Figure 7: Software system design.

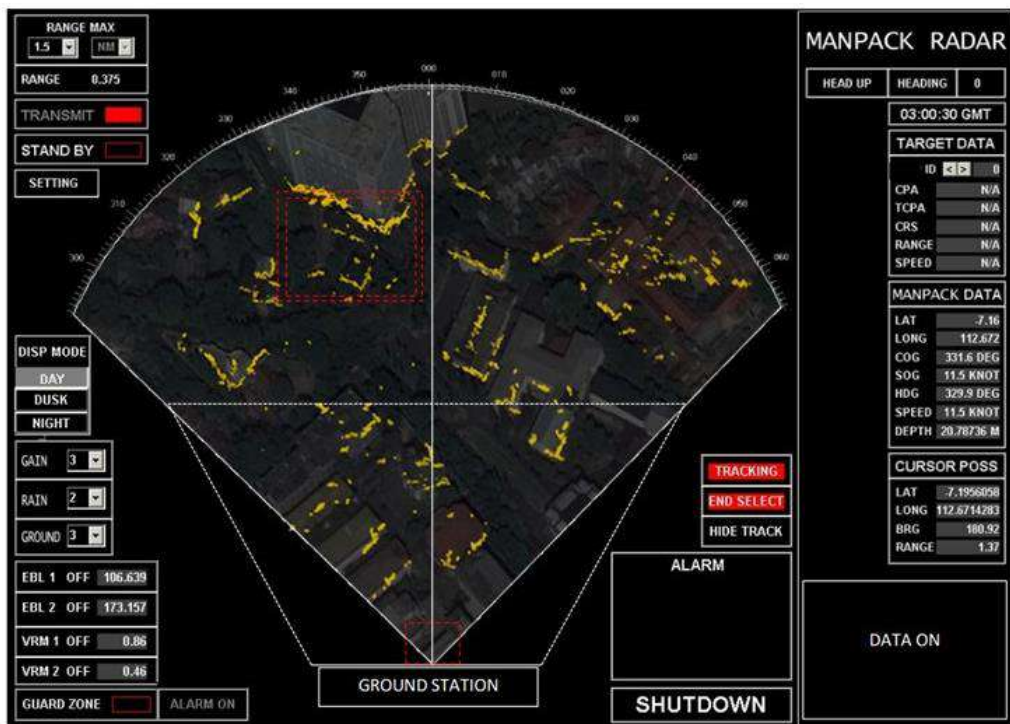


Figure 8: Radar display of the manpack radar.

## 2.7 Digital Signal Processing (DSP) Unit

The DSP unit functions to process the input signal in order to obtain the desired information and functions to process ADC (analog-to-digital signal) data and DDS (direct digital synthesis) signals (Mashury *et al.*, 2015). In general, the signal processing section consists of:

- ADC IO (analog-to-digital signal input / output) handling
- DDS signal generator

- Signal level calculation
- Signal filter
- Compiling the data packet

All signal processing on the computer part is handled by the SNAP application, which is a Visual C++ based signal processing program for radar applications that performs several main functions, namely:

- Raw data capture
- Fast Fourier transform (FFT) processing
- Constant false alarm rate (CFAR) processing
- Data compression

### 3. RESULTS AND DISCUSSION

The developed manpack ground surveillance radar (Figure 9) has specifications as shown in Table 1. The radar system, with dimensions of 520 mm (W) x 410 mm (H) x 108 mm (D) and weight of 15.9 kg, is mounted on a tripod equipped with thermal and long range cameras, with each of those devices connected to a power source (power supply and electrical converter) with a power cable and connected to the display console with an ethernet cable. The power supply can be charged simultaneously while used as a power source. The radar system is also installed with a radio link for serving remote radar data that is processed and displayed on the display console.

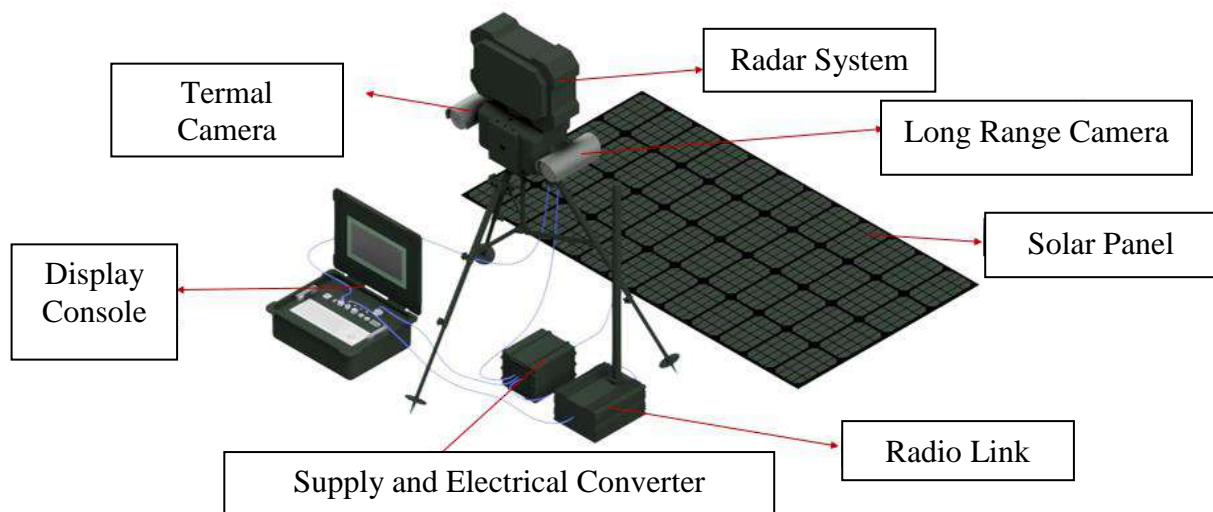


**Figure 9: The ground surveillance manpack radar.**

**Table 1: Specifications of the developed manpack radar system.**

Antenna		
a.	Microstrip Patch Array Gain	~20 dB
b.	Dual Antenna Configuration for Transmitter and Receiver	Yes
c.	Elevation Range	Up to 40°
d.	Beamwidth	< 5°
e.	Vertical Beamwidth	< 25°
f.	Detection Angle	90 and 180°
g.	Speed of Movement	5, 10, 15, 20

<b>Transmitter</b>		
a.	Frequency	X-band
b.	Range (5, 2.5, 1, 0.5)	Yes
c.	Output Power 10 W (Max)	Yes
d.	Bandwidth	60 MHz
e.	Power	1 W
<b>Receiver</b>		
a.	IF Bandwidth	512 kHz
b.	Number of Range Cells	512
c.	Range Cells 125, 62, 31, 12, 6 M	Yes
d.	PC-Based Processing System	Yes
e.	Laptop Display Size	Yes
f.	Maximal Beat Frequency	2 MHz
g.	Beat Signal Sampling by 16-bit ADC	Yes
<b>Frequency Generation</b>		
a.	Main Frequency Generator DRO	Yes
b.	FM – Modulation	Yes
c.	Linear Saw-tooth by Using DDS (Direct Digital Synthesizer)	Yes
d.	Sweep (Sweep Repetition Frequency)	1.5 kHz
e.	Frequency Sweep (2, 4, 8, 16, 32) MHz	Yes
<b>Software</b>		
a.	Target Tracking	Yes
b.	Able to be Integrated into a Telecommunication Network	Yes
c.	Mode (Night, Dusk, and Day)	Yes
<b>Technical</b>		
a.	Power Max	24 V DC
b.	Consumption Power	100 W (Max)
c.	Size Dimension (W x H x D)	520 x 410 x 108 mm
d.	Weight	15.9 kg
<b>Object Detection</b>		
a.	Drone (RCS = 0.2 m <sup>2</sup> )	Tracking: 500 m Detection: 2,000 m
b.	People (RCS = 1 m <sup>2</sup> )	Tracking: 2,000 m Detection: 3,000 m
c.	Small Vehicles (RCS = 100 m <sup>2</sup> )	Tracking: 3,000 m Detection: 4,000 m
d.	Large Vehicles (RCS = 200 m <sup>2</sup> )	Tracking: 4,000 m Detection: 5,000 m

The testing process in the field was carried out in the Glora Bandung Lautan Api (GLBA) area (Figure 10). It was carried out by detecting people as well as passing vehicles, according to the requirements of the origin of the system. The radar system can be used to detect objects that will be shown on the display, while tracking can be carried out if the object is found to be moving so that it can detect the object's trail and its velocity that is calculated by the software automatically.

It is found that the radar is capable of tracking drones moving up to 500 m and detecting it at range of up to 2 km; tracking humans walking up to 2 km and detecting it at range of up to 3 km; tracking small vehicles moving up to 3 km and detecting it at range of up to 4 km; and tracking large vehicles moving up to 4 km and detecting it at range of up to 5 km, with note that this test is a result of line of sight (LOS) detection to get the optimal data. For the parameters, the radar system can analyze the signal data to get value of distance, velocity and radar cross section (RCS) of the object. Using the software display with maps, it can be processed to get the geolocation of the object with calculation based of the radar's installed location. All of the objects can be seen and tracked in one single layer and have the output of each own's parameters.

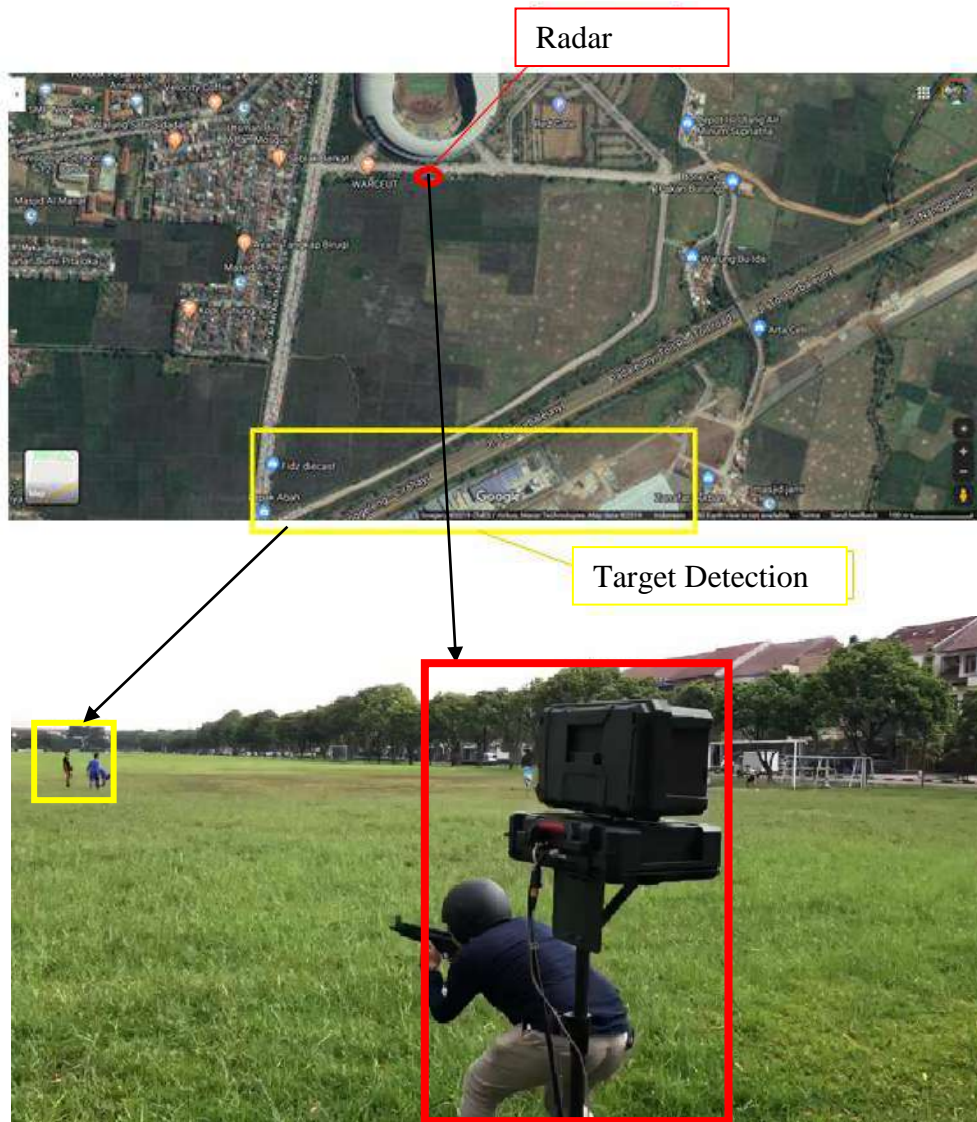


**Figure 10: Testing process of the manpack radar.**

#### **4. CONCLUSION**

A manpack ground surveillance radar is developed using FMCW and microstrip array antenna technologies. The fabrication process is carried out starting from the design, simulation and fabrication stages, both for antenna, and its RF and IF components, with supporting components inside a mechanical frame that can be connected to a laptop with signal processing and display software. This radar system can be carried by troops (one to two personnel), is easy to be used with a laptop as a display, uses very little power (customized maximum power output of 100 W), as well as easy to maintain. It can be used to detect objects when troops are in the field at range of up to 2 km for drones, 3 km for humans, 4 km for small vehicles and 5 km for large vehicles. It also tracks moving objects at range of up to 500 m for drones, 2 km for humans, 3 km for small vehicles and 4 km for large vehicle. This radar can replace the limited human vision of troops and is useful during night operations as it can function properly in all weather conditions.

## REFERENCES

- Anantoep (2011). *Radar FM-CW*. Available Online at <https://anantoep.wordpress.com/2011/07/04/mengenal-radar-part-3-radar-fmcw> (Last access date: 1 oct 2023).
- BPS (Badan Pusat Statistik) (2022). *Luas Daerah dan Jumlah Pulau Menurut Provinsi*. Available online at: [https://www.bps.go.id/indikator/indikator/view\\_data\\_pub/0000/api\\_pub/UFpWMmJZOVZIZTJnc1pXaHhDV1hPQT09/da\\_01/1](https://www.bps.go.id/indikator/indikator/view_data_pub/0000/api_pub/UFpWMmJZOVZIZTJnc1pXaHhDV1hPQT09/da_01/1) (Last access date: 05 November 2022).
- Kraus, J.D. & Marhefka, R.J. (2001). *Antennas for All Applications*, McGraw Hill, New York, US.
- Ligthart, L.P. (2011). *Short Course Document on Radar Technologies*. International Research Centre for Electronics and Telecommunication, Bandung, Indonesia
- Mashury, W., Yussi P.S. & Yuyu, W. (2015). *Development of phase inverter for performance improvement of FM-CW radar*. IEEE Region 10 Conf. (TENCON 2015), 1-4 November 2015, Macao, China.
- Mashury, W., Yussi P.S. & Yuyu W (2013). Research and development of transportable coastal radar at S-band frequency with FM-CW technology for supporting C4ISR. *3<sup>rd</sup> Int. Conf. Elect. Electr. (EEIC 2013)*, 24-25 December 2013, Hong Kong, China.
- PT. Radar Telekomunikasi Indonesia (2022). *Naskah Akhir Litbang Prototipe Man Portable Surveillance Radar Tahap I TA.2022*. Ministry of Defense, Indonesia.

# SHORTEST POSSIBLE DUAL-SECTION MATCHING NETWORK

Chung Boon Kuan

Department of Electrical and Electronic Engineering, Universiti Tunku Abdul Rahman,  
Malaysia

Email: chungbk@utar.edu.my

## ABSTRACT

*Impedance matching networks using lumped inductors and capacitors are only applicable at lower radio frequencies (RF). At high microwave frequencies, transmission lines should be used in matching network design, but the required substrate area may be too large. This paper presents a dual-section matching network design method that uses the shortest possible transmission lines. It is particularly advantageous for radio frequency integrated circuit (RFIC) design. Both single- and dual-section solutions are presented with detailed equations and design methodologies. The methods are flexible enough to accommodate the modification of the line width to an attainable value, with a trade-off of a slight increase in the overall transmission line length. The Q-factor and bandwidth can be adjusted to suit different application needs by modifying the line width and length. A few design examples are presented herein.*

**Keywords:** *Transmission line theory; impedance matching; circuit analysis; microwave amplifiers; antenna*

## 1. INTRODUCTION

In the past decade, wireless networked intelligence has spread throughout our cities, homes and offices. In Industry 4.0, factory floors use wireless networks to improve production through advancements in connectivity and digitisation to allow manufacturing systems to become smarter and more autonomous. Wireless communications enabled by radio frequency integrated circuits (RFIC) and monolithic microwave integrated circuits (MMIC) are widely used in domestic and military defence applications.

In the design of RFIC and MMIC, impedance matching is essential for achieving minimum reflection and adequate harmonic rejection. The simplest matching networks involve the use of lumped inductors and capacitors (de Lima *et al.*, 2000; Thompson & Fidler, 2004; Chung, 2006; Hameed & Moez, 2017). However, the lack of a good inductor and capacitor is one of the shortcomings of standard integrated circuit (IC) processes. The attainable inductance values and relatively low Q-factors are the two main problems faced by design engineers (Pozar, 2012). Lumped inductance higher than 10 nH is difficult to achieve due to parasitic capacitance. On the other hand, high-Q capacitors tend to have relatively loose tolerance, while area-efficient capacitor structures usually have low Q and poor voltage coefficients. In addition, parallel / series resonances caused by parasitic elements limit the upper operating frequency of the inductors / capacitors. At higher microwave frequencies, microstrip transmission lines and stub lines should be applied in single- or double-stub impedance matching networks (Chung, 2023). However, this increases the required semiconductor substrate area. An alternative is to use microstrip transmission lines as phase shifters (Chung, 2022).

A quarterwave transformer microstrip section can be used in certain impedance matching problems. The bandwidth is limited because the microstrip length is a quarter wavelength ( $\lambda/4$ ) only at the centre frequency. In order to increase the bandwidth, multiple sections of quarterwave transformers can be used (Schwartz & Allen, 2004; Pozar, 2012), as illustrated in Figure 1. The idea is to spread the needed impedance transformation ratio over a few step-changes provided by separate quarterwave transformers. One major shortcoming is the great increase in overall transmission line length and the required substrate area. Furthermore, quarterwave transformers can only be used to transform a real impedance to another real impedance. That means the method is not suitable when the load or source impedance is a complex value.

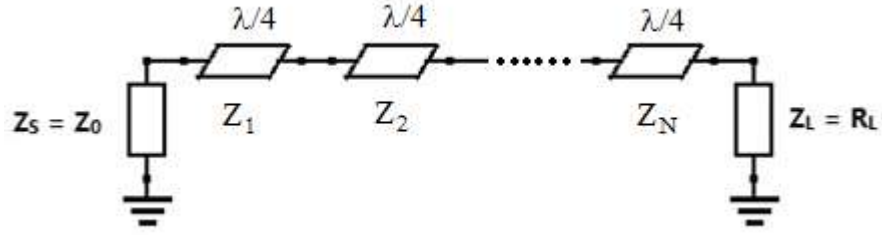


Figure 1: Multisection matching transformer (Pozar, 2012).

This paper proposes a method that uses a transmission line to transform a complex impedance to a real impedance using the shortest possible transmission lines (i.e., less than a quarter wavelength), thus enabling significant reduction of RFIC chip size. The equations and design methodologies are presented. The line width can be modified to an attainable value, with a trade-off in a slight increase of the overall transmission line length. Further modification of the line width and length can be done to optimise the Q-factor and bandwidth to suit different application needs. A few design examples are presented. The use of transmission lines instead of discrete inductors / capacitors means this method can be used at high microwave frequencies. This is a new application of transmission line theory to solve impedance mismatch problems.

## 2. SINGLE-SECTION COMPLEX IMPEDANCE TRANSFORMER

Consider a transmission line of characteristic impedance  $Z_C$ , phase constant  $\beta$  and length  $l$  terminated by a complex load impedance  $Z_L = R_L + jX_L$ . At the source end of the transmission line, the input impedance  $Z_{in}$  is given by Equation 1.

$$Z_{in} = Z_C \left[ \frac{Z_L + jZ_C \tan \beta l}{Z_C + jZ_L \tan \beta l} \right] = R_{in} + jX_{in} \quad (1)$$

$$\rho_{in} = \frac{Z_{in} - Z_0}{Z_{in} + Z_0} \quad (2)$$

Equation 2 gives the reflection coefficient  $\rho_{in}$  for a given reference impedance  $Z_0$ . If  $Z_C = Z_0$ , increasing electrical length  $\theta = \beta l$  from 0 to  $180^\circ$  causes  $\rho_{in}$  to change along a concentric circle at the centre of the Smith Chart according to Equation 3, starting from the load reflection coefficient  $\rho_L$ . This is known as a voltage standing wave ratio (VSWR) circle.

$$\rho_{in} = \frac{Z_{in} - Z_0}{Z_{in} + Z_0} = \frac{Z_L - Z_0}{Z_L + Z_0} e^{-j2\beta l} = \rho_L e^{-j2\beta l} \quad (3)$$

If  $Z_C \neq Z_0$ , the VSWR circle will not be concentric but offset to the left or right as shown in Figure 2.

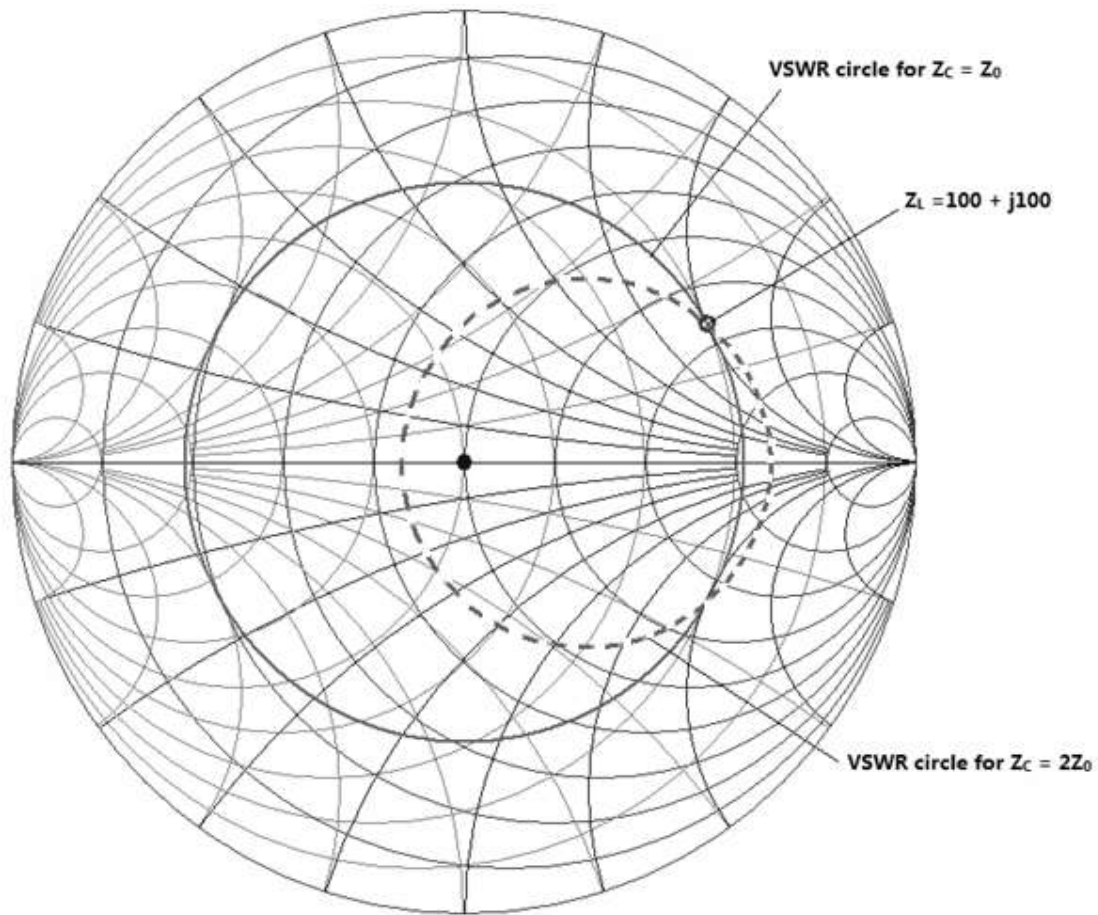


**Figure 2: Different VSWR circles for  $Z_C = Z_0$  as compared to  $Z_C = 2Z_0$ .**

The VSWR circle will cross the centre of the Smith Chart if a suitable value of  $Z_C$  is chosen. That means one can transform  $Z_L$  to  $Z_0$  using a suitable length of transmission line. When another value of  $Z_C$  is used, the complex load impedance can be transformed to another complex impedance. One can set  $R_{in} = 50 \Omega$  and  $X_{in} = 0$  in Equation 1 if  $Z_L$  is to be transformed to  $Z_0 = 50 \Omega$ . The required value of  $Z_C$  and electrical length  $\theta$  can be calculated using Equations 4 and 5 respectively.

$$Z_C = \sqrt{\frac{R_{in}X_L^2}{R_L - R_{in}} + R_{in}R_L} \quad (4)$$

$$\tan \theta = \frac{Z_C(R_{in} - R_L)}{R_{in}X_L} \quad (5)$$

As an example, consider the case where  $Z_L = 100 + j100 \Omega$ . The calculation gives a value of  $Z_C = 122.5 \Omega$  and  $\theta = 128.66^\circ$ . Another example is the case where  $Z_L = 100 - j100 \Omega$ . The calculation gives a value of  $Z_C = 122.5 \Omega$  and  $\theta = 51.34^\circ$ . These may not be the shortest possible transmission line lengths, as will be shown later. In the cases where  $R_L < R_{in}$ , Equation 4 may possibly give an invalid value. In other words, this single-section transformer can only be used when the normalised load impedance  $Z_L/Z_0$  is within the unit resistance circle ( $r > 1$ ) or unit conductance circle ( $g > 1$ ), as indicated in Figure 3. Transforming a complex load impedance to certain complex impedances may not be possible in some cases. In order to overcome this limitation, a dual-section complex impedance transformer is introduced.



### 3. DUAL-SECTION COMPLEX IMPEDANCE TRANSFORMER

In the dual-section transformer, the first section of the transmission line will transform  $Z_L$  to an intermediate complex impedance  $Z_I$  such that it is within either the unit resistance circle or unit conductance circle. The single-section transformer described above can then transform  $Z_I$  to  $50 \Omega$ . In this case,  $Z_L$  can be any value on the Smith Chart, i.e., no limitation on the value of  $Z_L$ .

Figure 3 shows a Smith Chart that is divided into two regions. Different algorithms should be used to obtain the solutions with the shortest possible overall transmission line lengths. For Region I,  $Z_L = R_L + jX_L$  or  $Y_L = G_L + jB_L$  is first transformed to  $Z_I = R_I + jX_I$  or  $Y_I = G_I + jB_I$  such that  $G_I = G_L$  and  $R_I = 50 \Omega + 1\%$  (the additional 1% is to ensure  $Z_I$  is within the unit resistance circle).  $B_I$  and  $X_I$  are then given by Equations 6 and 7.

$$B_I = \sqrt{\frac{G_I}{Z_0} - G_I^2} \quad (6)$$

$$X_I = -\frac{B_I}{G_I^2 + B_I^2} \quad (7)$$

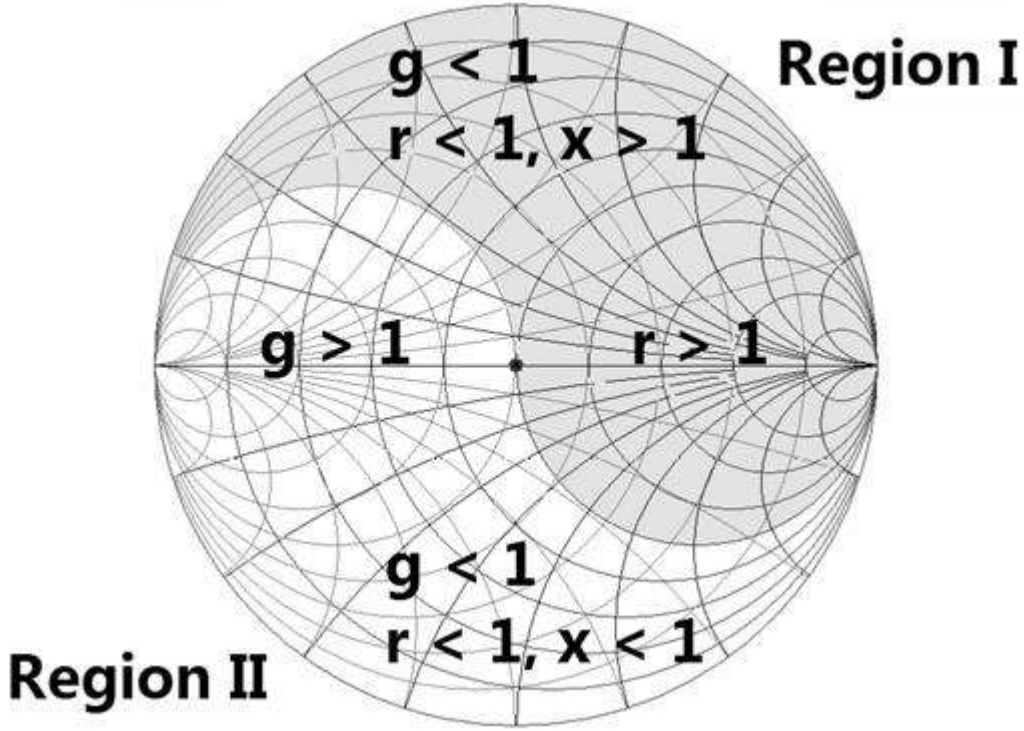


Figure 3: A Smith chart divided into two regions.

Figure 4 shows the circuit diagram of the dual-section complex impedance transformer.  $Z_{C1}$  and  $\theta_1$  are the characteristic impedance and electrical length of the first transmission line section respectively. Equation 1 is rewritten as follows:

$$Z_I = Z_{C1} \left[ \frac{Z_L + jZ_{C1} \tan \theta_1}{Z_{C1} + jZ_L \tan \theta_1} \right] = R_I + jX_I \quad (8)$$

Resolving Equation 8 yields:

$$Z_{C1}^2 = \frac{X_I - X_L}{R_I - R_L} (X_L R_I + X_I R_L) - X_I X_L + R_I R_L \quad (9)$$

$$\tan \theta_1 = \frac{Z_{C1}(R_I - R_L)}{X_L R_I + X_I R_L} \quad (10)$$

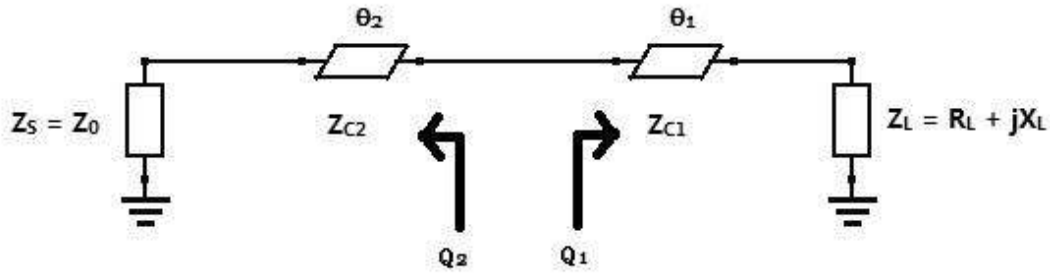


Figure 4: Circuit diagram of the dual-section complex impedance transformer.

For the second transmission line section, the characteristic impedance  $Z_{C2}$  and electrical length  $\theta_2$  can be determined using the design method of single-section complex impedance transformer, i.e., Equations 4 and 5 are rewritten as follows:

$$Z_{C2} = \sqrt{\frac{R_{in}X_L^2}{R_L - R_{in}} + R_{in}R_L} \quad (11)$$

$$\tan \theta_2 = \frac{Z_{C2}(R_{in} - R_L)}{R_{in}X_L} \quad (12)$$

Three design examples of single- and dual-section complex impedance transformers are tabulated in Table 1. The third example has no single-section solution because the load impedance is beyond the unit resistance circle. For the first and second examples, the dual-section solutions have overall transmission line lengths  $\theta_1 + \theta_2$  that are much shorter than the respective single-section solutions. However, the required characteristic impedance of 858.8  $\Omega$  may not be attainable in practical situations. This problem can be overcome by choosing a different value of  $Z_L$ , so long as it is within the unit resistance circle of the Smith Chart. There are a virtually unlimited number of alternative solutions. Attainable characteristic impedances can be chosen. Table 2 shows two additional solutions for each load impedance stated in Table 1. In each case, notice the increase in the overall transmission line length  $\theta_1 + \theta_2$ .

Table 1: Design examples of single- and dual-section impedance transformers.

$Z_L \Omega$	Single-section		Dual-section				
	$Z_C \Omega$	$\theta^\circ$	$Z_{C1} \Omega$	$\theta_1^\circ$	$Z_{C2} \Omega$	$\theta_2^\circ$	$\theta_1^\circ + \theta_2^\circ$
100+j100	122.5	128.66	20.05	15.73	858.8	5.72	21.45
100-j100	122.5	51.34	20.05	4.17	858.8	5.72	9.89
20.7+j50.3	NA	NA	7.08	10.71	690	5.72	16.43

**Table 2: Design examples of dual-section impedance transformers.**

$Z_L \Omega$	Dual-section							
	$Z_{C1} \Omega$	$\theta_1^\circ$	$Q_1$	$Z_{C2} \Omega$	$\theta_2^\circ$	$Q_2$	$\theta_1^\circ + \theta_2^\circ$	$Q_0$
100+j100	20.05	15.73	1.06	858.8	5.72	1.71	21.45	1.38
	15.5	10	1.03	146	40	2.04	50	1.53
	50	24	1.21	109	66	2.51	90	1.86
100-j100	20.05	4.17	1.73	858.8	5.72	0.01	9.89	0.87
	55.1	10	1.63	187	27	0.126	37	0.88
	187	30	1.56	63.8	70	0.96	100	1.26
20.7+j50.3	7.08	10.71	1.01	690	5.72	1.38	16.43	1.20
	19.8	28	1.10	169	26	1.53	54	1.32
	45.4	50	1.40	120	58	2.43	108	1.91

In order to further illustrate the validity of the proposed impedance matching method with the shortest possible transmission line, Figure 5 shows the results of a parametric analysis for  $Z_L = 100 + j100 \Omega$ . The shortest possible total length is  $21.45^\circ$  by selecting  $Z_{C1} = 20.05 \Omega$  and  $Z_{C2} = 858.8 \Omega$ . If  $Z_{C1}$  is increased (but  $\theta_1$  fixed at  $15.73^\circ$ ), the value of  $Z_{C2}$  can be decreased but the resulting solution yields a longer total length. Figure 6 shows the parametric analysis for the same complex impedance  $Z_L = 100 + j100 \Omega$  but with varying lengths of  $\theta_1$ . With fixed value of  $Z_{C1} = 20.05 \Omega$ , a shorter length of  $\theta_1$  can yield an impedance matching solution that reduces the value of  $Z_{C2}$  but with the trade-off of a longer total length.

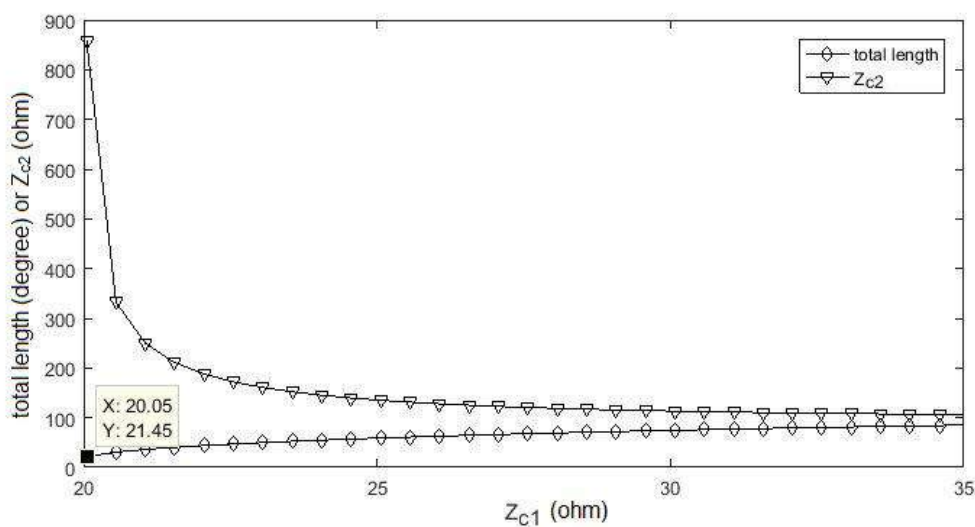


**Figure 5: Parametric analysis for increasing  $Z_{C1}$  to decrease  $Z_{C2}$ .**

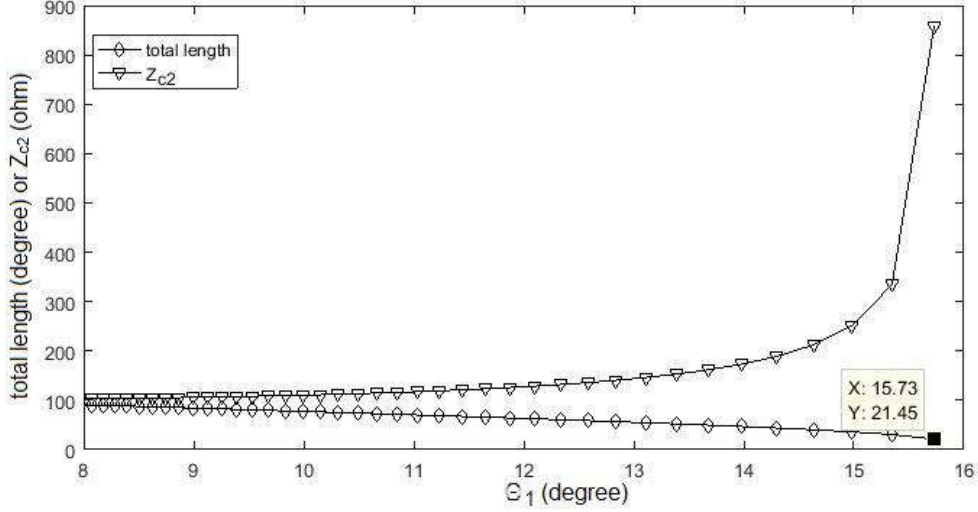


Figure 6: Parametric analysis for decreasing  $\theta_1$  to decrease  $Z_{C2}$ .

For Region II, the design method is similar but different sets of equations are used.  $Z_L = R_L + jX_L$  or  $Y_L = G_L + jB_L$  is first transformed to  $Z_I = R_I + jX_I$  or  $Y_I = G_I + jB_I$  such that  $R_I = R_L$  and  $G_I = 1/50 \text{ S} + 1\%$  (the additional 1% is to ensure  $G_I$  is within the unit conductance circle).  $X_I$  and  $B_I$  are then given by Equations 13 and 14.

$$X_I = \sqrt{R_I Z_0 - R_I^2} \quad (13)$$

$$B_I = -\frac{X_I}{R_I^2 + X_I^2} \quad (14)$$

The intermediate admittance  $Y_I$  is given by Equation 15.

$$Y_I = Y_{C1} \left[ \frac{Y_L + jY_{C1} \tan \theta_1}{Y_{C1} + jY_L \tan \theta_1} \right] = G_I + jB_I \quad (15)$$

Resolving Equation 15 yields:

$$Y_{C1}^2 = Z_{C1}^{-2} = \frac{B_I - B_L}{G_I - G_L} (B_L G_I + B_I G_L) - B_I B_L + G_I G_L \quad (16)$$

$$\tan \theta_1 = \frac{Y_{C1}(G_I - G_L)}{B_L G_I + B_I G_L} \quad (17)$$

For the second transmission line section, the characteristic impedance  $Z_{C2}$  and electrical length  $\theta_2$  can be determined using the design method of the single-section complex impedance transformer, i.e., Equations 11 and 12.

#### 4. Q-FACTOR IMPROVEMENT

The different solutions in Tables 1 and 2 result in different bandwidths or Q-factor. Since the complex impedance transformer line length is electrically short, the equivalent circuit in Figure 7 can be used to represent the circuit in Figure 4. Figure 7(a) is used if the load impedance is inductive. The Q-factor can be calculated using Equations 18 and 19 (Chung, 2006).

$$Q_1 = \frac{X_{C1} + X_L}{R_L} \quad (18)$$

$$Q_2 = \frac{X_{C2}}{Z_0} \quad (19)$$

Figure 7(b) is used if the load impedance is capacitive. The Q-factor can be calculated using equations (20) and (21):

$$Q_1 = \frac{B_{C1} + B_L}{G_L} \quad (20)$$

$$Q_2 = \frac{B_{C2}}{Y_0} \quad (21)$$

The overall Q-factor is given by Equations 22 or 23:

$$Q_0 = \frac{Q_1 + Q_2}{2} \text{ for double-section transformer} \quad (22)$$

$$Q_0 = \frac{Q_1}{2} \text{ for single-section transformer} \quad (23)$$

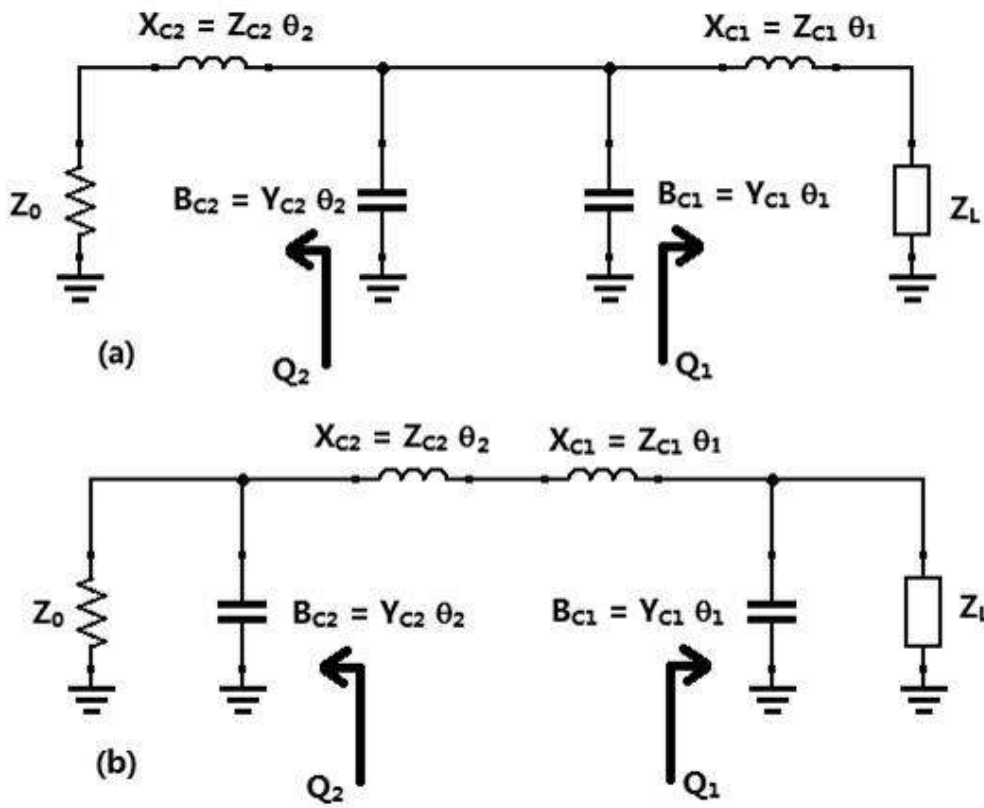
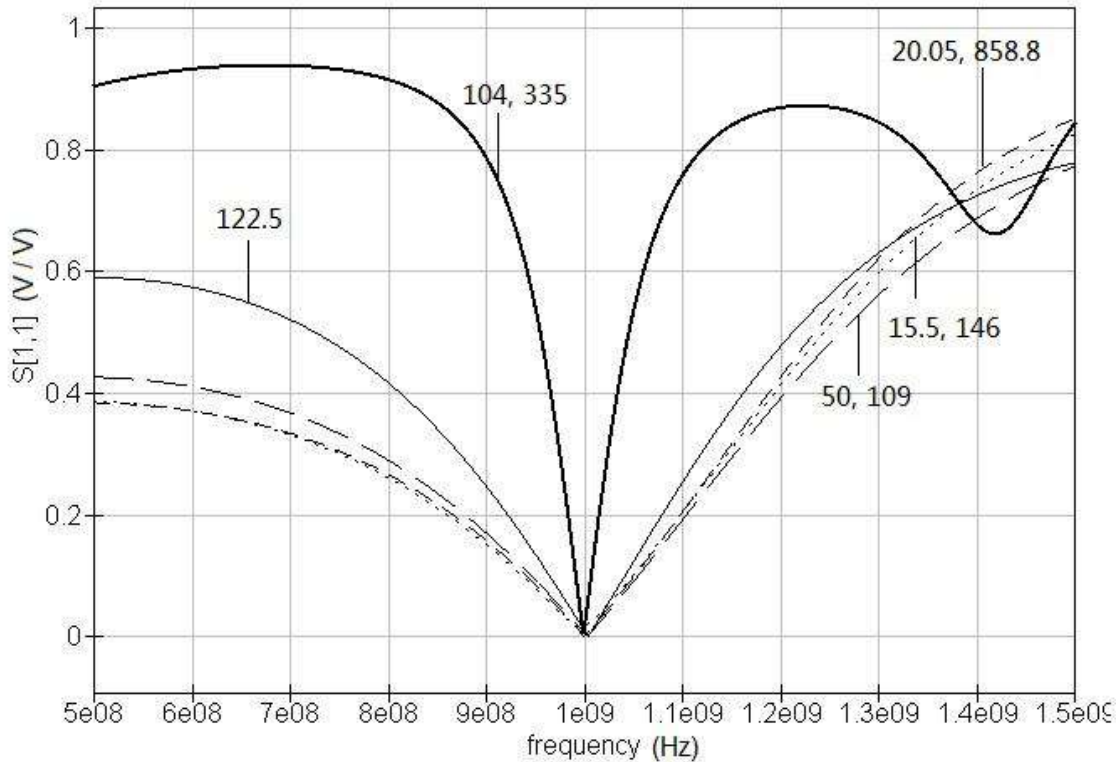


Figure 7: Equivalent circuits of dual-section impedance transformer for (a) inductive load and (b) capacitive load.

The Q-factors for the impedance transformers tabulated in Table 2 are calculated using the above equations. For the single-section solution to transform  $Z_L = 100 + j100 \Omega$  given in Table 1, its  $Q_0$  is 1.88. For illustration purposes, a dual-section impedance transformer with very high Q-factor is designed for  $Z_L = 100 + j100 \Omega$ . The first section has  $Z_{C1} = 104 \Omega$  and electrical length  $\theta_1 = 152^\circ$ . The second section has  $Z_{C2} = 335 \Omega$  and electrical length  $\theta_2 = 172^\circ$ . The value of  $Q_0$  is 11.94. The frequency responses of different solutions are plotted in Figure 8 for comparison. It shows that higher Q-factor results in narrower bandwidth.



**Figure 8: Frequency response of different solutions for  $Z_L = 100 + j100 \Omega$ . The line impedances ( $Z_{C1}$  and  $Z_{C2}$ ) are indicated in the graphs.**

The Q-factor of L-network impedance matching is fixed and determined by the source and load resistances. For the purposes of bandwidth optimisation and harmonic rejection, one can only change and control the Q-factor by utilising the Pi / T network topology (Chung, 2006). That means a total of three reactive components should be used. In the dual-section impedance matching method proposed in this paper, only two short lengths of transmission lines are needed to adjust the Q-factor. This is an added advantage of the proposed method.

A dual-section impedance matching for  $Z_L = 100 + j100 \Omega$  is implemented using the Roger RT / Duroid 5880 substrate with the dielectric constant of 2.2 and thickness of 1.575 mm. The characteristic impedance of the first section is 20  $\Omega$ , and that for the second section is 173  $\Omega$ . The total length is only 16.5 mm. For comparison, single-stub matching is also implemented. Characteristic impedance of 50  $\Omega$  is used for the transmission line and short-circuited stub line. The required length of the transmission line is 45.8 mm, and that of the stub line is 20.4 mm. The dual-section matching solution clearly shows its advantages of requiring a much shorter transmission line length and has wider bandwidth as compared to the single-stub matching solution, as shown in Figure 9.

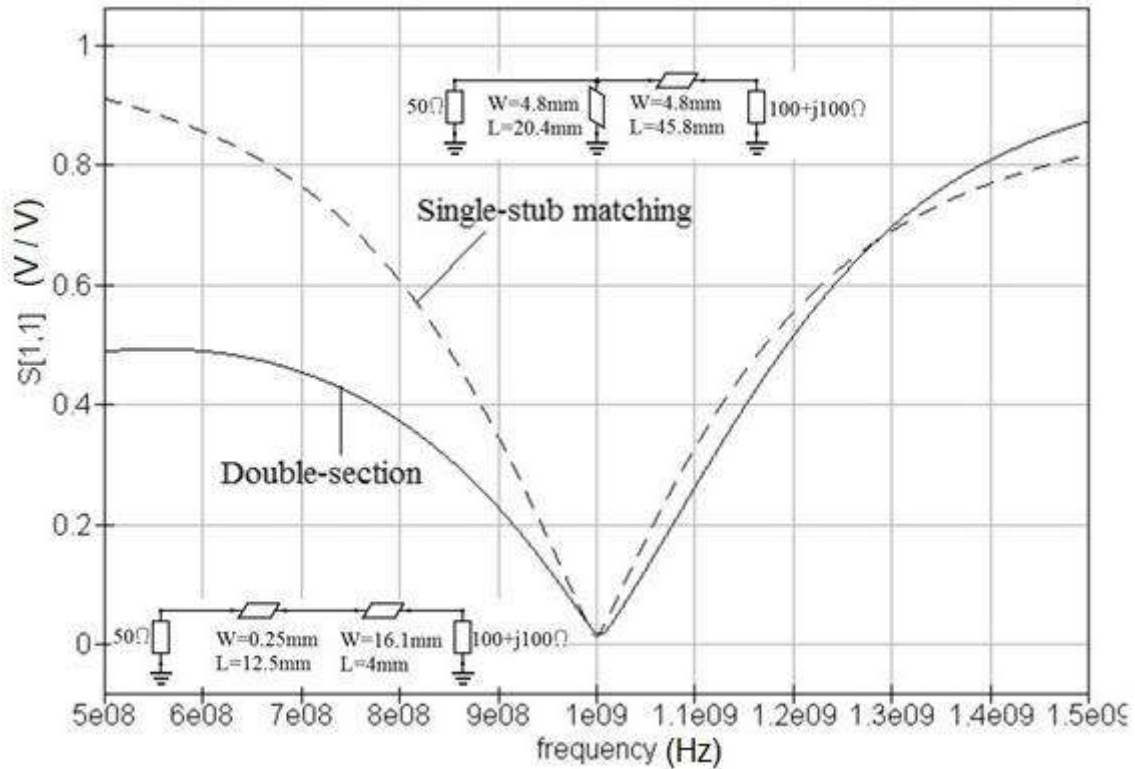


**Figure 9: Comparison of double-section matching and single-stub matching.**

## 5. CONCLUSION

Many impedance matching methods are available, including the use of multi-section transmission lines. However, to the best of the author's knowledge, there are no papers in the open literature that propose a method to shorten the transmission line length. Multi-section transmission lines typically increase the total line length for different purposes. In contrast, the impedance matching methods using single- and double-section transmission lines proposed in this paper can shorten the total length of the transmission line. A complex load impedance can be matched to a  $50\ \Omega$  source. Complex conjugate matching is also possible. The shortest possible transmission lines can be calculated using the given equations and design methodologies. It enables a significant reduction of RFIC substrate area. If the required line width is not attainable due to high / low characteristic impedance, the methods allow for modification to obtain several practical solutions, with a trade-off in a slight increase of the overall transmission line length. The Q-factor and bandwidth can be optimised to cater to different application needs through modification of the line width and length. A few design examples are presented. The use of transmission lines instead of discrete inductors / capacitors means this method can potentially be used at high microwave frequencies.

## REFERENCES

- Chung, B.K. (2006) Q-based design method for T network impedance matching. *Microelectr. J.*, **37**: 1007-1011.
- Chung, B.K. (2022) Integrated adaptive impedance matching using phase shifters. *J. Commun. Tech. Electr.*, **66**: 185-193.

- Chung, B.K. (2023) Adaptation of microwave antenna to confined spaces. *Defense S&T Tech. Bull.*: **16**, 220-227.
- Pozar, D.M. (2012). *Microwave Engineering, 4<sup>th</sup> Ed.* Wiley Global Education, New Jersey, US.
- de Lima, R.N., Huyart, B., Bergeault, E. & Jallet, L. (2000). MMIC impedance matching system. *Electron. Lett.*, **36**: 1393–1394.
- Schwartz, D.F. & Allen, J.C. (2004). Wide-band impedance matching: performance bounds. *IEEE Trans. Circuits Syst. II: Express Briefs*, **51**: 364–368.
- Thompson, M. & Fidler, J.K. (2004) Determination of the impedance matching domain of impedance matching networks, *IEEE Trans. Circuits Syst. I: Regular Papers*, **51**: 2098–2106.
- Hameed, Z. & Moez, K. (2017). Design of impedance matching circuits for RF energy harvesting systems. *Microelectr. J.*, **62**: 49 – 56.



# EVALUATION OF THE EFFECT OF MULTIPATH ON MULTI-GNSS PERFORMANCE VIA GNSS SIMULATION

Dinesh Sathyamoorthy

Science & Technology Research Institute for Defence (STRIDE), Ministry of Defence, Malaysia

\*Email: dinesh.sathyamoorthy@stride.gov.my

## ABSTRACT

*This paper is aimed at evaluating the effect of multipath on multi-Global Navigation Satellite System (GNSS) performance via GNSS simulation. The study is conducted for a Global Positioning System (GPS) receiver, Garmin GPSMAP 60CSx (Receiver R1), and two multi-GNSS receivers, Garmin GPSMAP 66sr (Receiver R2) and Trimble TDC600 (Receiver R3). Varying parameters of GNSS signal power attenuation and time delay are employed for multipath conditions of benign, moderate, challenging and difficult. It is found that with increasing severity of multipath, GNSS position error increases due to increase of GNSS signal power attenuation and time delay. Single frequency L1/ E1 GPS only and GPS + Galileo modes are both affected by multipath, though in the case of Receiver R3, the GPS + Galileo mode provides some mitigation for multipath.*

**Keywords:** *Global Navigation Satellite System (GNSS) simulation; multipath; power attenuation; time delay; position error.*

## 1. INTRODUCTION

Multipath refers to the distortion of direct line-of-sight (LOS) of Global Navigation Satellite System (GNSS) satellite signals by localised reflected / diffracted signals, caused by objects such as trees and buildings. As the multipath signals travel additional distances, they are delayed relative to the LOS signals, resulting in range measurements to the GNSS satellites being severely degraded. The multipath signals' paths are dependent on the reflecting surfaces and satellites' positions. As the satellites move with time, the multipath effect is also a variable of time. Multipath error is dependent on the architecture of GNSS receivers, in terms of the different ways the receivers process the signals (Matsushita & Tanaka, 2012; Wang *et al.*, 2018; Xue *et al.*, 2022).

There are two categories of multipath; diffuse and specular. In diffuse multipath, GNSS signals are incident on a rough surface and the reflected signals are scattered in multiple directions. It is generally uncorrelated with time and noise-like in behaviour. In specular multipath, GNSS signals are reflected from a relatively smooth surface, resulting in systematic errors in range measurement (Yi *et al.*, 2012; Lau, 2021). Multipath can also be categorised in terms of motion; static and dynamic. For a stationary GNSS receiver, the multipath geometry changes slowly, making multipath parameters essentially constant for up to several minutes. In mobile applications, the GNSS receiver can experience rapid fluctuations of multipath parameters that are hard to predict (Matsushita & Tanaka, 2012; Wang *et al.*, 2018; Xue *et al.*, 2022).

A number of studies have been conducted to study the effect of multipath on GNSS performance (Matsushita & Tanaka, 2012; Yi *et al.*, 2012; Wang *et al.*, 2018; Sathish Nayak *et al.*, 2023). The study by Dinesh *et al.* (2013) employed Global Positioning System (GPS) simulation and only focused on varying GPS signal power attenuations caused by multipath, as this was sufficient for older models of GPS receivers that generally have lower receiver sensitivity and higher receiver noise. However, as demonstrated in Dinesh *et al.* (2023), more recent versions of GNSS receivers have

higher receiver sensitivity and lower receiver noise, allowing them to operate in environments with relatively higher GNSS signal power attenuations. Hence, considering only power attenuation caused by multipath would not be adequate for these receivers.

To this end, in this paper, the study is extended to include varying GNSS signal time delays caused by multipath. The study is conducted for a GPS receiver, Garmin GPSMAP 60CSx (Garmin, 2007) (Receiver R1), and two multi-GNSS receivers, Garmin GPSMAP 66sr (Garmin, 2021) (Receiver R2) and Trimble TDC600 (Trimble, 2022) (Receiver R3).

## 2. METHODOLOGY

The study is conducted using an Aeroflex GPSG-1000 GNSS simulator (Aeroflex, 2010) in STRIDE's mini-anechoic chamber (Kamarulzaman, 2010) to avoid external interference signals and unintended multipath errors. The test setup employed is as shown in Figure 1. Simulated GNSS signals are generated using the GNSS simulator and transmitted via the coupler. The tests are conducted with the assumption that there are no ionospheric and tropospheric delays, GNSS satellite clock and ephemeris errors, interference signals, as well as unintended obstructions and multipath.

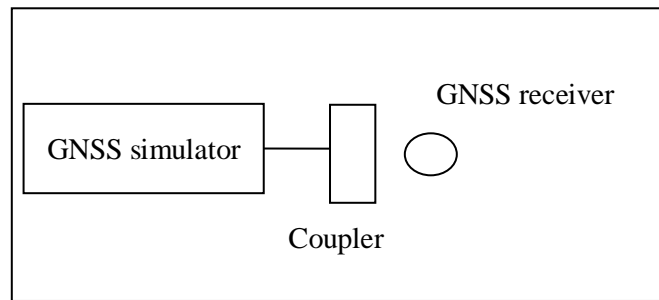


**Figure 1: The test setup employed.**

The tests are conducted for coordinated universal time (UTC) of 0000, 0300, 0600 and 0900, with the location set at Teluk Intan, Perak (N 4° E 101°). The almanac data for the periods is downloaded from the US Coast Guard's web site (USCG, 2023) and imported into the GNSS simulator.

The GNSS simulator does not provide specific multipath simulation. Instead, this study is conducted for varying parameters of GNSS signal power attenuation and time delay for multipath conditions of benign, moderate, challenging and difficult, which is adapted from Halford & Webster (2001) and shown in Table 1.

**Table 1: GNSS signal parameters for multipath conditions used in this study.**

<b>Multipath condition</b>	<b>Power attenuation (dBm)</b>	<b>Time delay (ns)</b>
Benign	2	30
Moderate	5	90
Challenging	9	150
Difficult	15	270

The GNSS simulator also does not provide specific GNSS signal time delay. However, it does allow for selection of pseudorange errors for GNSS satellites. For this study, GNSS signal time delay is simulated using the pseudorange error function, with 1 ns of clock error representing pseudorange error of 0.3 m (RAE, 2011; Bidikar *et al.*, 2014; Kaplan & Hegarty, 2017).

Based on the functionalities of the GNSS simulator, this study is conducted for the GPS L1 coarse acquisition (C/A) and Galileo E1 open service (OS) signals. The GPS L1 C/A signal is an unencrypted civilian GPS signal that is widely used by various GPS receivers. The signal has fundamental frequency of 1,575.42 MHz and code structure that modulates the signal over a 2 MHz bandwidth (USACE, 2011; Kaplan & Hegarty, 2017; DOD, 2020). The Galileo E1 OS signal also has fundamental frequency of 1,575.42 MHz, with code structure that modulates the signal over a 4 MHz bandwidth (Kaplan & Hegarty, 2017; Povero, 2019; ESA, 2021).

The tests scenarios employed for this study are shown in Table 2. For each reading, GNSS signal transmission of -130 dBm is used and average GNSS position error is recorded for a period 20 min.

**Table 2: Test scenarios employed for the evaluation of the effect multipath.**

Scenario	Number of GNSS satellites	Multipath condition	Description
GPS-FN	*GPS: 10 - 12	-	Open sky with no obstructions and full range of GPS satellites. This scenario represents an ideal scenario with no multipath, and serves as a baseline for comparison with the subsequent scenarios.
GPS-4N	GPS: 4	-	This scenario simulates a situation where obstructions limit the number of visible GPS satellites but there is no multipath. It helps demonstrate the effect of reduced satellite availability without multipath.
GPS-4B	GPS: 4	Benign	Relatively low level of multipath for GPS signals.
GPS-4M	GPS: 4	Medium	Increased severity of multipath for GPS signals.
GPS-4C	GPS: 4	Challenging	Higher severity of multipath for GPS signals.
GPS-4D	GPS: 4	Difficult	The most severe multipath condition for GPS signals.
GPS-GAL-4N	GPS: 4 Galileo: 4	-	Similar to Scenario GPS-4N, this scenario simulates limited GPS and Galileo satellite visibility due to obstructions, but no multipath.
GPS-GAL-4B	GPS: 4 Galileo: 4	Benign	Relatively low level of multipath for GPS and Galileo signals.
GPS-GAL-4M	GPS: 4 Galileo: 4	Medium	Increased severity of multipath for GPS and Galileo signals.
GPS-GAL-4C	GPS: 4 Galileo: 4	Challenging	Higher severity of multipath for GPS and Galileo signals.
GPS-GAL-4D	GPS: 4 Galileo: 4	Difficult	The most severe multipath condition for GPS and Galileo signals.

\*The full range of GPS satellites is dependant on the GPS coverage at the times set for the simulation.

### 3. RESULTS & DISCUSSION

For the tests conducted, the recorded position errors are shown in Figure 2. For scenarios GPS-4N and GPS-GAL-4N, it is observed that reduced availability of GNSS satellites causes increase of position errors. Increasing severity of multipath causes further increase of position errors due to increase of GNSS signal power attenuation and time delay. Increase of power attenuation causes decreasing carrier-to-noise density ( $C/N_0$ ) levels for GNSS satellites tracked by the receiver, which is the ratio of received GNSS signal power level to noise density. Lower  $C/N_0$  levels result in increased data bit error rate when extracting navigation data from GNSS signals, and hence, increased carrier and code tracking loop jitter. This, in turn, results in more noisy range measurements and thus, less precise positioning. Furthermore, increase of time delay results in degradation of range measurements to the GNSS satellites (USACE, 2011; Kaplan & Hegarty, 2017; DOD, 2020).

For scenarios GPS-FN and GPS-4N, it is observed that Receivers R2 and R3 recorded lower position errors as compared to Receiver R1. This is as Receivers R2 and R3 have higher receiver sensitivity and lower receiver noise, which allows them to track higher  $C/N_0$  levels for the available GNSS satellites. However, for the GPS only multipath scenarios, all three receivers show similar levels of position error.

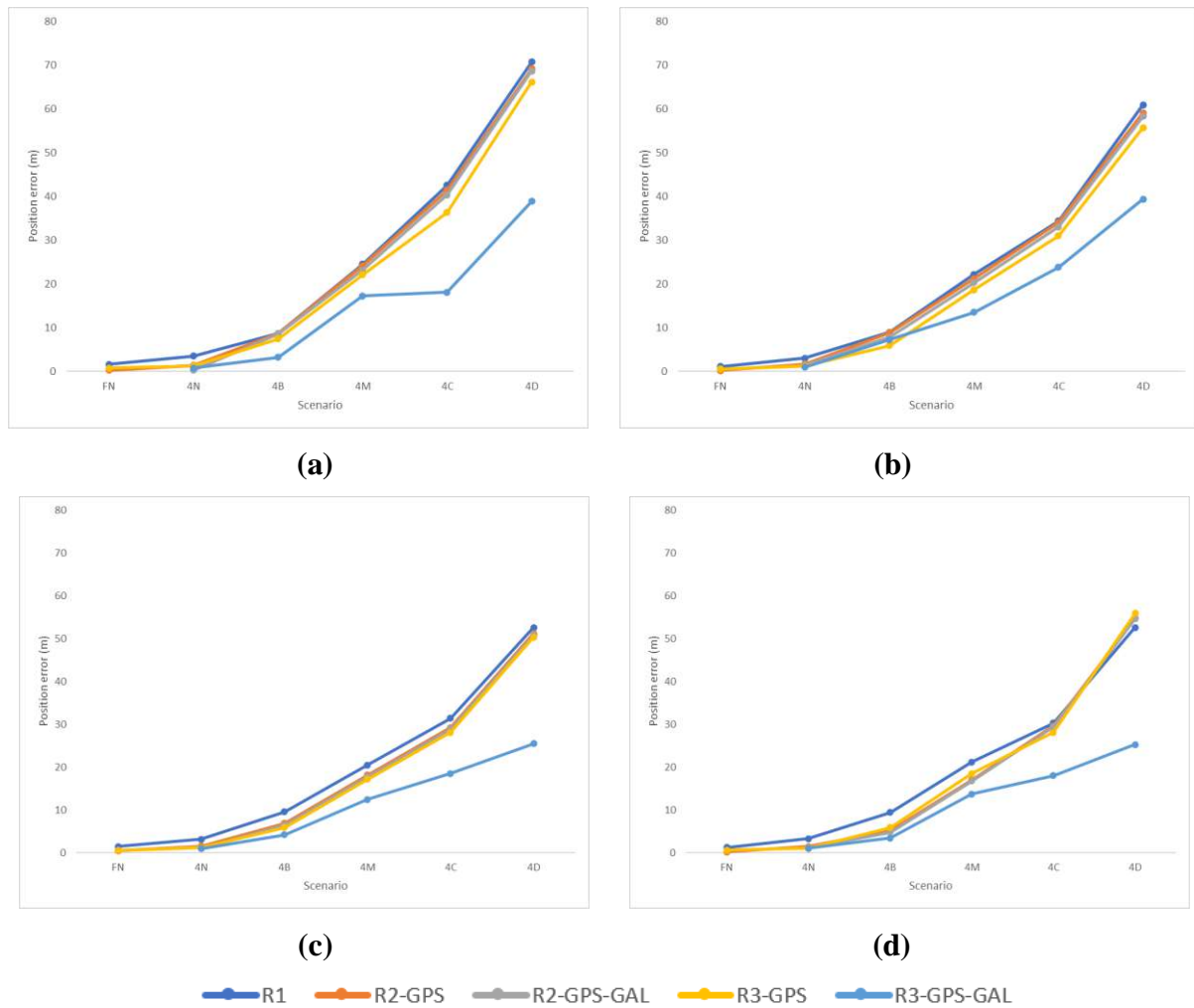


**Figure 2: The effect of increasing severity of multipath on the GNSS receivers for: (a) UTC 0000 (b) UTC 0300 (c) UTC 0600 (d) UTC 0900.**

For scenario GPS-GAL-4N, the higher number of GNSS satellites observed for the GPS + Galileo mode allows Receivers R2 and R3 to have lower position errors as compared Scenario GPS-4N. This highlights the advantage of multi-GNSS in degraded environments, such as in dense urban and forest areas.

For Receiver R2, the GPS + Galileo mode does not provide any mitigation for multipath, with similar position errors observed as the GPS only mode. For Receiver R3, the GPS + Galileo mode provides some level of mitigation with lower positions errors observed as compared to the GPS only mode. This could be as the receiver makes use of the alternative binary offset carrier (AltBOC) modulation that is employed for the Galileo E1 OS signal, which is aimed at improving the robustness of the signal against various sources of interferences, including multipath (Kaplan & Hegarty, 2017; Povero, 2019; ESA, 2021).

Varying position error patterns are observed for each of the readings. This is due to the GNSS satellite constellation being dynamic, causing varying satellite geometry over time, resulting in GNSS accuracy being location / time dependent (USACE, 2011; Kaplan & Hegarty, 2017; DOD, 2020).

The tests conducted in this study employed GNSS signal power level of -130 dBm. Usage of lower GNSS signal power levels would result in reduced  $C/N_0$  levels and hence, higher rates of increase of position error values.

It should be noted that the tests conducted in this study are for only three GNSS receivers. Additional tests using a wider range of GNSS receivers are needed to further validate the findings of this study. Furthermore, a limitation faced in this study is that it is only conducted for the GPS L1 / Galileo E1 signals. Receiver R2 is a dual-frequency GNSS receiver that supports GPS L1 / Galileo E1 and GPS L5 / Galileo E5. The use of multiple frequency bands allows for more consistent tracklogs and improved positioning in challenging environments. In addition, dual-frequency systems are better able to filter out multipath signals from obstacles (Kaplan & Hegarty, 2017; Povero, 2019; DOD, 2020; ESA, 2021). To this end, the proposed future work is for the procurement of a GNSS simulator that will allow transmission of multifrequency GNSS signals.

#### **4. CONCLUSION**

It is found that with increasing severity of multipath, GNSS position error increases due to increase of GNSS signal power attenuation and time delay. Single frequency L1/ E1 GPS only and GPS + Galileo modes are both affected by multipath, though in the case of Receiver R3, the GPS + Galileo mode provides some mitigation for multipath. Future studies are aimed at evaluating the ability of multifrequency GNSS in mitigating multipath.

#### **REFERENCES**

- Aeroflex (2010). *Avionics GPSG-1000 GPS / Galileo Portable Positional Simulator*. Aeroflex Inc., Plainview, New York.
- Bidikar, B., Rao, G.S., Ganesh, L. & Kumar, M.S. (2014). Satellite clock error and orbital solution error estimation for precise navigation applications. *Positioning*, **5**: 22-26.
- Dinesh, S., Shalini, S., Zainal Fitry, M.A. & Siti Zainun, A. (2013). Evaluation of the repeatability of Global Positioning System (GPS) performance with respect to GPS satellite orbital passes. *Defence S&T Tech. Bull.*, **6**: 130-140.
- Dinesh, S., Hafizah, M.Y., Ahmad Firdaus, A.K. Mohd Zuryn, M.D. & Maizurina, K. (2023). Evaluation of multi-GNSS performance via GNSS simulation. *Defence S&T Tech. Bull.*, **16**: 13-23.

- DOD (Department of Defence) (2020). *Global Positioning System Standard Positioning Service Performance Standard, Command, Control, Communications, and Intelligence, 5<sup>th</sup> Ed.* Department of Defence (DOD), Washington D.C.
- ESA (European Space Agency) (2021). *European GNSS (Galileo) Open Service Signal-in-Space Interface Control Document.* European Space Agency (ESA), Paris, France.
- Garmin (2007). *GPSmap 60CSx Owner's Manual.* Garmin International Inc., Olathe, Kansas.
- Garmin (2021). *GPSMAP 66 Owner's Manual.* Garmin International Inc., Olathe, Kansas.
- Halford, K. & Webster, M. (2001). Multipath Measurement in Wireless LANs. Intersil, Florida, US.
- Kamarulzaman, M. (2010). *Technical Specification for STRIDE's Mini-Anechoic Chamber.* Science & Technology Research Institute for Defence (STRIDE), Ministry of Defence, Malaysia.
- Kaplan, E.D. & Hegarty, C.J. (2017). *Understanding GPS: Principles and Applications.* Artech House, Norwood, Massachusetts.
- Lau, L. (2021). GNSS multipath errors and mitigation techniques. In Petropoulos, G.P. & Srivastava, P.K. (Eds.), *GPS and GNSS Technology in Geosciences*, Elsevier, Amsterdam, Netherlands, pp. 77-98.
- Matsushita, T. & Tanaka, T. (2012). Study on improving the accuracy of satellite measurement in urban areas. *T. Soc. Instrumen. Control Eng.*, **48**: 73-77.
- Povero, G. (2019). *GNSS Signals Introduction.* Links Foundation, Torino, Italy.
- Royal Academy of Engineering (RAE) (2011). *Global Navigation Space Systems: Reliance and Vulnerabilities.* Royal Academy of Engineering, London.
- Sathish Nayak, B., Krishna Naik, K., Odelu, O. & Surendra, P. (2023). GPS receiver simplification for low-cost applications and multipath mitigation analysis on SDR-based re-configurable software receiver. *Defence Sci. J.*, **73**: 699-711.
- Trimble (2022). *Trimble TDC600 Handheld.* Trimble, Colorado, US.
- USACE (US Army Corps of Engineers) (2011). *Engineer Manual EM 1110-1-1003: NAVSTAR Global Positioning System Surveying.* US Army Corps of Engineers (USACE), Washington D.C.
- USCG (US Coast Guard) (2023). *GPS NANUs, Almanacs, & Ops Advisories.* Available online at: <https://www.navcen.uscg.gov/gps-nanus-almanacs-opsadvisories-sof> (Last access date: 8 June 2023).
- Wang, Y., Chen, X. & Liu, P. (2018). Statistical multipath model based on experimental GNSS data in static urban canyon environment. *Sensors*, **18**: 1149.
- Xue, Z., Lu, Z., Xiao, Z., Song, J. & Ni, S. (2022). Overview of multipath mitigation technology in global navigation satellite system. *Front. Phys.*, **10**: 1071539.
- Yi, T.H., Li, H.N. & Gu, M. (2012). Effect of different construction materials on propagation of GPS monitoring signals. *Measurement*, **45**: 1126-1139.

# GPS JAMMING IMPACT ON UAV PERFORMANCE IN OUTDOOR ENVIRONMENTS

Nurhakimah Norhashim<sup>\*1</sup>, Nadhiya Liyana Mohd Kamal<sup>1</sup>, Zulhilmy Sahwee<sup>1</sup>, Shahrul Ahmad Shah<sup>1</sup>  
Nur Afiqah Alfian<sup>1</sup> & Dinesh Sathyamoorthy<sup>2</sup>

<sup>1</sup>Unmanned Aerial System Research Laboratory, Avionics Section, Malaysian Institute of Aviation Technology, Universiti Kuala Lumpur, Malaysia

<sup>2</sup>Science & Technology Research Institute for Defence (STRIDE), Ministry of Defence, Malaysia

\*Email: nurhakimah@unikl.edu.my

## ABSTRACT

Due to long-distance propagation, the received Global Navigation Satellite System (GNSS) signal power is low, making it highly susceptible to signal interference. In safety-critical applications such as unmanned aerial vehicles (UAVs), GNSS signal interference can lead to significant position, navigation and timing (PNT) service deterioration or interruption. Therefore, this work focuses on investigating the effects of Global Positioning System (GPS) jamming on a DJI Mini 2 UAV and a Garmin GPSMAP 60CSx handheld GPS receiver based on various interference signal power levels and rotation angles. The field evaluation is conducted in an open area and GPS interference signals are generated using a signal generator. The signal is emitted to the target UAV using a directional antenna, and the effect of the signal is analysed and evaluated. Then, using the same setup, the measurement is repeated by varying the rotation angles of the UAV to 0, 45 and 90°. The findings indicate that when a jammer's signal reaches approximately -110 dBm in an outdoor setting, it significantly affects GPS accuracy. The impact of GPS jamming on rotation angles is influenced by altering the UAV's position (lateral and upright) as a result of changes in antenna orientation (facing upwards or towards the interference signal).

**Keywords:** Global Positioning System (GPS) jamming; unmanned aerial vehicle (UAV); field evaluation; estimate probable error (EPE); rotation angle.

## 1. INTRODUCTION

Unmanned aerial vehicle (UAV) technologies have advanced rapidly in the last several years, and as a result, various industries have adopted it for surveying, agriculture, environmental monitoring, as well as transportation of products and medical supplies (Nurhakimah *et al.*, 2023; Zhang & Zhu, 2023). By 2025, the UAV market is projected to experience a compound annual growth rate (CAGR) of 56.5% (Adroit, 2022). Future 5G networks are anticipated to benefit greatly from UAV support for backhaul link operations and flexible deployment (Nadhiya Liyana *et al.*, 2019). In military applications, UAVs are heavily used, focusing on surveillance, target tracking and air-to-ground combat (Mohsan *et al.*, 2022). The security of wireless communications between UAVs and ground systems is crucial. To this end, the security protocols and strategies to guarantee fundamental security elements (privacy preservation and mutual authentication) in UAV networks have been given emphasis. Nonetheless, UAVs are still facing security vulnerabilities. It has been demonstrated that even professional UAVs employed for delicate and important tasks such as enemy observation and law enforcement operations have security vulnerabilities. When they are compromised, the UAV can be remotely disabled, hijacked, taken away or stolen by terrorists and criminals for illegal surveillance and unmanned attacks (Dinesh, 2015; Khan *et al.*, 2021; Vinay *et al.*, 2021).

Global Navigation Satellite System (GNSS) is a crucial component for military and civilian UAV navigation. However, GNSS is susceptible to jamming due to its weak signals. In the past ten years, there has been growing concern about the dependable usage of GNSS signals due to the proliferation of low-cost jamming devices. Large positioning, navigation and timing (PNT) errors, loss of control and even total denial of service are all possible outcomes of GNSS jamming attacks (Dinesh *et al.*, 2012, 2020; 2023; Seferoglu & Turk, 2019; Nurhakimah *et al.*, 2022; Islam *et al.*, 2022).

GNSS jamming is considered as one of the serious risks to UAVs due to its feasibility and ease to conduct (Dinesh 2015; Dinesh *et al.*, 2020; Khan *et al.*, 2021; Nurhakimah *et al.*, 2022; Sabitha Banu & Padmavathi, 2022). Numerous actual instances of signal interferences have been documented in the last decade, including an event at Newark Airport in 2013. In this incident, a truck driver employed a compact jamming device to disrupt a Global Positioning System (GPS) tracker within the company's fleet monitoring system. Consequently, the airport's ground-based augmentation system (GBAS), crucial for aiding aircraft during takeoff and landing, experienced malfunctions. The disturbance continued for about two years until the incidents were officially identified by the US Federal Communications Commission (FCC) as cases of GPS jamming (Matyszczyk, 2013). In October 2018, there was a reported incident in Hong Kong where a GPS signal jammer caused more than 40 UAVs to fall from the sky during a professional light show (Elghamrawy *et al.*, 2020). Incidents like these highlight the need for robust security measures to prevent and detect unauthorised use of jamming devices.

The objective of this work is to investigate the effects of different levels of GPS jamming signals on UAVs in an outdoor environment. This study focuses on two variables, which are the interference signal power level and rotation angle.

## 2. EXPERIMENTAL SETUP

The study to examine the impact of GPS jamming attacks via field evaluation was conducted using an IFR 2023B signal generator and Hyperlog 60180 directional antenna for a Garmin GPSMAP 60CSx handheld GPS receiver and a DJI Mini 2 UAV. In this setup, the signal generator transmitted GPS jamming signals via the directional antenna. The GPS coverage during the measurement period was good with high satellite visibility (between 10 to 12 satellites). This study was conducted in an open area at the STRIDE Block B car park (STRIDE, Kajang, Selangor, Malaysia, N 2° 58' E 101° 48') on 19 September 2023. The surrounding environment has low-rise office buildings and open spaces. This location was chosen to study how GPS jamming affects UAVs in a real outdoor setting. The setup for the field evaluation is as shown in Figures 1 and 2.

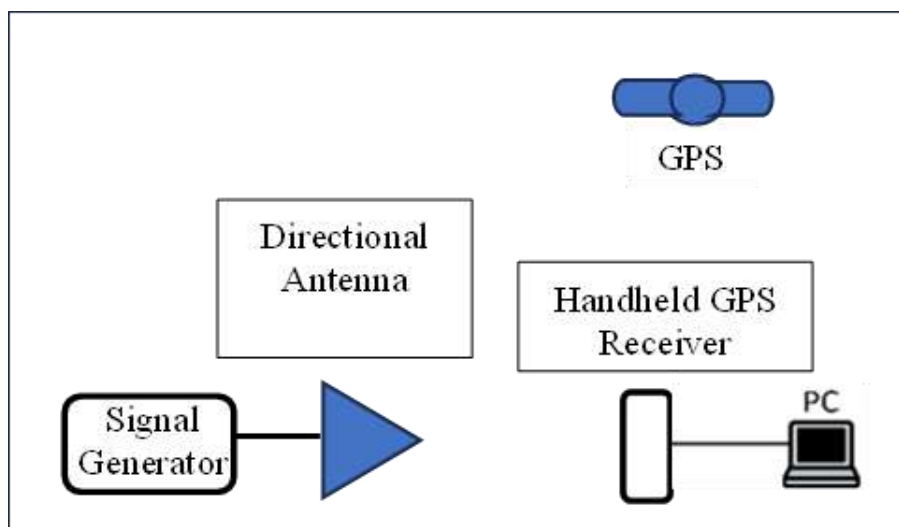
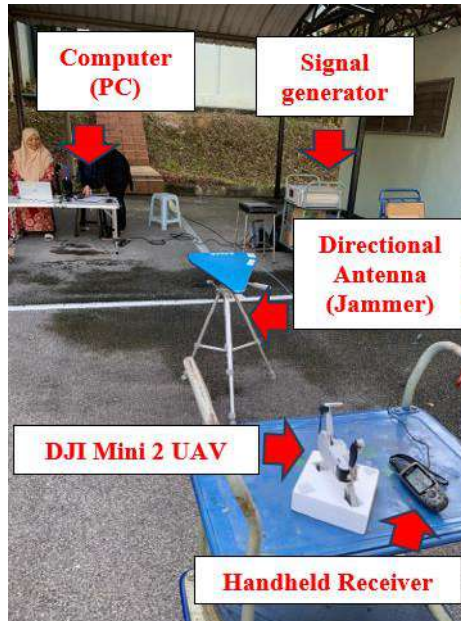


Figure 1: Illustration of field evaluation setup for the study on the effect of GPS jamming.





**Figure 2: The field evaluation setup.**

The experiment was initially conducted for the handheld GPS receiver, which used the GPS L1 coarse acquisition (C/A) signal with fundamental frequency of 1,575.42 MHz. The effect of GPS jamming was evaluated using estimate probable error (EPE), which indicates a 3D confidence ellipsoid that illustrates measurement uncertainties in all three coordinates (USACE, 2011; Kaplan & Hegarty, 2017; DOD, 2020). The measurements were then repeated with the same experimental setup to study the effect of GPS jamming on the UAV with varying the rotation angles. The rotational angles involved were 0, 45 and 90° in lateral and upright positions, as shown in Figure 3.



**Figure 3: The rotational angle measurement with 0, 45 and 90° for the upright position.**

The interference signal generated by the signal generator was a frequency-modulated (FM) signal transmitted in increments of 3 dBm, commencing at -140 dBm and continuing until the GPS receiver encountered jamming. The GPS Diagnostics software was used to record EPE values. An example of EPE value when the signal is not jammed is visualised in Figure 4. When the GPS receiver is jammed, as shown in Figure 5, no positional information is shown on the software.

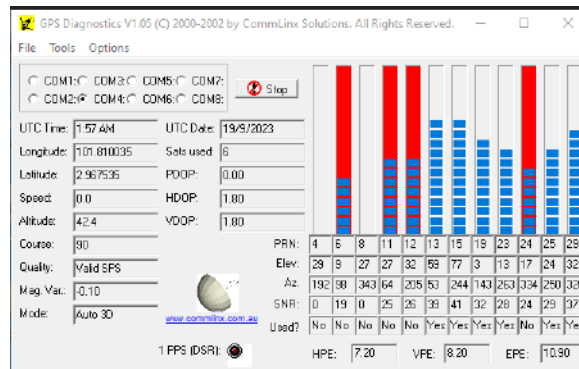


Figure 4: The GPS Diagnostics software shows the EPE value when the GPS receiver is not jammed.

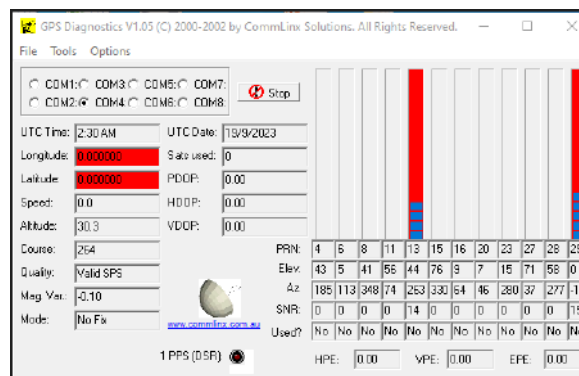


Figure 5: The GPS Diagnostics software shows that the EPE value is 0 when the GPS receiver is jammed.

### 3. RESULTS & DISCUSSION

In this section, the results of the effects of GPS jamming using the handheld GPS receiver are presented and discussed, followed by the results for different rotation angles for the UAV.

#### 3.1 Effects of GPS Interference Signal On EPE

Figure 6 compares the effect of increasing interference signal power levels on EPE for open environment conducted in this study and for controlled environment conducted in Nurhakimah *et al.* (2022). When the interference level exceeded -110 dBm in the open environment, EPE values started to notably increase. In comparison, for the controlled environment, the EPE values only started to increase abruptly at interference level exceeding -90 dBm. Thus, the two different environments give effect to the EPE values and interference levels. The increase in interference levels correlated with increase in EPE values, due to diminishing ratio of received GPS signal power to noise density. Elevating the interference level beyond -83 dBm for the open environment and -74 dBm for the controlled environment resulted in the GPS receiver being jammed, rendering it incapable of providing information on EPE and position.

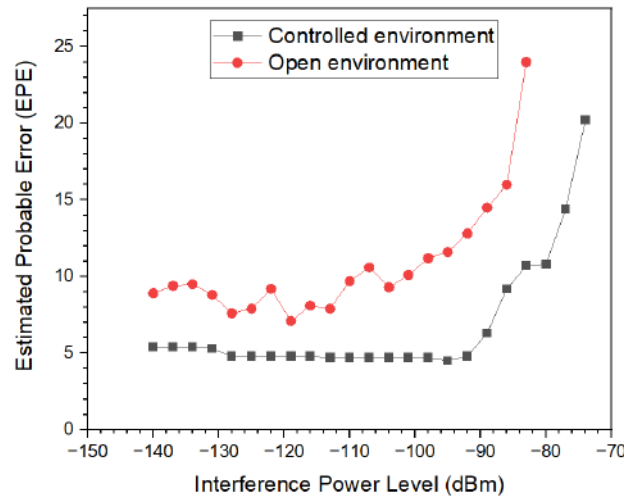


**Figure 6: Graph for EPE vs interference signal power level for the effect of GPS jamming in controlled and open environments.**

For the controlled environment, such as using a GPS simulator in an anechoic chamber in the case of Dinesh *et al.* (2012, 2020) and Nurhakimah *et al.* (2022), the interference signal power level required to induce error is larger as compared to when jamming is performed in an open environment. This indicates that GPS is more susceptible for jamming at open environments as compared to controlled settings. This susceptibility for open environments arises due to multipath propagation caused by GPS signals reflecting off various outdoor objects, such as trees and buildings, as well as atmospheric delays. These multipath and atmospheric delay scenarios facilitate easier manipulation of signals by jammers (Seferoglu & Turk, 2019; Dinesh *et al.*, 2023). In contrast, an anechoic chamber minimises such reflections, creating a controlled test environment without external interference. Consequently, GPS is more prone to interference and manipulation by jammers at outdoor environments than in controlled environments.

### 3.2 Effects of Varying Rotation Angles

The results for the field measurement for varying rotation angles of the UAV can be divided into two different positions:

- a) First UAV position: Lateral
- b) Second UAV position: Upright

The effect of UAV rotation angles on EPE are shown in Figures 7 and 8. For the lateral position (Figure 7), at fixed rotation angle, the graph shows increasing trend. There are no obvious changes of EPE values except at 90°. For the upright position (Figure 8), all the rotation angles show increasing trend. The EPE value is the highest when the UAV's position is at 0° at interference level of -89 dBm. The EPE values for the upright position are approximately five times higher than the lateral position due to the antenna position facing towards the interference signal source. At the lateral position, the antenna is facing upwards, thus the probability of jamming is less than when the antenna is facing towards the interference signal. Variation is also observed in EPE performance for different UAV positions. This may be contributed by the orientation of the GPS antenna installed in the UAV resulting in different antenna gains at different UAV positions. This observation indicates that the positioning of the UAV is a crucial factor in determining its performance in the presence of jammers.

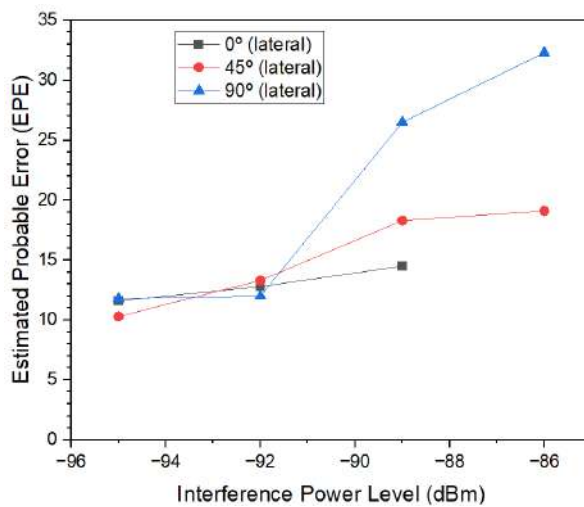


**Figure 7: Graph of EPE vs interference signal power level for the effect of GPS jamming by varying the rotation angle of the UAV for the lateral position.**

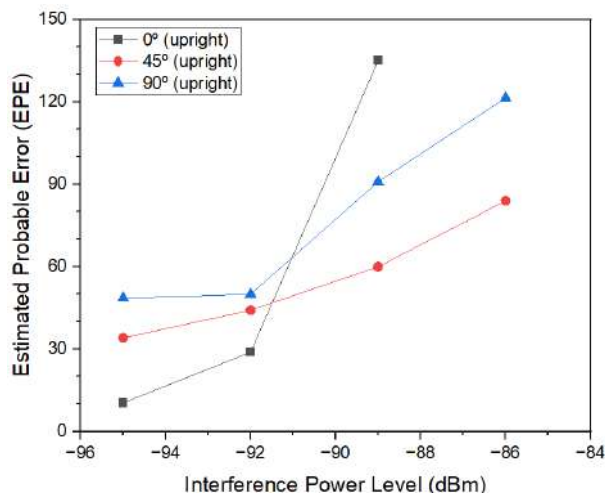


**Figure 8: Graph of EPE vs interference signal power level for the effect of GPS jamming by varying the rotation angle of the UAV for the upright position.**

Figure 9 shows the GPS satellite signal strength on the DJI interface. When the number of satellites in view are less than five, it means that the signal has been jammed / satellite signal strength is low. On the DJI screen, the satellite symbol turned from white to red, indicating that the GPS signal has been jammed. The highest number of observed GPS satellites was detected when the UAV was rotated to 45° (lateral). At 0°, for both lateral and upright positions, it is observed that the lowest number of GPS satellites are viewed, three and four respectively. Based on this, it is vital to acknowledge that when devising strategies to counter interference, one must consider the effects of the angle at which the jamming incident occurs.

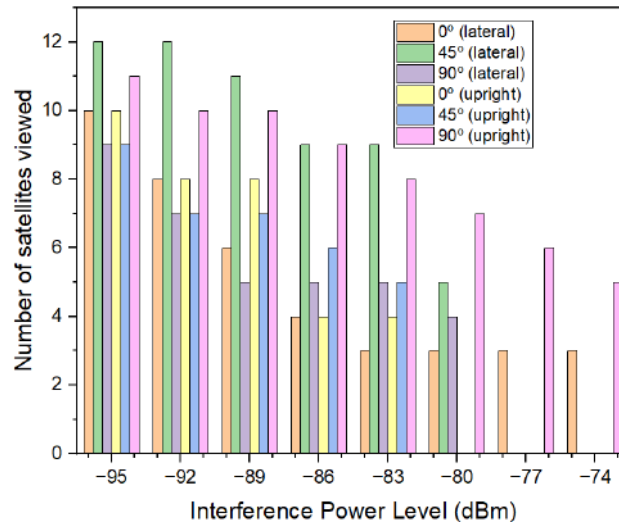


**Figure 9: Number of satellites viewed vs interference power level.**

#### 4. CONCLUSION

This study focused on analysing the impact of GPS jamming on UAV performance in a real field scenario, concentrating specifically on interference signal power levels and rotation angles. Comparing outdoor and controlled (anechoic chamber) environments, it is evident that although the trend of jamming effects remains similar, the outdoor setting requires slightly lower interference signal power level to induce effects akin to the controlled environment.

Additionally, the investigation into UAV positioning and rotation angles revealed substantial variations in EPE values under jamming conditions. Notably, for the lateral UAV position, increase of EPE values with angle changes was found to be much smaller as compared to the upright position, due the orientation of the GPS antenna installed in the UAV resulting in different antenna gains at different UAV positions. This comprehensive analysis sheds light on the nuanced impact of jamming signal levels and UAV orientations, providing valuable insights for enhancing UAV resilience in real-world settings.

#### ACKNOWLEDGMENT

This work was supported by the Ministry Higher Education of Malaysia under the Fundamental Research Grant Scheme (FRGS) Grant number FRGS/1/2022/TK04/UNIKL/02/12.

#### REFERENCES

- Adroit (2022). *Drones Market Size by Product, Application and Forecast to 2025*. Adroit Market Research, Texas, US.
- Dinesh, S. (2015). A review of security threats of unmanned aerial vehicles and mitigation steps. *J Defence Secur.*, **6**: 81-97
- Dinesh, S, Mohd Faudzi, M. & Zainal Fitry, M.A. (2012a). Evaluation of the effect of radio frequency interference (RFI) on Global Positioning System (GPS) accuracy via GPS simulation. *Defence. Sci. J.*, **62**: 338-347.
- Dinesh, S., Zainal Fitry, M.A, Esa, S.,Shahrudin, E.S., Ahmad Firdaus, A.K & Zaherudin, Z. (2020). Evaluation of the vulnerabilities of unmanned aerial vehicles (UAVs) to Global Positioning System (GPS) jamming and spoofing. *Defence S&T Tech. Bull.*, **13**: 333-343.

- Dinesh, S., Hafizah, M.Y., Ahmad Firdaus, A.K. Mohd Zuryn, M.D. & Maizurina, K., 2023. Evaluation of the effect of radio frequency interference (RFI) on dual-frequency Global Navigation Satellite System (GNSS). *Defence S&T Tech. Bull.*, **16**: 228-237.
- DOD (Department of Defence) (2020). *Global Positioning System Standard Positioning Service Performance Standard, Command, Control, Communications, and Intelligence*, 5<sup>th</sup> Ed. Department of Defence (DOD), Washington D.C.
- Elghamrawy, H., Karaim, M., Tamazin, M. & Noureldin, A. (2020). Experimental evaluation of the impact of different types of jamming signals on commercial GNSS Receivers. *Appl. Sci.* 2020, **10**: 4240.
- Islam, S., Bhuiyan, M.Z.H., Thombre, S. & Kaasalainen, S. (2022). Combating single-frequency jamming through a multi-frequency, multi-constellation software receiver: A case study for maritime navigation in the Gulf of Finland. *Sensors*, **22**: 2294.
- Kaplan, E.D. & Hegarty, C.J. (2017). *Understanding GPS: Principles and Applications*. Artech House, Norwood, Massachusetts.
- Khan, S.Z., Moshin, M. & Iqbal, W. (2021). On GPS spoofing of aerial platforms: a review of threats, challenges, methodologies, and future research directions. *PeerJ Comput. Sci.*, **7**: e507
- Matyszczuk, C. (2013). *Truck Driver Has GPS Jammer, Accidentally Jams Newark Airport*. Available online at: <https://www.cnet.com/culture/truck-driver-has-gps-jammer-accidentally-jams-newark-airport> (Last access date: 12 January 2023).
- Mohsan, S.A.H., Khan, M.A., Noor, F., Ullah, I. & Alsharif, M.H. *Applications of Unmanned Aerial Vehicles*. Available online at: <https://encyclopedia.pub/entry/25512> (Last access date: 30 November 2023).
- Nadhiya Liyana, M.K., Sahwee, Z., Abdul Hamid, S., Norhashim, N. & Lott, N. (2019). Cellular network and its relevance for unmanned aerial vehicle application in Malaysia. *IOP Conf. Ser. Mater. Sci. Eng.*, **705**: 012009.
- Nurhakimah, N, Mohd Kamal, N.L., Sahwee, Z., Lott, N., Abdul Hamid, S., Wan Jusoh, W.N.B., Ahmad, S., Mahmood, A.S. & Ahmad Ruzaini, A.I. (2020). Ground Positioning System (GPS) spoofing avoidance utilizing Frequency Selective Surface (FSS) method. *J. Adv. Res. Dyn. Control Syst.*, **12**: 1755-1760.
- Nurhakimah, N, N.L. Mohd Kamal, Z. Sahwee, S. A. Shah and Sathyamoorthy, D. The effects of jamming on Global Positioning System (GPS) accuracy for unmanned aerial vehicles (UAVs). *2022 Int. Conf. Comp. Drone Appl. (IConDA 2022)*, 28-29 November 2022, Kuching, Malaysia.
- Nurhakimah, N., Mohd Kamal, N.L., Ahmad Shah, S., Sahwee, Z. & Ahmad Ruzani, A.I. (2023). A review of unmanned aerial vehicle (UAV) technology adoption for precision agriculture (PA) in Malaysia. *Unmanned Syst.*, doi 10.1142/s230138502450016x.
- Sabitha Banu, A. & Padmavathi, G. (2022). Taxonomy of UAVs GPS spoofing and jamming attack detection methods. In Ouaisa, M., Khan, I.L., Ouaisa, M., Boulouard, Z. & Hussain Shah, S.B. (Eds.), *Computational Intelligence for Unmanned Aerial Vehicles Communication Networks*, Springer, Berlin, Germany.
- Seferoglu, K.T & Turk, A.S. (2019). Review of spoofing and jamming attack on the global navigation systems band and countermeasure. *9<sup>th</sup> Int. Conf. Recent Adv. Space Tech (RAST 2019)*, 11-14 June 2019, Istanbul, Turkey.
- USACE (US Army Corps of Engineers) (2011). *Engineer Manual EM 1110-1-1003: NAVSTAR Global Positioning System Surveying*. US Army Corps of Engineers (USACE), Washington D.C.
- Vinay, C., Pavan, K., Aayush, A., Navneet, G. & Mohsen, G. (2021) A comprehensive review of unmanned aerial vehicle attacks and neutralization techniques. *Ad Hoc Netw.*, **111**: 102324.
- Zhang, Z. & Zhu, L.A. (2023) Review on unmanned aerial vehicle remote sensing: Platforms, sensors, data processing methods, and applications. *Drones*, **7**: 398.

# A CASE STUDY OF FAILURE REPORTING ANALYSIS AND CORRECTIVE ACTION SYSTEM (FRACAS) FOR MEDICAL OXYGEN PLANT (MOP)

Manmeet Singh\* & Nilesh Ware

Department of Technology Management, Defence Institute of Advanced Technology, India

\*Email: ms\_pec@yahoo.com

## ABSTRACT

*Failure reporting analysis and corrective action system (FRACAS) is used during the development, manufacturing and deployment stages of a product. It helps in the knowledge process to learn about the root cause of failure through failure analysis and then implement the required corrective action. The objective of this research is to propose a productivity-oriented FRACAS framework and to determine its usefulness at a manufacturer site for medical oxygen plant (MOP). MOP is a spin-off technology of the onboard oxygen generating system (OOGS) used in defence fighter aircrafts. During implementation, the FRACAS framework was found to have effectiveness of 89%, with testing failure rate being reduced significantly.*

**Keywords:** *Failure reporting analysis and corrective action system (FRACAS); medical oxygen plant (MOP); failure analysis, corrective action; acceptance testing.*

## 1. INTRODUCTION

Failure reporting analysis and corrective action system (FRACAS) is important during the design evaluation and manufacturing stages to minimise defects in the product during its actual usage by the customer. In FRACAS, each failure should be reported separately, then verified and analysed to identify the root causes of the failure, with suitable corrective action taken to eliminate the failure. Finally, the effectiveness of the corrective action is monitored. If the corrective action does not work, then the whole analysis should be repeated, which makes FRACAS a closed-loop procedure (DOD, 1995; Braglia *et al.*, 2021).

During the second wave of the COVID-19 pandemic in India, due to the shortage of medical oxygen in hospitals, the defence technology of onboard oxygen generating system (OOGS), which was originally designed for defence fighter aircrafts, was redesigned for greater capacity, resulting in spin-off technology of medical oxygen plant (MOP). This design was transferred to manufacturing partners to produce large numbers of MOPs to cater for the requirement of medical oxygen in hospitals. MOP consists of a compressor, dryer, air reservoir, two oxygen concentrator tanks and oxygen reservoir from which supply is given to the hospital (Jha & Gaur, 2022).

FRACAS is usually deployed during the design, development, manufacturing or operational stages. During the manufacturing stage, the type of FRACAS used is process-oriented FRACAS in which all the manufacturing processes are monitored for failures. Ordinarily, during testing, FRACAS is implemented at the design evaluation or qualification testing stages (Susanto *et al.*, 2017; Tanner, 2020; Chang *et al.*, 2021; Sakhaei, 2023). However, due to the substantial requirement of MOPs in hospitals, for this case, FRACAS was only implemented at the acceptance testing stage.

This paper proposes a productivity-oriented FRACAS framework for MOP failures at a manufacturer's site. In this framework, the failure is reported, verified and analysed for root cause and corrective action, and finally, the efficacy of corrective action is estimated during acceptance testing.

In productivity-oriented FRACAS, the acceptance testing process is monitored for failures, as compared to process-oriented FRACAS whereby all the manufacturing processes are monitored for failures. The usefulness of the FRACAS process during the production acceptance stage will save the losses for the manufacturing factory, as well as increase the success and profitability of product manufacturing.

## 2. METHODOLOGY

### 2.1 FRACAS Framework

The proposed framework of the productivity-oriented FRACAS process is shown in Figure 1. The framework includes the following steps:

- (a) First step: Failure reporting of each failure with the failure reporting date. When the product has failed during the acceptance testing, the failure has to be reported. The required format for failure reporting should consist of serial numbers (including skid numbers) of all the sub-systems for traceability, acceptance criteria against which it has failed, sub-system that has failed (if identifiable), and the date of failure. Production of future lots has to be stopped.
- (b) Second step: Failure verification by quality and reliability experts, who visit the failure site, verify the failure and confirm that the sub-system has failed (if identifiable).
- (c) Third step: Failure analysis to identify the root cause of the failure and the corrective action to eliminate the failure. The failure assessment team, consisting of design, subject, and quality and reliability experts, uses the fault tree analysis method to identify the root cause and recommend corrective action. If the failure assessment team is not able to identify a single root cause, then it should identify the multiple likely root causes and recommend multiple corrective actions to address these likely root causes.
- (d) Fourth step: The corrective action suggested by the failure assessment team is implemented and examined.
- (e) Fifth step: Acceptance testing is conducted to assess the effectiveness of the corrective action. This step is the novelty of the proposed productivity-oriented FRACAS framework.
- (f) Last step: If acceptance testing is cleared, change acceptance and implementation for all future lots is carried out. Production of future lots is then restarted. On the other hand, if acceptance testing is not cleared, then the steps from the third step (failure analysis) are repeated.

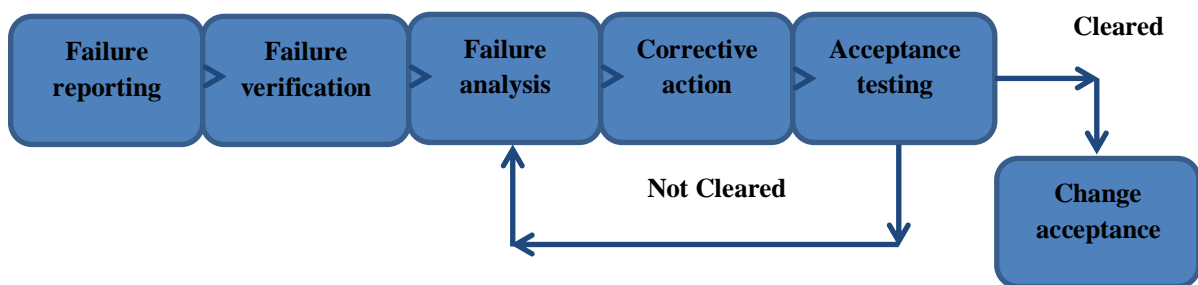


Figure 1: Framework of productivity-oriented FRACAS process.



## 2.2 Principle of Pressure Swing Adsorption (PSA) Medical Oxygen Plant (MOP)

The schematic of PSA MOP is shown in Figure 2. Ambient air is compressed for up to 5.5 bar by the compressor, water vapour content in the air is removed by the air dryer, and then air is collected at the air reservoir. From the air reservoir, the air is filtered and it passes through the oxygen concentrator tank from the bottom to the top of the tank and adsorption takes place. The PSA process consists of two oxygen concentrator tanks. During adsorption in Oxygen Concentrator Tank 1, desorption takes place in Tank 2, and during adsorption in Oxygen Concentrator Tank 2, desorption takes place in Tank 1. The process works within cycles in which a concentrator tank recurrently experiences a series of pressurisation, adsorption and desorption steps. The oxygen concentrator consists of molecular sieves (i.e., zeolite as adsorbent, desiccant and ceramic balls / saddles) and during adsorption when air at high pressure is passed over it, nitrogen molecules are adsorbed at the bottom, pure oxygen is collected at the top exit of the oxygen concentrator and this continues until the nitrogen saturates the concentrator tank. This nitrogen is vented from the tank at reduced pressure through desorption. During desorption, oxygen from the other oxygen concentrator tank (where adsorption is taking place) is passed from top to bottom of the desorbed oxygen concentrator tank to vent out the nitrogen. Pure oxygen collects in an oxygen reservoir and it is supplied to the hospital at pressure range of 4.2 to 5.5 bar. The open end points in the figure are the safety valves for emergency pressure release (Jha & Gaur, 2022).

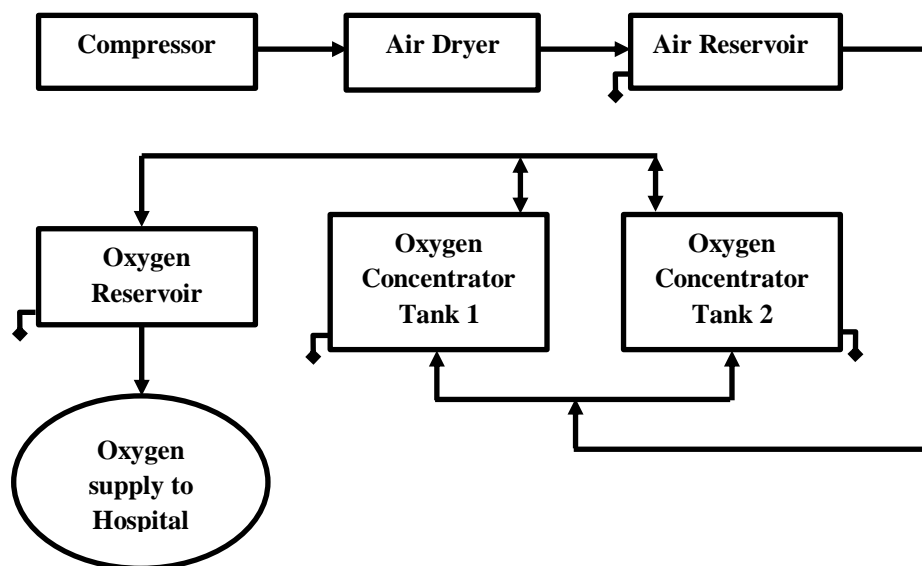


Figure 2: Schematic of PSA MOP (Source: Jha & Gaur, 2022).

## 2.3 Failure Modes of PSA MOP

The identified failure modes for sub-systems of PSA MOP are as follows (Jha & Gaur, 2022):

- (a) Compressor
- (b) Dryer
- (c) Oxygen concentrator tank, including top diffuser, bottom diffuser and chemical composition of oxygen concentrator
- (d) Piping and valve system, including angular seat valve, solenoid valve, non-returning valve and auto change over valve
- (e) Control panel and sensors (pressure and oxygen purity).

## 2.4 Acceptance Criteria

The acceptance criteria considered were set by the designer as per their requirements and the requirements of ISO (2016). During uninterrupted operation of the system for 48 h, the acceptance criteria are as follows:

- (a) Oxygen purity:  $90 \pm 3\%$
- (b) Oxygen flow rate: 960 LPM
- (c) No dust formation
- (d) Oxygen Pressure: 4.2 - 5.5 Bar
- (e) Dry air dew point:  $\leq -50\text{ }^{\circ}\text{C}$

## 3. RESULTS AND DISCUSSION

### 3.1 Failure Database

Based on MOP failure at the manufacturing stage, a failure database was prepared as per the required format. Failure analysis was conducted and the root causes were identified by the manufacturer. The corrective actions were implemented and their effectiveness was observed. Production tests were then conducted against the acceptance criteria before clearing the MOPs. The failure database is shown in Table 1.

**Table 1: Failure database for MOPs at the manufacturing stage.**

No.	Day of Failure	Skid No.	Failure Observed	Cause of Failure	Corrective Action Taken	Result
1	Day 1	Skid no. 38	Dust formation	Concentrator layers filling not as per standard	Concentrator chemical layers and Top diffuser design changed	Production test cleared - Day 46
2	Day 2	Skid no. 27	Low performance (oxygen purity)	Valve leakage	Valve replaced and Dryer design changed	Production test cleared - Day 44
3	Day 3	Skid no. 35	Low performance (oxygen purity)	Dryer problem	Dryer design changed	Production test cleared - Day 64
4	Day 7	Skid no. 47	Dust formation	Concentrator layers filling not as per standard	Concentrator chemical layers and Top diffuser design changed	Production test cleared - Day 44
5	Day 7	Skid no. 51	Low performance (oxygen purity)	Valve leakage and Dryer problem	Valve replaced and Dryer design changed	Production test cleared - Day 44
6	Day 7	Skid no. 54	Dust formation	Concentrator layers filling not as per standard	Concentrator chemical layers and Top diffuser design changed	Production test cleared - Day 63
7	Day 7	Skid no. 61	Low performance (oxygen purity)	Valve leakage	Valves replaced and concentrator chemical layers changed	Production test cleared - Day 44
8	Day 8	Skid no. 52	Dust formation	Concentrator layers filling not as per standard	Concentrator chemical layers and Top diffuser design changed	Production test cleared - Day 44
9	Day 9	Skid no. 02	Dust formation	Concentrator layers filling not as per standard	Concentrator chemical layers and Top diffuser design changed	Production test cleared - Day 79
10	Day 9	Skid no. 03	Dust formation	Concentrator layers filling not as per standard	Concentrator chemical layers and Top diffuser design changed	Production test cleared - Day 79
11	Day 9	Skid no. 53	Dust formation	Concentrator layers filling not as per standard	Concentrator chemical layers and Top diffuser design changed	Production test cleared - Day 88
12	Day 10	Skid no. 33	Low performance (oxygen purity)	Dryer problem	Dryer design changed	Production test cleared - Day 44
13	Day 11	Skid no. 32	Dust formation	Concentrator layers filling not as per standard	Concentrator chemical layers and Top diffuser design changed	Production test cleared - Day 44
14	Day 11	Skid no. 59	Dust formation	Concentrator layers filling not as per standard	Concentrator chemical layers and Top diffuser design changed	Production test cleared - Day 63
15	Day 11	Skid no. 49	Low performance (oxygen purity)	Dryer problem	Dryer design changed	Production test cleared - Day 62
16	Day 13	Skid no. 62	Low performance (oxygen purity)	Dryer problem	Dryer design changed	Production test cleared - Day 44
17	Day 18	Skid no. 97	Low performance (oxygen purity)	Valve leakage	Valve replaced and Dryer design changed	Production test cleared - Day 63
18	Day 24	Skid no. 34	Dust formation	Modified diffuser not welded properly	Top diffuser replaced and Dryer design changed	Production test cleared - Day 45

19	Day 24	Skid no. 64	Low performance (oxygen purity)	Dryer problem	Dryer design changed	Tested again on Day 68 but failed due to low performance
20	Day 24	Skid no. 102	Dust formation	Top diffuser ripped	Top diffuser design changed	Production test cleared - Day 44
21	Day 25	Skid no. 05	Low performance (oxygen purity)	Dryer problem	Dryer design changed	Tested again on Day 44 but failed due to low performance
22	Day 25	Skid no. 08	Low performance (oxygen purity)	Valve leakage	Valves tightened and Dryer design changed	Production test cleared - Day 89
23	Day 25	Skid no. 31	Low performance (oxygen purity)	Valve leakage and Dryer problem	Valves tightened and Dryer design changed	Tested again on Day 44 but failed due to low performance
24	Day 28	Skid no. 09	Low performance (oxygen purity)	Dryer problem	Dryer design changed	Production test cleared - Day 89
25	Day 28	Skid no. 82	Low performance (oxygen purity)	Dryer problem	Dryer design changed	Production test cleared - Day 44
26	Day 28	Skid no. 07	Low performance (oxygen purity)	Dryer problem	Dryer design changed	Production test cleared - Day 74
27	Day 40	Skid no. 87	Low performance (oxygen purity)	Dryer problem	Top diffuser replaced and Dryer design changed	Production test cleared - Day 81
28	Day 65	Skid no. 117	Low performance (oxygen purity)	Valve leakage and Oxygen sensor kit fault	Replaced the oxygen sensor kit and valves tightened	Production test cleared - Day 67

### 3.2 Common Failures, Root Causes and Corrective Actions

Based on the failure analysis, two common failures were identified, which were dust formation and low oxygen purity. For dust formation, the root causes identified were chemical composition of concentrator layers and top diffuser configuration. For low oxygen purity, the root causes identified were valve assembling defects, oxygen purity sensor defects and dryer problems. The common root causes and corrective actions are shown in Table 2.

**Table 2: Common root causes and corrective actions.**

No.	Failure Types	No. of Plants	Failure observed	Causes of Failure	Corrective Actions	Result
1	Dust	11	Dust formation	(a) Concentrator chemical composition layers did not settle properly due to less time taken for filling. (b) Top modified diffuser ripped.	(a) Concentrator chemical composition layers changed as per baseline. (b) Dryer design changed. (c) Top diffuser design changed.	11 MOPs cleared in retest.
2	Performance	17	Low performance (oxygen purity)	(a) Valves assembly defect. (b) Dryer problem. (c) Oxygen sensor kit problem.	(a) Valves tightened or replaced. (b) Dryer design changed. (c) Oxygen sensor kit changed.	(a) 14 MOPs cleared in retest. (b) 3 MOPs failed in retest.

### 3.3 Effectiveness of the Productivity-Oriented FRACAS Framework

Table 3 shows the effectiveness of corrective actions taken. For the first 120 plants cleared, the testing failure rate during production testing was 18.5%. Total number of tests conducted during this time were 120 cleared and 27 failed. After that, production was stopped for a brief period and a thorough failure analysis was carried out. The common root causes were identified and corrective actions were

suggested. After implementation of the corrective actions, the testing failure rate during production testing was reduced to just 0.5%.

**Table 3: Effectiveness of corrective actions.**

No.	Period	No. of Tests / Retests Undertaken	No. of Failures	Failure Rate (%)
1	Until Day 43	120 / 27	27	18.5
2	From Day 44 to Day 92	190 / 1	1	0.5
<b>Total</b>		338	28	8.3

From 28 re-tests, 25 MOPs were cleared after implementing corrective actions. From Equation 1, the effectiveness of the proposed FRACAS framework was evaluated as 89%.

$$E_f = \frac{c}{n} * 100 \quad (1)$$

where:

$E_f$  - Effectiveness of proposed FRACAS framework

$c$  - Number of failures corrected

$n$  - Total number of failures

The effectiveness of the proposed FRACAS framework augmented the production output, transformed the unsuccessful design into an efficacious design and protected the production firm from losses.

#### 4. CONCLUSION

A productivity-oriented FRACAS framework was proposed and failure data at the production site was studied, with inferences drawn about the common root causes. Through implementation suitable corrective actions, the testing failure rate during production was reduced from 18.5 to just 0.5%. The effectiveness of the proposed FRACAS framework was found to be 89%.

The research implication is that this study can help in designing and implementing productivity-oriented failure reporting systems and emphasising on the effectiveness of FRACAS during the production stage. Careful designing of failure reporting, analysis and corrective action process for a composite system can increase the productivity of the system and protect the production firm from losses. The novelty of the proposed FRACAS framework is that the corrective action is scrutinised during acceptance testing. After the system failed during the acceptance testing, the production process was stopped, the proposed FRACAS process followed, and effective corrective actions were implemented for the further lots. The proposed FRACAS framework is flexible and straightforward to implement for any type of production site.

The benefits of productivity-oriented FRACAS are that the failures encountered during acceptance testing are analysed and corrective actions are implemented without interfering in or delaying the manufacturing process. However, the primary limitation is that the involvement of the FRACAS team is only at the acceptance stage rather than involvement throughout the production process. This late involvement can increase the cost of implementing corrective actions. However, considering the urgency of the requirement of MOPs in hospitals during the COVID-19 pandemic, implementation of FRACAS at the acceptance stage avoided delays in production of MOPs.

The research limitation is that the data available for the study was for the acceptance testing stage and not for the failures during the design evaluation stage. However, this gives a good measure of the effectiveness of productivity-oriented FRACAS. The scope for future study includes the development of design-oriented FRACAS and implementation during the design evaluation phase.

## REFERENCES

- Braglia, M., Gabbrielli, R. & Marrazzini, L. (2021). Risk failure deployment: A novel integrated tool to prioritize corrective actions in failure mode and effects analysis. *Qual. Reliab. Eng. Int.*, **37**: 433-450.
- Chang, J., Yoo, S.J. & Kim, S. (2021). Development and application of computerized risk registry and management tool based on FMEA and FRACAS for total testing process. *Medicina*, **57**: 477.
- DOD (Department of Defense) (1995). *MIL-HDBK-2155: Failure Reporting Analysis and Corrective Action Taken*. US Department of Defense (DOD), Washington DC, US.
- ISO (International Organization for Standardization) (2016). *ISO 7396-1:2016: Medical Gas Pipeline Systems - Part 1: Pipeline Systems for Compressed Medical Gases and Vacuum*. International Organization for Standardization (ISO). Geneva, Switzerland.
- Jha, M. & Gaur, N. (2022). Life cycle of medical oxygen from production to consumption. *J. Family Med. Prim. Care*, **11**: 1231–1236.
- Sakhaei, B. (2023). Development of an operational procedure based on issues management methodologies in the FRACAS process. *Life Cycle Reliab. Saf. Eng.*, **12**: 323-340.
- Susanto, T., Djamaris, A., Ayumi, F. & Novianti, M. (2017). Evaluation of downtime in milling system with approach to failure reporting analysis and corrective action system. *Int. J. Eng. Technol.*, **17**: 17.
- Tanner, J. (2020). Agile FRACAS in production manufacturing. *2020 Annu. Reliab. Maintainab. Symp. (RAMS)*, Palm Springs, California, US.